

# Applied Research Laboratory

## Technical Report

CORROSION-FATIGUE OF A  
COMPOSITE LASER WELDMENT

by

Ellen M. Perkoski  
Richard Queeney  
Ram Kossowsky

AD-A209 973

PENNSSTATE



**SDTICD**  
ELECTE  
JUL 12 1989  
*CE* **H**

DISTRIBUTION STATEMENT A

Approved for public release  
Distribution Unlimited

4

The Pennsylvania State University  
APPLIED RESEARCH LABORATORY  
P. O. Box 30  
State College, PA 16804

**CORROSION-FATIGUE OF A  
COMPOSITE LASER WELDMENT**

by

Ellen M. Perkosi  
Richard Queeney  
Ram Kossowsky

Technical Report No. TR 89-003  
July 1989

**SDTICD**  
**ELECTE**  
**JUL 12 1989**  
**H**

Supported by:  
Space and Naval Warfare Systems Command

L. R. Hettche, Director  
Applied Research Laboratory

Approved for public release; distribution unlimited

89 7 11 255

UNCLASSIFIED

## SECURITY CLASSIFICATION OF THIS PAGE

## REPORT DOCUMENTATION PAGE

1a. REPORT SECURITY CLASSIFICATION Unclassified			1b. RESTRICTIVE MARKINGS	
2a. SECURITY CLASSIFICATION AUTHORITY			3. DISTRIBUTION/AVAILABILITY OF REPORT Approved for public release; distribution unlimited.	
2b. DECLASSIFICATION/DOWNGRADING SCHEDULE				
4. PERFORMING ORGANIZATION REPORT NUMBER(S) TR-89-003			5. MONITORING ORGANIZATION REPORT NUMBER(S)	
6a. NAME OF PERFORMING ORGANIZATION Applied Research Laboratory The Pennsylvania State University		6b. OFFICE SYMBOL (If applicable)	7a. NAME OF MONITORING ORGANIZATION	
6c. ADDRESS (City, State, and ZIP Code) P. O. Box 30 State College, PA 16804			7b. ADDRESS (City, State, and ZIP Code)	
8a. NAME OF FUNDING/SPONSORING ORGANIZATION Space and Naval Warfare Systems Command		8b. OFFICE SYMBOL (If applicable)	9. PROCUREMENT INSTRUMENT IDENTIFICATION NUMBER	
8c. ADDRESS (City, State, and ZIP Code) Department of the Navy Washington, DC 20363			10. SOURCE OF FUNDING NUMBERS PROGRAM ELEMENT NO.	TASK NO.
			PROJECT NO.	WORK UNIT ACCESSION NO.
11. TITLE (Include Security Classification) "Corrosion-Fatigue of a Composite Laser Weldment"				
12. PERSONAL AUTHOR(S) Ellen M. Perkoski, Richard Queeney, Ram Kossowsky				
13a. TYPE OF REPORT M. S. Thesis	13b. TIME COVERED FROM TO	14. DATE OF REPORT (Year, Month, Day)	15. PAGE COUNT 133	
16. SUPPLEMENTARY NOTATION				
17. COSATI CODES FIELD GROUP SUB-GROUP			18. SUBJECT TERMS (Continue on reverse if necessary and identify by block number) fatigue crack propagation, steel, notched specimens, air, weldment, salt water, growth rate, corrosion	
19. ABSTRACT (Continue on reverse if necessary and identify by block number) In this study, the fatigue crack propagation rates were studied within air and salt water environments for various regions of a laser weldment comprised of two steels: AISI 4140 and HTS. Notched compact-tension specimens were used to test the response of the weldment to cracking within the center of the weld fusion zone as well as the various heat-affected zones. Testing in either environment was done at one Hertz and at five Hertz to assess the contributions of salt water and frequency on fatigue crack growth within the weldment zones. The various candidates for the rate-controlling mechanism in corrosion-fatigue were compared with the results of the experiments; topographical features of the fracture surfaces were used also in conjunction with the results of the fatigue crack growth rate versus cyclic stress intensity data to determine the mechanisms of corrosion-fatigue.  (Continued on back)				
20. DISTRIBUTION/AVAILABILITY OF ABSTRACT <input checked="" type="checkbox"/> UNCLASSIFIED/UNLIMITED <input type="checkbox"/> SAME AS RPT. <input type="checkbox"/> DTIC USERS			21. ABSTRACT SECURITY CLASSIFICATION Unclassified	
22a. NAME OF RESPONSIBLE INDIVIDUAL			22b. TELEPHONE (Include Area Code) (814) 865-6344	22c. OFFICE SYMBOL

UNCLASSIFIED

SECURITY CLASSIFICATION OF THIS PAGE

19 ABSTRACT - Continued

The highest fatigue crack growth rates were found from tests in salt water for the portion of the heat-affected zone near the fusion zone and on the side of the HTS material; these data were not sufficiently higher than those from this region tested in air, and the region was therefore found to be not particularly susceptible to enhanced cracking during corrosion-fatigue. Accelerated crack growth rates of as much as six times those in air were found for two regions within the weldment; evidence of intergranular failure was cited as contributing to these increased crack growth rates in salt water. The shapes of the fatigue crack growth rate versus cyclic stress intensity curves indicated that the rate-controlling mechanisms changed throughout the lifetime of a corrosion-fatigue experiment; the various mechanisms that vie to control crack growth rates and the ways in which they interact have been modelled using the results of the fatigue crack growth rate versus cyclic stress intensity data.

Accession For	
NTIS GRA&I	<input checked="checked" type="checkbox"/>
DTIC TAB	<input type="checkbox"/>
Unannounced	<input type="checkbox"/>
Justification	
By	
Distribution/	
Availability Codes	
Dist	Avail and/or Special
A-1	



UNCLASSIFIED

SECURITY CLASSIFICATION OF THIS PAGE

## ABSTRACT

In this study, the fatigue crack propagation rates were studied within air and salt water environments for various regions of a laser weldment comprised of two steels: AISI 4140 and HTS. Notched compact-tension specimens were used to test the response of the weldment to cracking within the center of the weld fusion zone as well as the various heat-affected zones. Testing in either environment was done at one Hertz and at five Hertz to assess the contributions of salt water and frequency on fatigue crack growth within the weldment zones. The various candidates for the rate-controlling mechanism in corrosion-fatigue were compared with the results of the experiments; topographical features of the fracture surfaces were used also in conjunction with the results of the fatigue crack growth rate versus cyclic stress intensity data to determine the mechanisms of corrosion-fatigue.

The highest fatigue crack growth rates were found from tests in salt water for the portion of the heat-affected zone near the fusion zone and on the side of the HTS material; these data were not sufficiently higher than those from this region tested in air, and the region was therefore found to be not particularly susceptible to enhanced cracking during corrosion-fatigue. Accelerated crack growth rates of as much as six times those in air were found for two regions within the weldment; evidence of intergranular failure was cited as contributing to these increased crack growth rates in salt water. The shapes of the fatigue crack growth rate versus cyclic stress intensity curves indicated that the rate-controlling mechanisms changed throughout the lifetime of a corrosion-fatigue experiment; the various mechanisms that vie to control crack growth rates and the ways in which they interact have been modelled using the results of the fatigue crack growth rate versus cyclic stress intensity data.

## TABLE OF CONTENTS

	<u>Page</u>
LIST OF TABLES .....	vi
LIST OF FIGURES .....	vii
ACKNOWLEDGEMENTS .....	x
 CHAPTER	
1. INTRODUCTION .....	1
1.1 Statement of the Problem .....	1
2. GENERAL RESPONSE OF METALS TO CORROSION-FATIGUE .....	2
2.1 Mechanisms, Microstructures and Electrochemistry .....	2
2.2 The Concept of a Rate-Controlling Process .....	5
2.3 Frequency, Load Ratio and Stress Intensity Effects .....	9
2.4 The Response of Weldments to Corrosion-Fatigue .....	10
3. TEST SPECIMENS .....	12
3.1 Welding Procedure .....	12
3.2 Weldment Microstructures .....	13
3.2.1 Surface Microstructures .....	16
3.2.2 Cross-Section Microstructures .....	23
3.3 Weldment Evaluation .....	29
3.3.1 Optical Inspection .....	32
3.3.2 Hardness Tests .....	32
3.3.3 Fracture Surface Porosity .....	36
3.4 Compact-Tension (CT) Specimen Fabrication .....	38
4. EXPERIMENTAL PROCEDURES .....	42
4.1 Introduction .....	42
4.2 Fatigue Tests .....	42
4.2.1 Apparatus .....	42
4.2.2 Data Collection .....	43
4.2.3 Test Procedure .....	44
4.3 Treatment of Data .....	46
4.3.1 Crack Length Versus Number of Cycles Data .....	47
4.3.2 Computing $D_a/D_N$ Versus $\Delta K_{eff}$ Data .....	48
4.3.3 The Crack Growth Rate Law .....	50
4.3.4 Fracture Toughness Calculations .....	51
4.4 Treatment of Fractured Specimens .....	51
4.5 Porosity Determination .....	53
5. RESULTS .....	54
5.1 Fatigue Data .....	54
5.2 Results of Fracture Toughness Calculations .....	61
5.3 Porosity Levels .....	62
5.4 Fatigue Surfaces .....	63

## TABLE OF CONTENTS (Continued)

	<u>Page</u>
6. DISCUSSION AND CONCLUSIONS .....	69
6.1 Corrosion-Fatigue Data .....	69
6.1.1 Low $\Delta K_{eff}$ Behavior .....	69
6.1.2 Transition Stage Crack Growth Behavior .....	71
6.1.3 High $\Delta K_{eff}$ Behavior .....	72
6.1.4 Relative Cracking Rates of the Weldment Regions .....	73
6.1.5 Modelling the Rate-Controlling Mechanisms .....	74
6.2 Fracture Toughness Results .....	75
6.3 Fatigue Surfaces Analysis .....	78
6.3.1 The HTS HAZ N .....	79
6.3.2 The HTS HAZ F .....	80
6.3.3 The Weld Center .....	80
6.3.4 The 4140 HAZ .....	81
6.4 Conclusions .....	81
REFERENCES .....	83
APPENDIX A: COMPLETE CRACK LENGTH VERSUS NUMBER OF CYCLES DATA .....	86
APPENDIX B: COMPLETE DA/DN VERSUS $\Delta K_{eff}$ DATA .....	92
APPENDIX C: ALL SPECIMEN DIMENSIONS, LOAD RANGES AND LOAD RATIOS .....	100
APPENDIX D: ALL DA/DN VS. $\Delta K_{eff}$ PLOTS WITH STRAIGHT LINE FITS...	100
APPENDIX E: COMPLETE FINAL CRACK LENGTHS AND MAXIMUM LOAD DATA .....	122

## LIST OF TABLES

<u>Table</u>	<u>Page</u>
3.1 Nominal Material Compositions .....	15
3.2 CT-Specimen Numbers and the Regions Tested.....	37
5.1 Constants C and m from Equation 4.5 .....	59
5.2 Values of $\Delta K_{eff}$ at Transition Onset ( $\Delta K_{eff T}$ ) and End ( $\Delta K_{eff III}$ ) .....	60
5.3 Estimated Strengths For Weldment Regions .....	60
5.4 Fracture Toughness Values and Final Plastic Zone Sizes.....	61
5.5 Fracture Surface Porosity in the Fatigue and Fast Fracture Regions .....	62



## LIST OF FIGURES

<u>Figure</u>	<u>Page</u>
2.1 Schematic Diagram Illustrating the Mechanisms of Hydrogen Embrittlement and Metal Dissolution Involved in Corrosion-Fatigue. ....	6
3.1 Sketch of Welding Operation Showing Progression of Third Laser Pass. ....	12
3.2 (A) Top Surface of Weldment and (B) Schematic of Top Surface Showing Locations of Figures 3.5 to 3.11. ....	14
3.3 Section of Top Surface of Weldment Showing Regions from HTS (Left) to HTS Heat-Affected Zone (Near) (Right). ....	17
3.4 Section of Top Surface of Weldment Showing Regions from Weld Center (Left) to 4140 (Right). ....	17
3.5 Nominal HTS Surface Microstructure. ....	19
3.6 HTS Heat-Affected Zone (Far) Surface Microstructure. ....	20
3.7 HTS Heat-Affected Zone (Near) Surface Microstructure. ....	20
3.8 Surface Microstructure of Weld Center. ....	21
3.9 Surface Microstructures of Weld Center and 4140 Heat-Affected Zone. ....	21
3.10 4140 Heat-Affected Zone Surface Microstructure. ....	22
3.11 Surface Microstructure of 4140. ....	22
3.12 (A) Cross-Section of Weldment and (B) Sketch of Weldment Cross-Section Showing Locations of Figures 3.13 to 3.21. ....	23
3.13 Cross-Section Microstructure of HTS. ....	26
3.14 Cross-Section Microstructure of HTS Heat-Affected Zone (Near). ....	26
3.15 Cross-Section Microstructure of HTS Heat-Affected Zone (Near). ....	27
3.16 Cross-Section Microstructures of HTS Heat-Affected Zone (Near) and Weld Center. ....	27
3.17 Weld Center Microstructure Near Top Surface Viewed from Cross-Section. ....	28
3.18 Weld Center Microstructure 25 mm from Top Surface of Weldment Viewed from Cross-Section. ....	28
3.19 Micrograph Showing Weld-Center Microstructure (Left) and 4140 Heat Affected Zone Microstructure (Right). ....	30
3.20 Cross-Section Microstructure of 4140 Heat-Affected Zone. ....	31

## LIST OF FIGURES (Continued)

<u>Figure</u>	<u>Page</u>
3.21 4140 Microstructure Viewed from Cross-Section. ....	31
3.22 Macrograph of Cross-Section Used in Rockwell "C" Hardness Tests.....	34
3.23 Rockwell "C" Hardness Versus Position for Various Depths within Cross-Section. ....	34
3.24 Rockwell "C" Hardness Versus Position for Specimens at Depths of 20-28 mm. ....	35
3.25 Rockwell "C" Hardness Versus Position for Specimens at Depths of 12-20 mm. ....	35
3.26 Rockwell "C" Hardness Versus Position for Specimens at Depths of 3-8 mm. ....	36
3.27 Fracture Surface of Specimen #23 Showing Fatigue and Fast Fracture Regions.....	37
3.28 Original Weldment Sections Which Yielded (A) Three CT-Specimens and (B) Four CT-Specimens. ....	39
3.29 Steps in CT-Specimen Fabrication. (A) Sectioning Original Plate, (B) Milling Cross-Section to Uniform Thickness and (C) Locating Specimen Notch Center with respect to Weld. ....	40
3.30 Dimensions of CT-Specimen.....	41
4.1 Sketch of Entire Apparatus for Fatigue Tests. ....	45
4.2 Sketch of Circuit Used in Crack Propagation Data Acquisition.....	46
4.3 Example Sketch of Curve Fit Used to Determine Crack Growth Rates.....	49
4.4 Fractured Specimen Showing Crack Path and Gross Plastic Deformation. ....	52
5.1 All Runs in the HTS HAZ F. ....	55
5.2 All Runs in the HTS HAZ N.....	55
5.3 All Runs in the Weld Center.....	56
5.4 All Runs in the 4140 HAZ.....	56
5.5 All Runs in Salt Water at 1 Hz. ....	57
5.6 All Runs in Air at 1 Hz.....	57
5.7 All Runs in Salt Water at 5 Hz. ....	58

## LIST OF FIGURES (Continued)

<u>Figure</u>	<u>Page</u>
5.8 All Runs in Air at 5 Hz.....	58
5.9 Fatigue Surface of the HTS HAZ N in Air at Low Cyclic Stress Intensity.....	64
5.10 Fatigue Surface of the HTS HAZ N in Salt Water at Low Cyclic Stress Intensity.....	64
5.11 Fatigue Surface of the HTS HAZ N in Air at Intermediate Cyclic Stress Intensity.....	65
5.12 Fatigue Surface of the HTS HAZ N in Salt Water at Intermediate Cyclic Stress Intensity.....	65
5.13 Fatigue Surface of the HTS HAZ F in Air.....	66
5.14 Fatigue Surface of the HTS HAZ F in Salt Water.....	66
5.15 Fatigue Surface of the Weld Center in Air.....	67
5.16 Fatigue Surface of the Weld Center in Salt Water.....	67
5.17 Fatigue Surface of the 4140 HAZ in Air at Low Magnification.....	68
5.18 Fatigue Surface of the 4140 HAZ in Salt Water at Low Magnification.....	68
6.1 A Proposed Model for the Rate-Controlling Mechanisms During Corrosion-Fatigue.....	76

## ACKNOWLEDGEMENTS

The author would like to express her sincere gratitude to her thesis co-advisor, Dr. Richard A. Queeney, for his keen interest in the planning, preparation and completion of this thesis. She also extends thanks to her thesis co-advisors, Drs. Queeney and Ram Kossowsky, for their patient cooperation with all aspects of this project, and to Mr. Paul Denney for his assistance in providing the preliminary information needed in this study.

The funding for this project was provided under Space and Naval Warfare Systems Command Prime Contract N00024-85-C-6041.

## **Chapter 1**

### **INTRODUCTION**

The application of laser technology to the welding of steels has invited investigation into the consequences resulting from this unique processing operation. From the mechanics community comes a wave of interest into the changes of material responses of weldments as a result of laser processing [1-7]. Early interests of laser weldment manufacturers focused on the optimization of those parameters that influence weldment soundness; such variables as welding power and welding speed were examined in terms of their effects on hardness, impact resistance, porosity and tensile properties [1,8]. Curiosity over the microstructural characteristics and solidification behavior of laser beam weldments [3,6,9-11], and the resulting effects on stress-corrosion cracking [4,7] and hot and cold cracking [2] has excited the metallurgical community. The culmination of interests on the part of each of these groups has resulted in the present study into the corrosion-fatigue resistance of a composite laser weldment.

#### **1.1 Statement of the Problem**

The purpose of the investigation was to determine the effect of corrosion-fatigue on crack propagation rates within the various zones of a weldment region, to assess the roles of variables such as weldment porosity, microstructure and frequency on the corrosion-fatigue crack growth behavior of these regions, to address the various rate-controlling mechanisms during corrosion-fatigue and to use the results of the crack growth rate data to compare the relative air and salt water crack growth behaviors of the regions within the composite weldment.

## Chapter 2

### GENERAL RESPONSE OF METALS TO CORROSION-FATIGUE

The broad category of environmentally assisted cracking (EAC) includes stress-corrosion cracking (SCC) for static loads, and corrosion-fatigue when repetitive loading is applied. Fontana has offered the following definition of corrosion-fatigue: corrosion fatigue is the reduction of fatigue resistance due to the presence of a corrosive medium [12]. Implicit to this definition is an amount of synergism owing to the effects of cyclically varying stresses and corrosive attack. Indeed, it has been suggested that features associated with corrosion, such as pitting, which occur to large extent during corrosion-fatigue, are less pronounced or even absent during static tests in the same environment [13-16]. The universally accepted manifestation of a corrosion-fatigue failure in a corrosive environment is an increased crack growth rate when referenced to growth rates under inert environmental conditions.

#### 2.1 Mechanisms, Microstructures and Electrochemistry

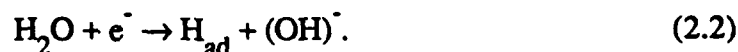
The mechanisms of hydrogen embrittlement and metal dissolution have both been proposed to account for enhanced fatigue crack growth rates observed for metals in aqueous solutions. That both processes actually contribute simultaneously to the deleterious effects of the metal/electrolyte system in fatigue has not been confirmed within the literature; most researchers tend to cite one predominant mechanism in a given situation [14,17-24]. Dissolution mechanisms have been found in some studies [14,17,19], especially when the steel is reportedly insensitive to hydrogen embrittlement [18]. Others have observed increased crack growth rates corresponding to increased accessibility to hydrogen [22] or when evidence of increased hydrogen activity exists [24]. Those that accept both mechanisms as operative and conclude that one is merely favored over the other during corrosion-fatigue often report conflicting reasons for the promotion of one

mechanism over the other [13,19]. Scott cites hydrogen embrittlement as the mechanism of corrosion-fatigue unless another chemical or diffusion process can enforce a slower rate [13], while tests by Cowling and Appleton have revealed that enhanced crack growth is caused by dissolution unless another factor is present that promotes hydrogen embrittlement to occur [19].

To the casual observer it seems plausible that the conditions exist in a metal/aqueous environment system for both embrittlement by diffused hydrogen and anodic dissolution of the metal. Hydrogen production is achieved by the hydronium ion reduction reaction:



where  $\text{H}_{\text{ad}}$  is adsorbed hydrogen on the metal surface, or by water reduction according to:



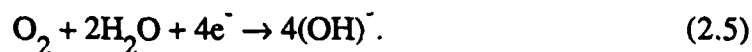
The adsorbed hydrogen concentration at the crack tip is then absorbed:



allowing embrittlement to occur. Anodic dissolution of iron requires two reactions. The metal is oxidized in the anodic reaction:



and the cathodic reaction by which both oxygen and the electrons are removed from the solution is:



Scott has pointed out that the hydrogen evolution reaction of Equation 2.2 may occur instead of Equation 2.5 in de-aerated solutions [13]. The oxidation and reduction reactions must occur at the same rate regardless of whether reduction occurs by Equation 2.2 or 2.5.

Closer inspection of the electrochemical conditions at the tip of the occluded crack suggests that the bulk solution electrochemistry does not necessarily represent the conditions at the crack tip and that the reactions listed above may be inhibited in the region of interest. Attempts to describe the thermodynamic conditions at the tip of the crack have focused on monitoring the pH and potential [13,16,25,26] in order to establish what Ford has called the "corrosion potential" [27], as well as to describe the diffusion of species down the crack as a means of determining which corrosion mechanism is favored [24,28]. In one experiment for which a wide range of applied currents greatly varied the pH at the crack tip, it was reported that the potential/pH combination as measured at the crack tip was consistently conducive to hydrogen evolution in salt water solutions [13]. In a similar study in seawater, Hodgkiess and Cannon also reported that an applied potential influenced the crack tip pH and that hydrolysis did occur, but that those results were not strong evidence for the hydrogen embrittlement reaction [26]. In separate studies by Turnbull [24] and Torronen and Kemppainen [28] it has been determined that the crack tip is completely devoid of oxygen and that hydrolysis is favored.

Various processes are available for the embrittlement of steel to occur due to hydrogen interaction. The proposed mechanisms have been discussed by Hertzberg [29] and applied to different types of steels by Nelson [30] and are presented as follows. Body-centered cubic or tetragonal steels, namely ferrite and martensite, allow rapid movement of



hydrogen and solubility of hydrogen is low. High strength martensitic steels are very susceptible to becoming embrittled by the diffusion of hydrogen down a stress gradient to a region of high tensile triaxiality where it interacts with the metal lattice to lower cohesive strength. The ferritic steels usually show resistance to stress-corrosion cracking, but, during fatigue, hydrogen in the metal lattice enhances dislocation mobility; the resulting multiple slip systems within a grain cause plastic incompatibility with neighboring grains, and brittle behavior results. Hydrogen embrittlement can also occur by internal pressurization at voids due to hydrogen supersaturation, or by reduction of the surface energy of the metal at an internally free surface. As Nelson has pointed out, these mechanisms of hydrogen embrittlement are parallel; the one which occurs fastest in a particular metal/electrolyte system will prevail.

Although support for either a metal dissolution or hydrogen embrittlement mechanism exists in the literature there is also evidence that these mechanisms do not act to the exclusion of one another [13,29]. Consider that in the absence of oxygen, the cathodic reaction which must accompany anodic dissolution is in fact the hydrolysis reaction that is necessary for the hydrogen embrittlement mechanism. It can be expected that for a given metal/electrolyte system, a knowledge of the crack tip environment can be combined to propose a mechanism for the corrosion-fatigue response of the system, if a rate-controlling process can be established for the given conditions at the crack tip which also predicts the same enhanced growth rate mechanism.

## 2.2 The Concept of a Rate-Controlling Process

The extent to which enhanced cracking will occur in a particular system depends upon the rates at which various processes proceed for the specific conditions of crack tip pH and potential. Furthermore, these crack tip phenomena depend strongly on the kinematic properties of the reactive species and electrolyte responsible for the transport of ions to the crack tip. The metal surface reactions of either oxidation and reduction for the

case of dissolution, or the adsorption of hydrogen in embrittlement, depend upon mobilities of electrons and hydrogen, respectively, within the metal. Difficulty in determining a rate-controlling process arises from the observance that conditions at the crack tip may not be predicted by steady-state diffusion and thermodynamics, but rather that the mixing action owing to sinusoidal variation of the sides of the crack serves to enhance the transport of species to the crack [28].

Figure 2.1 schematically illustrates the processes present during the conditions of corrosion-fatigue; the mechanisms of metal dissolution and hydrogen embrittlement are shown to be occurring at different locations for clarity. The role of the electrolyte in a dissolution model can easily be assessed for the case of static corrosion: if the process is stimulated by stirring the electrolyte or otherwise enhancing diffusion, then the corrosion rate is limited by the concentration of ionic species in solution.

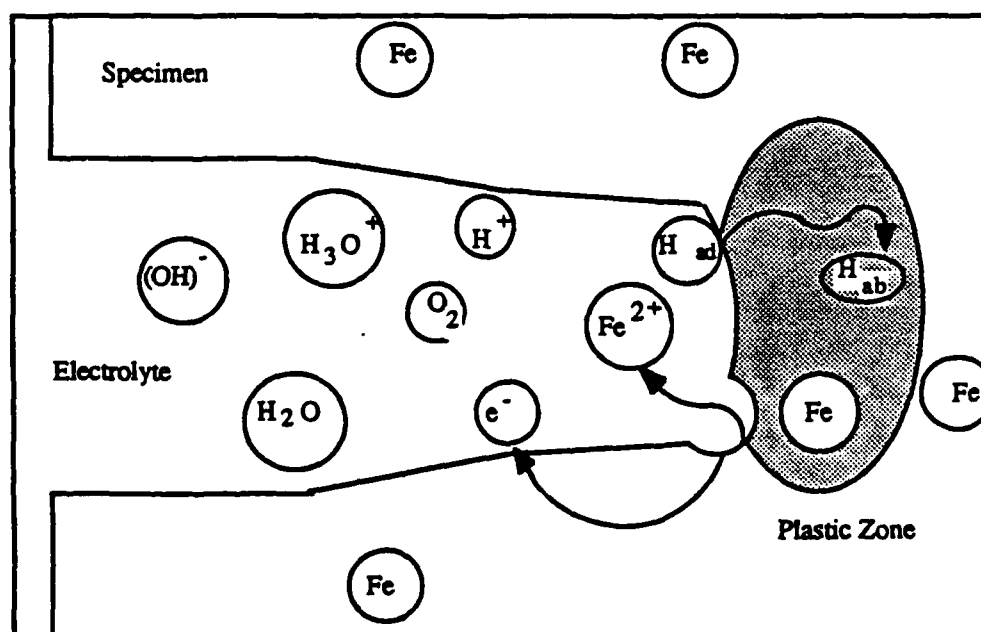


Figure 2.1: Schematic Diagram Illustrating the Mechanisms of Hydrogen Embrittlement and Metal Dissolution Involved in Corrosion-Fatigue.

The dissolution mechanism is otherwise said to be controlled by the slowest process involved in the oxidation-reduction reactions at the crack tip which may be the production of electrons during oxidation, the consumption of electrons during reduction, the transport of the electrons themselves or replenishment of the ionic species at the metal/electrolyte surface. The propensity with which hydrogen embrittles is dependent upon hydrogen transport to the metal/electrolyte interface, the dissolution, adsorption and absorption of hydrogen at the crack tip, diffusion of hydrogen to the embrittlement site and the subsequent embrittlement mechanism itself. When it is acknowledged that hydrogen embrittlement and metal dissolution may both proceed in a corrosive environment, then the evolution of hydrogen during the reduction reaction in dissolution may be considered as a source for hydrogen adsorption in embrittlement. The role of the electrolyte under static loading is not necessarily replaced during fatigue by the mixing effects of cyclic strains at the crack tip because the diffusion of species to the mouth of the crack, where mixing effects begin to become important, may still limit the corrosion process during corrosion-fatigue.

Corrosion products form films on the surface of the metal and have been found to inhibit hydrogen entry [25]. The rates at which these films form or break, owing to fatigue, may also be considered as the rate-controlling process [20].

Once all of the events have been accounted for, determination of a rate-controlling process requires discrimination between parallel and sequential events. Parallel mechanisms occur simultaneously, albeit at different rates, and without dependence on one another. The rate-controlling process among such events is the one that occurs fastest. In parallel mechanisms, all of the processes compete to achieve the same result and only one is thought to be successful, but the rate at which this mechanism occurs is limited by the fact that the other events also occur. Sequential mechanisms occur in succession; each mechanism in the sequence is essential to the overall process, and the slowest event in the sequence limits the rate at which the sequence can be completed. The obvious analogy is to

electrical resistors in parallel or in series, and determination of the actual rates of parallel or sequential events would be by the same summation procedures used for resistors. The resistance,  $R_i$ , of a system to a cracking mechanism that produces a crack growth rate,  $(da/dN)_i$ , would be given by the inverse of that crack growth rate. Then the overall crack resistance owing to all mechanisms,  $R_{eff}$ , which is equal to the inverse of the observed crack growth rate, may be written as a function of the individual resistances for sequential mechanisms and parallel mechanisms as in Equation 2.6 and 2.7, respectively:

$$R_{eff} = \sum_i R_i = \sum_i \frac{1}{\left(\frac{da}{dN}\right)_i} \quad (2.6)$$

$$\frac{1}{R_{eff}} = \sum_i \frac{1}{R_i} = \sum_i \left(\frac{da}{dN}\right)_i \quad (2.7)$$

The overall process of corrosion-fatigue may involve both parallel and sequential mechanisms. For instance, the rate at which the embrittlement process proceeds once hydrogen is absorbed into the metal can be modelled as:

$$\frac{1}{R_E} = \left(\frac{da}{dN}\right)_E = \sum_i H_i \quad (2.8)$$

where  $H_i$  represents the crack growth rate due to the  $i^{th}$  parallel embrittlement mechanism,  $(da/dN)_E$  is the overall crack growth rate owing to the embrittlement mechanism itself and  $R_E$  is the resistance of the material to crack growth due to the embrittlement mechanisms. The crack growth rate determined from Equation 2.8 would be one of the terms in an overall sequential or parallel process equation such as Equation 2.6 or 2.7.

### 2.3 Frequency, Load Ratio and Stress Intensity Effects

In addition to the mixing effects that arise owing to the action of mechanical fatigue, the cyclic frequency, load ratio and stress intensity parameters interact with the electrolyte in other ways to influence the corrosion-fatigue process. Many researchers have found that the effect of cyclic loading in an aggressive environment is reduced at high frequencies [13,21,23,24] and that the frequency must generally be below 1.0 Hertz in order to have an appreciable effect on crack growth. The effect of environment on fatigue crack growth rates has also been shown to decrease below frequencies of 0.01 Hertz owing to the growth and subsequent cracking of films [13]. If the effect of frequency is solely to limit the amount of time available for a diffusion or embrittlement process to occur [20,31], then it would not be very difficult to find the rate-controlling frequency for a given metal/electrolyte system. However, an additional effect of cyclic stress frequency is the strain rate at the crack tip; evidence exists that increased crack growth rates result from increased strain rates [14,24,27]. These consequences of cyclic frequency combine with the role of mixing in the enhancement of transport mechanisms within the electrolyte to account for the dependence of corrosion-fatigue on frequency.

One result of the application of cyclic loading that is not prevalent during static loading is the contribution of pitting to crack retardation by blunting of the crack tip. Pitting has been reported at frequencies of 0.5 Hertz, 20 Hertz [14], 30 Hertz [23] and below 0.01 Hertz [13]. However, the presence of pits is not always indicative of retardation; at very long lives and at high stresses pits serve as crack initiation sites.

The function of the load ratio,  $R$ , in enhancing crack growth rates is to dictate the percentage of time the crack is opened to its environment [13,21,28]. In a non-aggressive environment the effect of  $R$ , as manifested in crack growth rates versus cyclic stress intensity data, can be eliminated by representing crack growth as a function of the effective cyclic stress intensity factor,  $\Delta K_{eff}$ . Since  $\Delta K_{eff}$  represents the cyclic stress range over which the crack is opened, crack closure may be monitored during testing by

compliance measurements [21] or may be accounted for by an empirical relationship such as the one proposed by Schijve [32]:

$$\Delta K_{\text{eff}} = \Delta K (0.55 + 0.35R + 0.1R^2). \quad (2.9)$$

Corrosion products on the fracture surface of a specimen contribute to closure in an aggressive environment and are not accounted for by Equation 2.9; however, the effective stress intensity values found through compliance measurements would still be valid.

The cyclic stress intensity factor,  $\Delta K$ , controls the size of the plastic zone in fatigue, and the plastic zone size, in turn, controls the extent to which hydrogen can embrittle a material [13]. The size of the plastic zone can only limit the rate of enhancement due to hydrogen embrittlement when no other process enforces a slower rate. Researchers have found a plateau in  $da/dN$  versus  $\Delta K$  curves for corrosive environments which represents a region of crack growth that is independent of the cyclic stress intensity factor [22,33]. The onset of the plateau has been linked to growth of the plastic zone to the size of the prior austenite grains [22] and also to the transition from that of crack initiation via slip to that of Mode I fatigue crack growth, at which point the availability of hydrogen controls cracking [33]. At high  $\Delta K$  levels the mechanism of enhanced growth is believed to be ductile rupture and is once again dependent upon  $\Delta K$  [22,33].

#### 2.4 The Response of Weldments to Corrosion-Fatigue

As a result of the welding operation, materials may develop a sensitization zone which renders the weldment susceptible to intergranular corrosion. Sensitization occurs during welding because of the precipitation of chromium carbides at the grain boundaries and subsequent chromium depletion near the regions of the carbides [12]. Heat-treatment is often the chosen recourse for combating the sensitization zone in weldments; however

heat-treatment is usually not feasible for the large structures suited to laser welding. It has been shown that the laser welding operation does not allow sufficient time for sensitization to develop and there is little danger that this cracking mechanism is operative in the corrosion-fatigue of laser weldments [7].

Other consequences indigenous to the welding operation have been linked to changes in the response of the base metal to corrosion-fatigue. Davis has reported that residual stresses, defects and porosity enhance crack retardation mechanisms in weldments [34]. Weldment porosity has been shown to have both retardation and enhancement effects on fatigue crack growth in air and in seawater; the cracking mechanism was found to be dependent upon the amount of porosity and the stress level in both environments [23].

## Chapter 3

### TEST SPECIMENS

#### 3.1 Welding Procedure

The weldment studied was manufactured at the Laser Processing Facility, Westinghouse Electric Research and Development Center, Pittsburgh, Pennsylvania. An actual trough cover and track made of HTS and ASTM 4140 steels, respectively, were butt-welded using a continuous CO<sub>2</sub> laser beam. The trough cover and track materials were heated to 2040° C prior to welding. The filler wire used was type 100S-1, 1.12 mm diameter wire and was also heated prior to welding. The welding operation consisted of six passes over a modified double "J" groove joint geometry; these six laser passes, at a laser power of 9 kw, a travel speed of 38.1 cm per minute and a filler wire feed rate of 457.2 cm per minute, produced a 3.18 cm thick weldment. The welding operation is sketched in Figure 3.1.

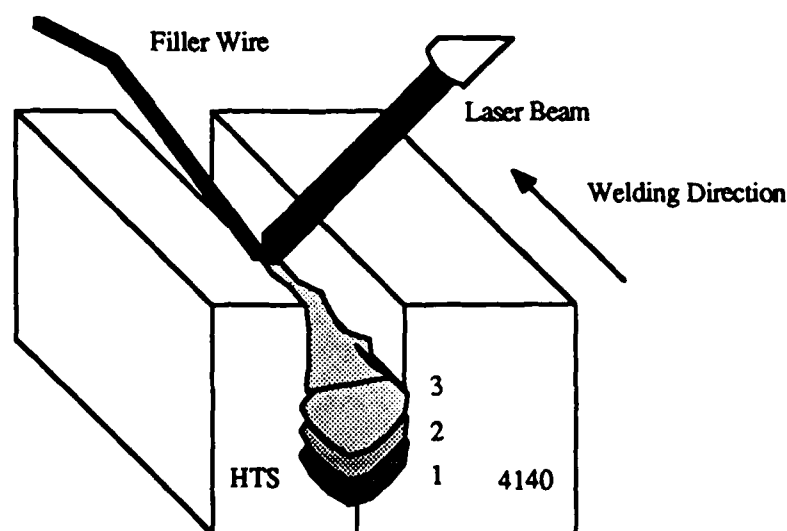


Figure 3.1: Sketch of Welding Operation Showing Progression of Third Laser Pass.



### **3.2 Weldment Microstructures**

A portion of the top surface of the welded material was sectioned, polished and etched for 30 seconds with 4% Nital solution to reveal the weldment microstructures contained throughout the entire region of the final laser pass. The microstructures were found to change quite continuously across the top surface of the weld. Etching revealed banded regions of variable degrees of shadings and provided a means to characterize and separate portions of the weldment for further study. Figure 3.2 contains a macrograph of the etched weld at 3X in (A) as well as a sketch of this same macrograph in (B). These regions are labelled in Figure 3.2 (B) and are defined as follows:

**HTS: Base metal.** The composition of HTS is given in Table 3.1.

**HTS HAZ F: HTS Heat-affected zone (far).** This region has been affected by the heat of the welding operation as its microstructure differs from that of the base metal. The HTS heat-affected zone was found to consist of two different regions and was therefore divided into a "far" region and a "near" region with reference to the proximity to the center of the fusion zone.

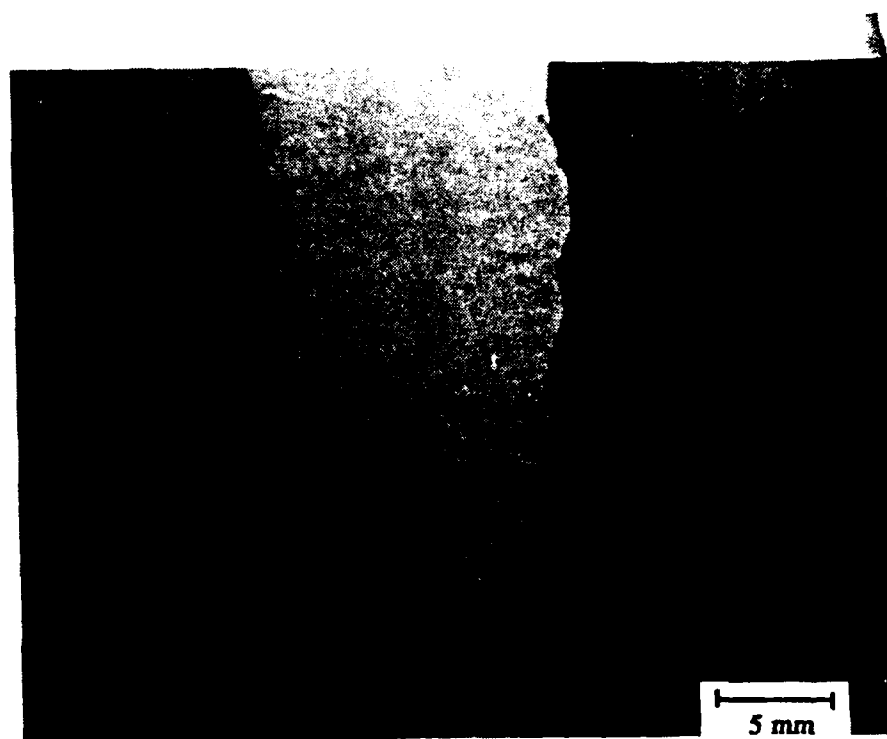
**HTS HAZ N: HTS Heat-affected zone (near).** This region lies between the center of the fusion zone and the HTS HAZ F, its microstructure was found to be different from those of its neighbors.

**Weld center:** The material within the center of the fusion zone is primarily the filler metal although some mixing with the base metals occurs [1]; the composition of the filler metal is given in Table 3.1.

**4140 HAZ: 4140 Heat-affected zone.** The microstructure within this region differs from that of the base metal as it has been altered by the heat of the welding operation.

**4140: Base metal.** The composition of 4140 is given in Table 3.1.

(A)



(B)

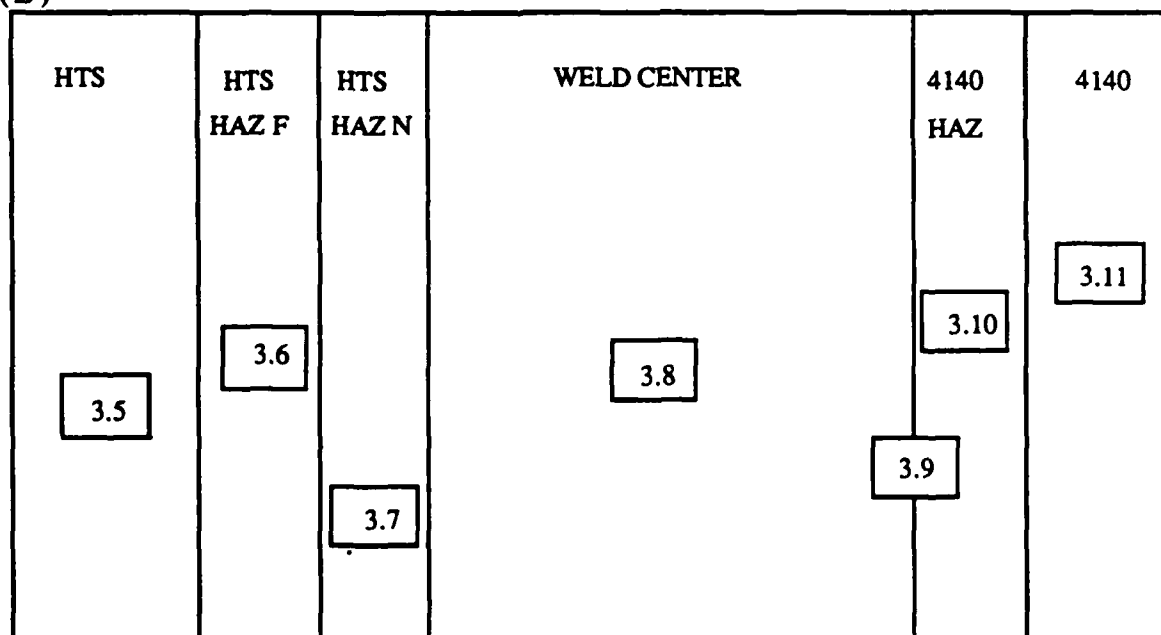


Figure 3.2: (A) Top Surface of Weldment and (B) Schematic of Top Surface Showing Locations of Figures 3.5 to 3.11.

Table 3.1 Nominal Material Compositions

element	<u>4140</u>	<u>HTS</u>	<u>filler</u>
C	0.4	0.18 max	0.06
Mn	0.75- 1.00	0.90- 1.60	1.33
P	0.025 max	0.04 max	****
S	0.025 max	0.04 max	****
Si	0.20- 0.35	0.10- 0.50	0.48
Cr	1.0	0.25 max	0.06
Mo	0.2	0.08 max	0.45
Cu	0.35 max	0.35 max	
Ni	0.25 max	0.40 max	1.59
Ti			0.011
Cb		0.05 max	
V		0.10 max	
Remainder Fe			

Photomicrographs taken at various regions along the top surface of the weldment, which span the entire range of microstructures found within the weldment from nominal HTS to nominal 4140, are shown in Figures 3.3 to 3.11. The continuous microstructural variation across the weldment surface has been captured at low magnification in Figures 3.3 and 3.4. The locations of the microstructures shown in Figures 3.5 to 3.11 have been designated in Figure 3.2 (B). The nominal compositions of 4140, HTS and the filler wire which make up the weldment are given in Table 3.1 [35,36].

A section of weldment was cross-sectioned, polished and etched to provide an additional view of the microstructures revealed in the surface photomicrographs and to determine what changes in microstructure occur with changes in depth. Photomicrographs of the various weldment regions, as observed from the cross-sectional angle, were taken near the top surface of the weldment. Many of the microstructures in Figures 3.13 to 3.21 should resemble those seen from the surface views as they were located within the first laser pass; all but Figure 3.18 were within 12 mm of the top surface of the weldment. The cross-sectional view from which these microstructures were photographed appears in Figure 3.12 (A), while the sketch of this region in Figure 3.12 (B) locates each of the photomicrographs on the cross-section.

### 3.2.1 Surface Microstructures

Two sections on the top surface of the weldment were photographed at 35X and appear in Figures 3.3 and 3.4. In Figure 3.3 the transition from the HTS, through the HTS HAZ F and into the HTS HAZ N is seen from left to right. HTS contains a network of large ferrite grains that border an austenitic matrix [37]; the procession of ferrite breakup as the more heat-affected direction was approached can be seen clearly in Figure 3.3. The effect of heat from the welding operation was transformation of the austenite matrix (far from the weld center) and even the entire structure (near the weld center) into martensite. The extent to which transformation occurred depended upon proximity to both the weld



Figure 3.3: Section of Top Surface of Weldment Showing Regions from HTS (Left) to HTS Heat-Affected Zone (Near) (Right).

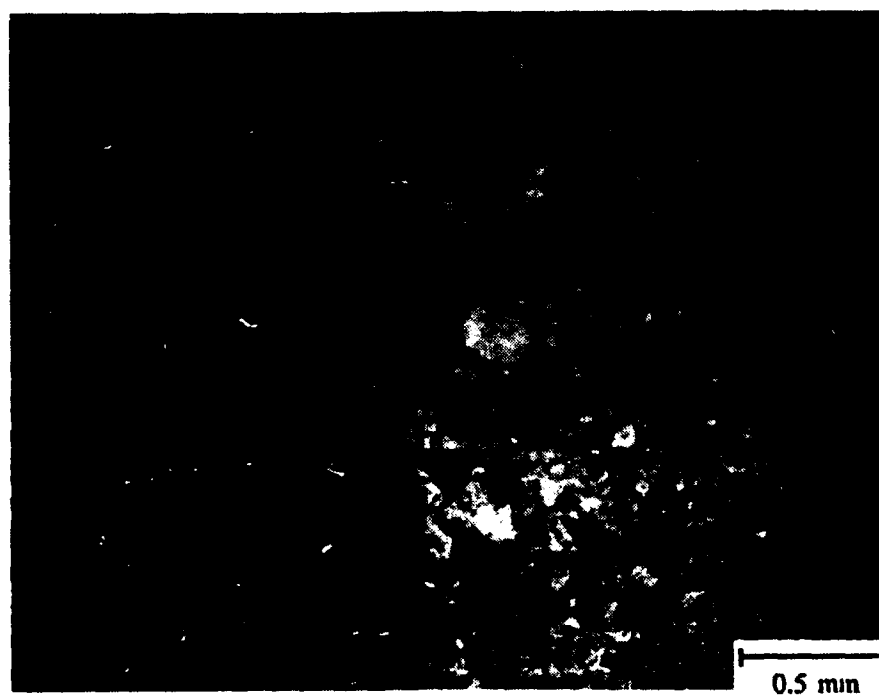


Figure 3.4: Section of Top Surface of Weldment Showing Regions from Weld Center (Left) to 4140 (Right).

center and subsequent laser passes. The three regions seen in Figure 3.3 have been labelled HTS, HTS HAZ F and HTS HAZ N. In Figure 3.4 the microstructural transition from the weld center through the 4140 HAZ and into the 4140 base metal is seen. The 4140 HAZ appears in the center of Figure 3.4 and is characterized by what appears to be cracking parallel to the welding direction.

Figures 3.5 to 3.11 contain photomicrographs taken at higher magnifications throughout the regions shown in Figures 3.3 and 3.4. The nominal HTS microstructure is seen at 500X in Figure 3.5. The large white grains are the boundary ferrite which form the network in Figure 3.3; they surround the matrix phase which is austenite [37]. Grey inclusions, as in the top right corner of Figure 3.5, are probably manganese sulfide (MnS) as they formed during solidification at the prior austenite grain boundaries. Figure 3.6 shows the HTS HAZ F microstructure at 500X. Small inclusions are clearly seen within the ferrite network grains in resemblance to the base metal, but the austenite that had comprised the matrix phase in the base metal has been transformed to very fine grains of martensite. In the HTS HAZ N the microstructure is entirely martensite and is clearly visible at 500X in Figure 3.7. It appears as though none of the boundary ferrite remains in this section of the weldment; none of the prior ferrite grain boundaries are outlined in the martensite structure. A large number of inclusions was found to occupy this region; the inclusions have been colored grey as a result of the etchant and are probably sulfides.

The weld center microstructure is seen at 500X in Figure 3.8. The structure is very fine, untempered martensite with small amounts of austenite. This microstructure is more readily observed as martensite in Figure 3.9 taken from the weld center/4140 HAZ boundary at 500X. The left side of Figure 3.9 is in the weld center region, the 4140 HAZ region begins near the center of Figure 3.9 and contains a dark phase which was described as cracking in the discussion of Figure 3.4. At this higher magnification this phase is seen to occur along the martensitic grain boundaries and resembles troostite [37], an extremely fine aggregate of cementite and ferrite.

The 4140 HAZ microstructure shown in Figure 3.10 outside of the region containing the troostite phase consists solely of martensite. There is not a dramatic transition to the nominal 4140 microstructure from the 4140 HAZ microstructure as was the case on the HTS side of the weldment. Instead, the large martensitic grains within the heat-affected zone seen in Figure 3.10 simply begin to decrease in size and number as the 4140 base metal is approached. Individual ferritic and pearlitic phases replace the martensitic grains immediately before the 4140 is reached. Figure 3.11 shows the nominal 4140 composition at 500X which consists of blocky ferrite and pearlite.



Figure 3.5: Nominal HTS Surface Microstructure.

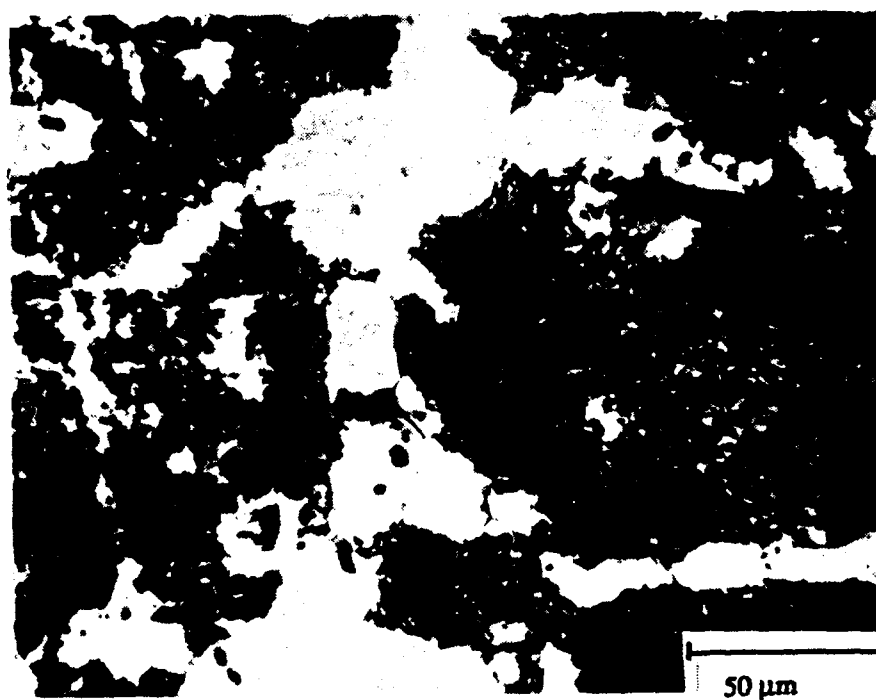


Figure 3.6: HTS Heat-Affected Zone (Far) Surface Microstructure.

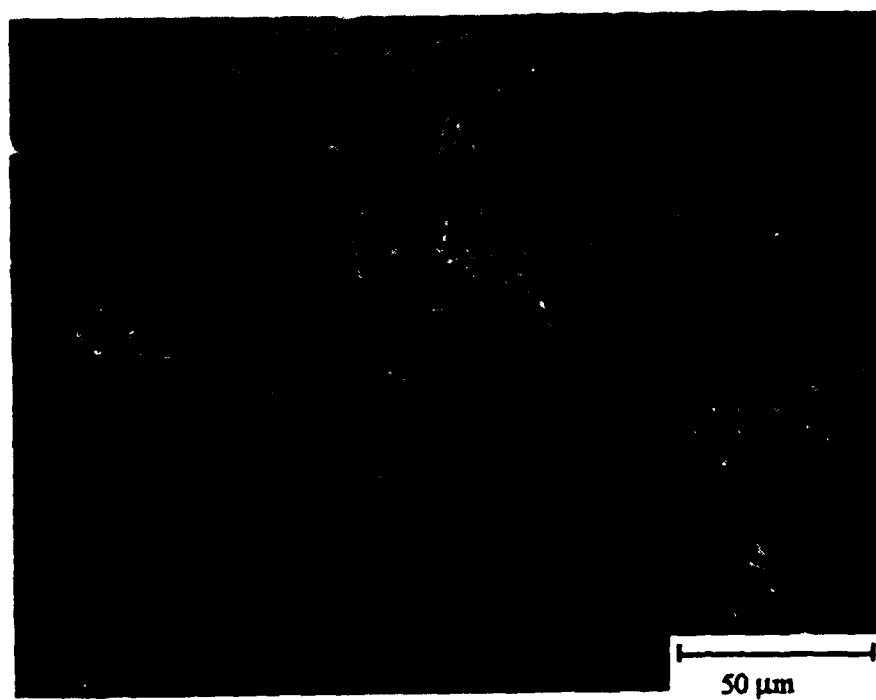


Figure 3.7: HTS Heat-Affected Zone (Near) Surface Microstructure.



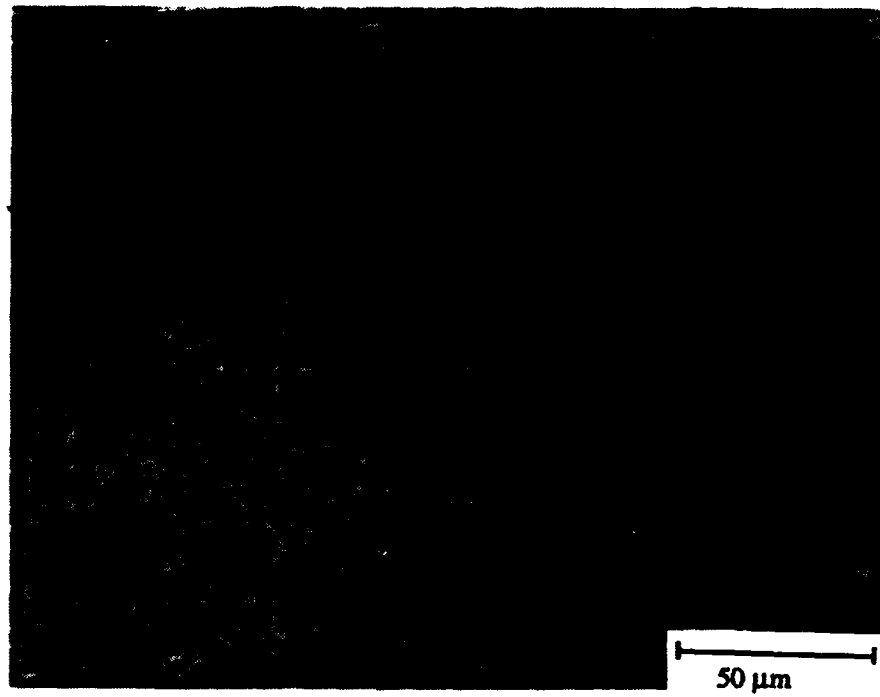


Figure 3.8: Surface Microstructure of Weld Center.

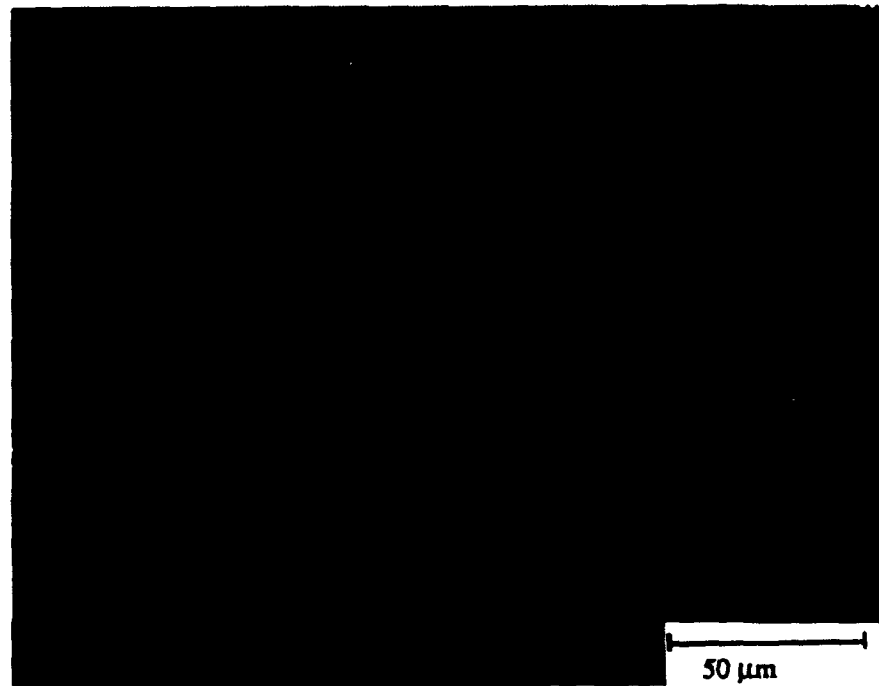


Figure 3.9: Surface Microstructures of Weld Center and 4140 Heat-Affected Zone.



Figure 3.10: 4140 Heat-Affected Zone Surface Microstructure.

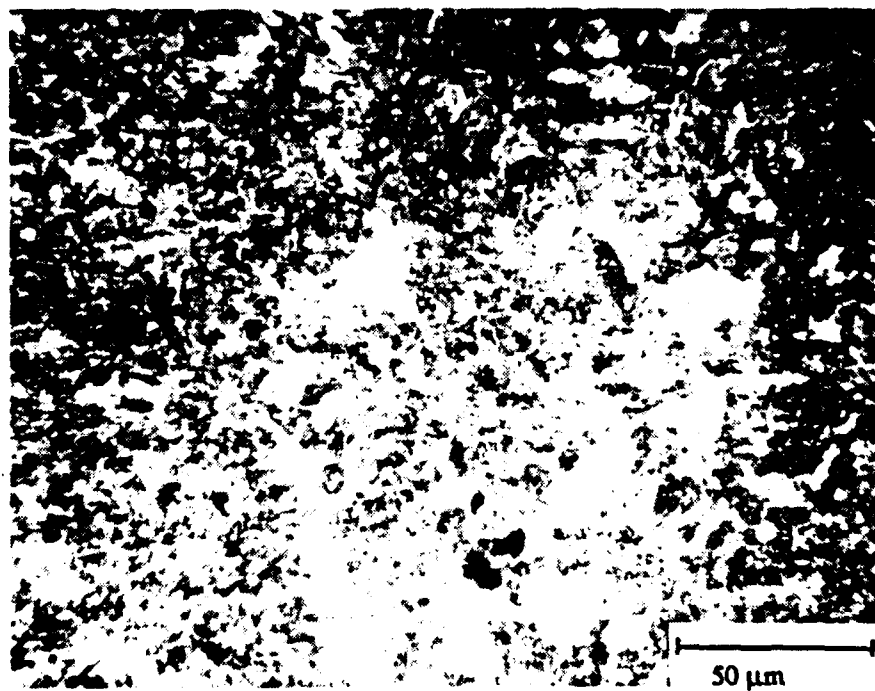


Figure 3.11: Surface Microstructure of 4140.

### 3.2.2 Cross-Section Microstructures

The weldment microstructures were studied throughout the cross-section shown at 3X in Figure 3.12 (A) and sketched in Figure 3.12 (B). Viewing the microstructures from this angle made it possible to determine whether a given laser pass influenced the microstructure of the previous pass. A three-dimensional understanding of the weldment structure can be gained from the combined top surface and cross-sectional views. Although the entire cross-section had been studied, only microstructures near the surface were photographed for comparison with those of the top surface view. The only significant difference in microstructure that was not discovered in the near surface photomicrographs was that of the weld center in Figure 3.18. This microstructure, found at a depth of 25 mm from the weldment surface, was therefore also included.

(A)

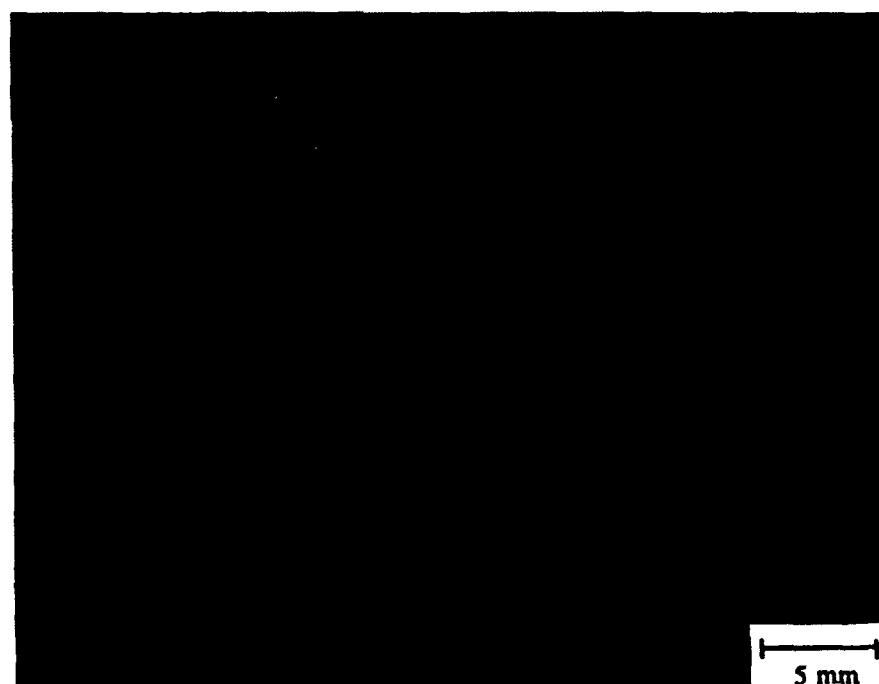


Figure 3.12: (A) Cross-Section of Weldment and (B) Sketch of Weldment Cross-Section Showing Locations of Figures 3.13 to 3.21.

(B)

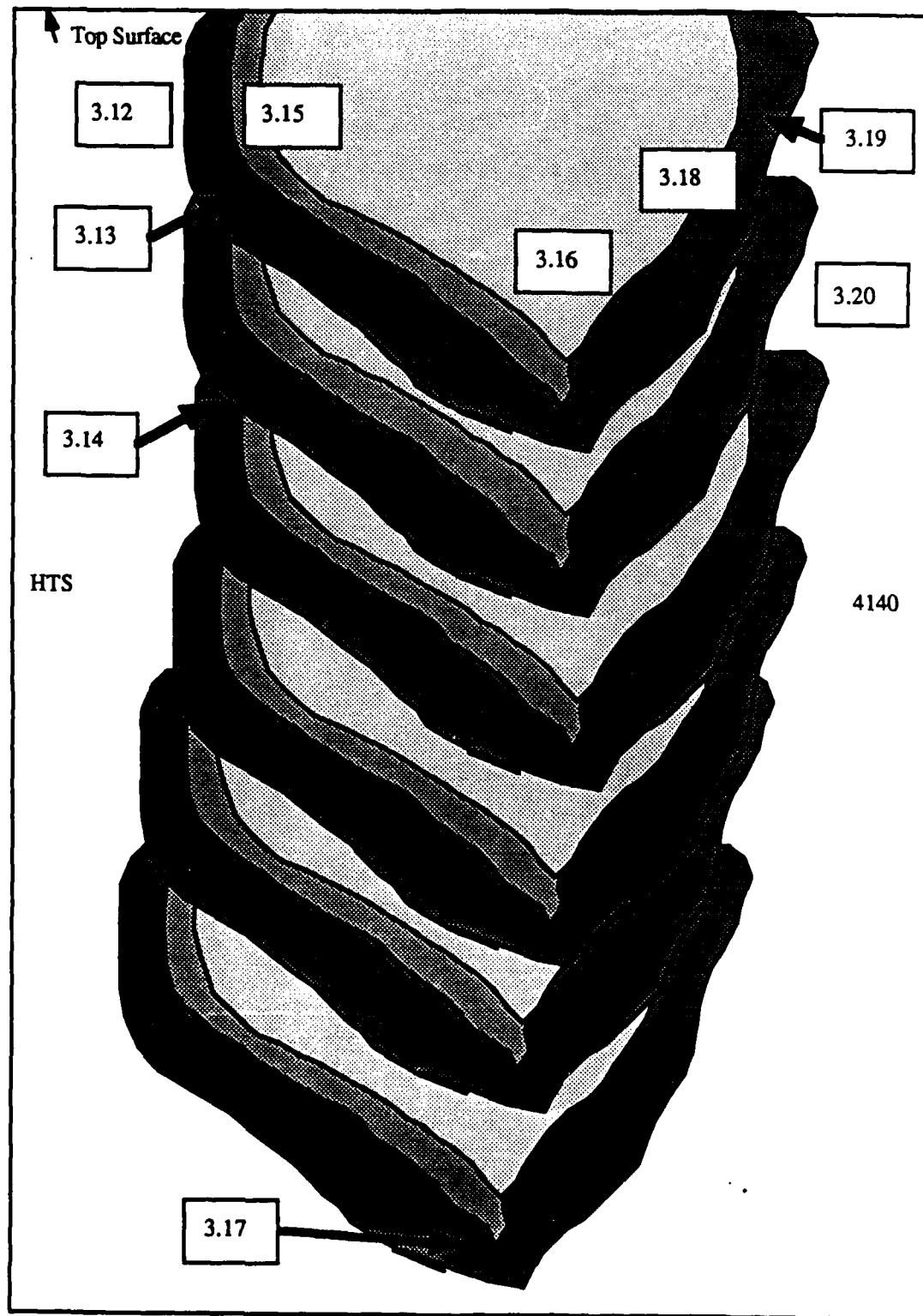


Figure 3.12 (Continued)

Figure 3.13 shows the ferrite network surrounding austenite in the HTS at 500X, and large grey MnS inclusions are clearly seen within the ferrite network. Figures 3.14 and 3.15 were taken from within the HTS HAZ N of the weldment cross-section at 500X and 1000X, respectively. Figure 3.14 does not show the sulfide phase that had been clearly apparent in the surface view of Figure 3.7. At 1000X, and under partially filtered light of Figure 3.15, the martensite grains in the HTS HAZ N are seen to be obviously bordered by a large number of these sulfides. Although they seem dark in this figure due to the lighting, the boundary phase had etched a dove-grey color.

The HTS HAZ N/weld center boundary microstructures are shown at 250X in Figure 3.16. Although shown at half the magnification of Figure 3.14, the grains in Figure 3.16 appear comparable in size to those in Figure 3.14 which are located at some distance from the weld center, possibly indicating a faster martensitic transformation rate nearer the weld center.

The weld center was photographed at 1000X in Figure 3.17, taken at 12 mm from the top surface, and in Figures 3.18, taken at a depth of 25 mm. The difference in these two microstructures arises from additional heat input to the region in Figure 3.18 by a subsequent laser pass. Figure 3.17 is within the final laser pass and therefore did not receive any further heat input.

Figure 3.19 of the weld center/4140 HAZ boundary shows very large martensite grains in the 4140 HAZ which decrease in number and size as the distance from the weld center increases. Eventually, the microstructure of the 4140 HAZ appears as in Figure 3.20 immediately before the 4140 structure becomes evident. Again, as in the heat-affected zone on the other side of the weld, the size differences of the martensite grains may be due to the relative speeds at which the transformation occurred. Heat would be expected to be conducted away extremely rapidly near the weld center, thereby causing a rapid solidification of the structure in this region. In Figure 3.21, the ferrite phase within the



Figure 3.13: Cross-Section Microstructure of HTS.

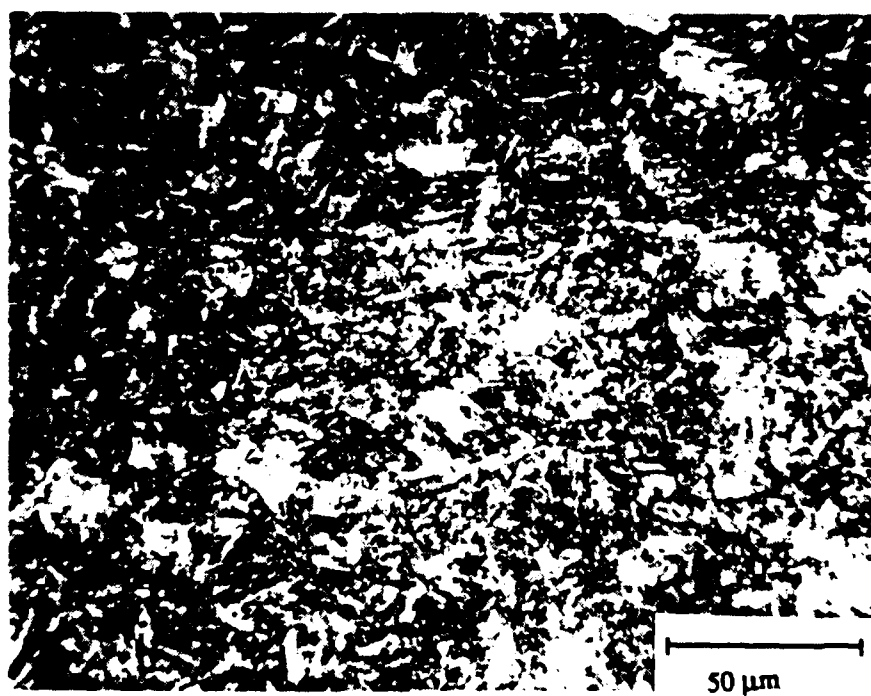


Figure 3.14: Cross-Section Microstructure of HTS Heat-Affected Zone (Near).

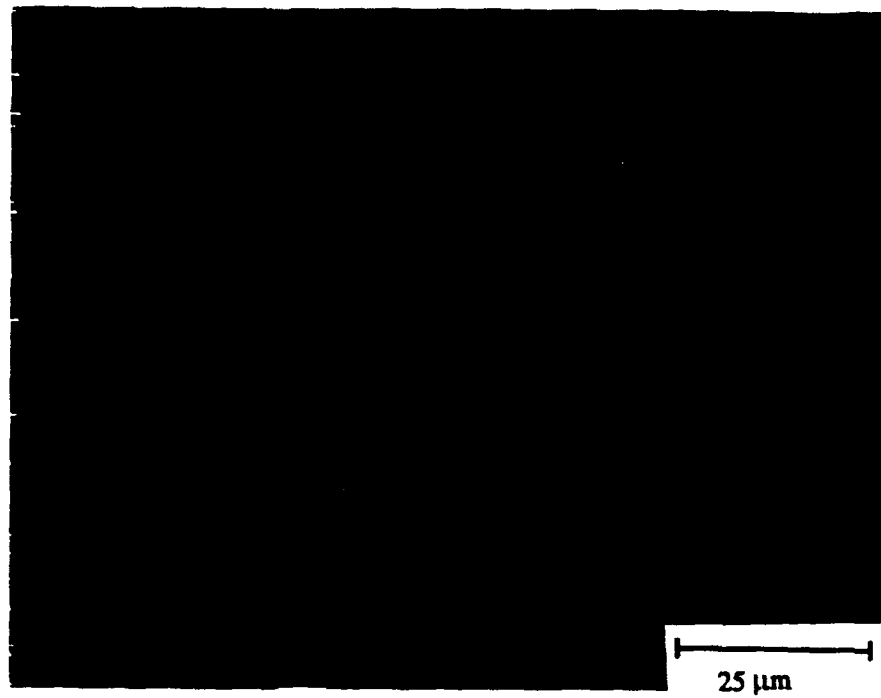


Figure 3.15: Cross-Section Microstructure of HTS Heat-Affected Zone (Near).

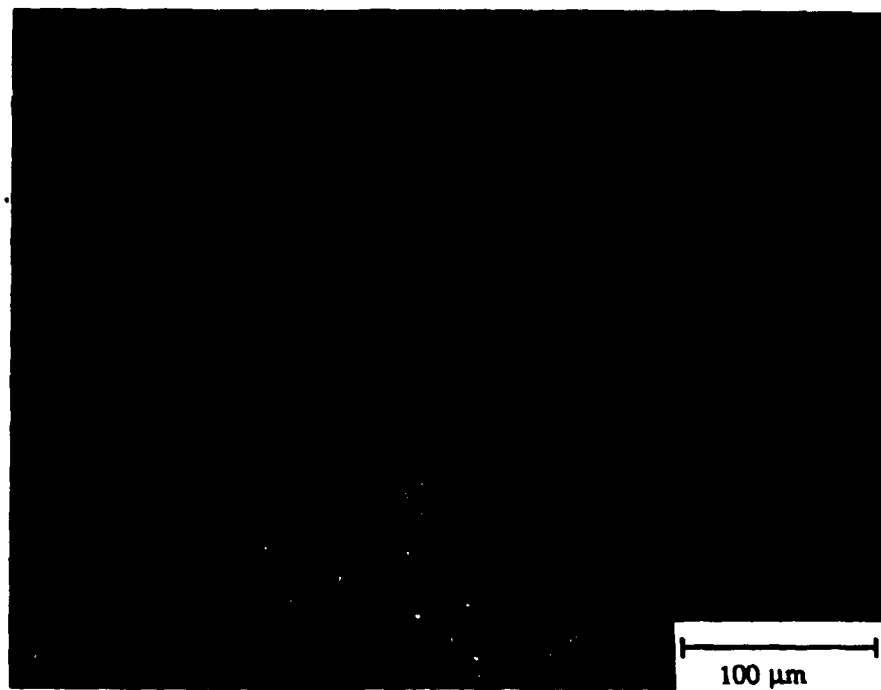


Figure 3.16: Cross-Section Microstructures of HTS Heat-Affected Zone (Near) and Weld Center.

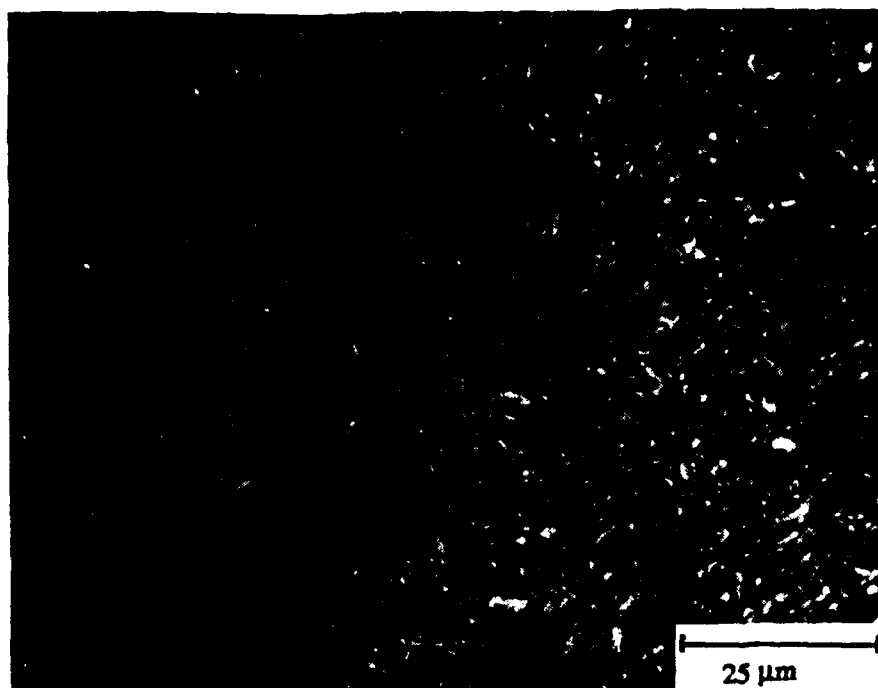


Figure 3.17: Weld Center Microstructure Near Top Surface Viewed from Cross-Section.

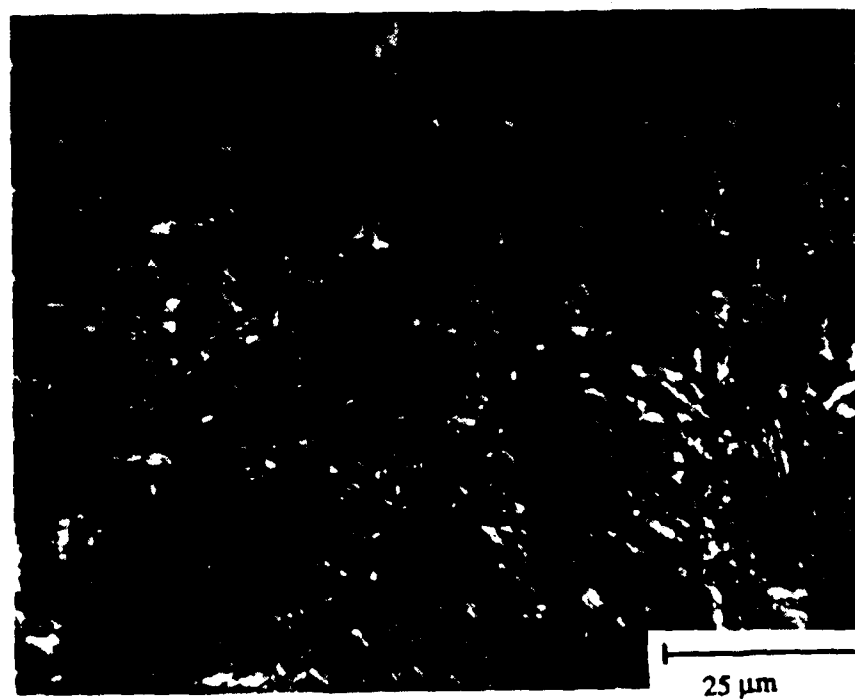


Figure 3.18: Weld Center Microstructure 25 mm from Top Surface of Weldment Viewed from Cross-Section.



4140 microstructure can be seen, but the individual cementite and ferrite layers within the very fine-grained pearlite phase are not discernable at this magnification.

No substantial changes in the various microstructures throughout the weldment occurred with depth, although some regions were affected by subsequent laser passes which served to slightly alter those microstructures. The microstructures change continuously but not abruptly across the various weldment zones. An exception to this continual change is directly within the weld center region where the microstructure remains constant over a 5 mm length.

### 3.3 Weldment Evaluation

It was determined by Denney and Nurminen that two of the three types of common weld defects, cracks from hot tearing and weld voids, could be eliminated if welding were conducted according to the optimal parameters they describe [1]. The third type of defect, porosity, could not be completely eliminated under these conditions; its occurrence in laser weldments is not fully understood. The amount of porosity found in weldments that were formed according to the optimal parameters of Denney and Nurminen was characterized using radiography and ultrasound (UT) inspection techniques. They detected no pores larger than 1.59 mm in diameter and determined that this degree of porosity would not significantly affect the mechanical response of the weldment [1].

The particular weldment studied here was fabricated using the parameter levels recommended by Denney and Nurminen except that the travel speed of 38.1 cm per minute at which this weldment was fabricated was higher than the recommended optimal value of 30.5 cm per minute. The resulting weldment was still expected to be characterized by the observations cited above in that cracks from hot tearing and weld voids were eliminated. A cross-section of the weldment was polished and etched for examination under an optical microscope at low magnification to determine whether acceptable porosity levels existed.

Hardness tests were conducted throughout the entire weldment cross-section to further characterize the weldment.

Another weldment evaluation study was conducted on the fractured surfaces of specimens upon completion of the fatigue experiments. Porosity levels on the fracture planes were determined using standard point counting methods, and this characterization was used to assess the role of porosity in the cracking process.

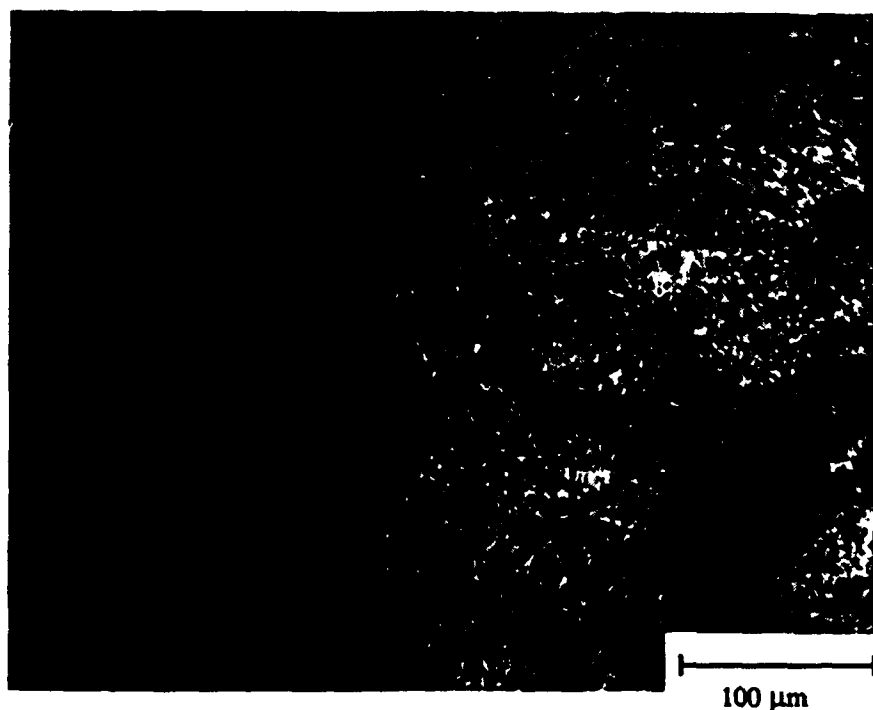


Figure 3.19: Micrograph Showing Weld-Center Microstructure (Left) and 4140 Heat-Affected Zone Microstructure (Right).

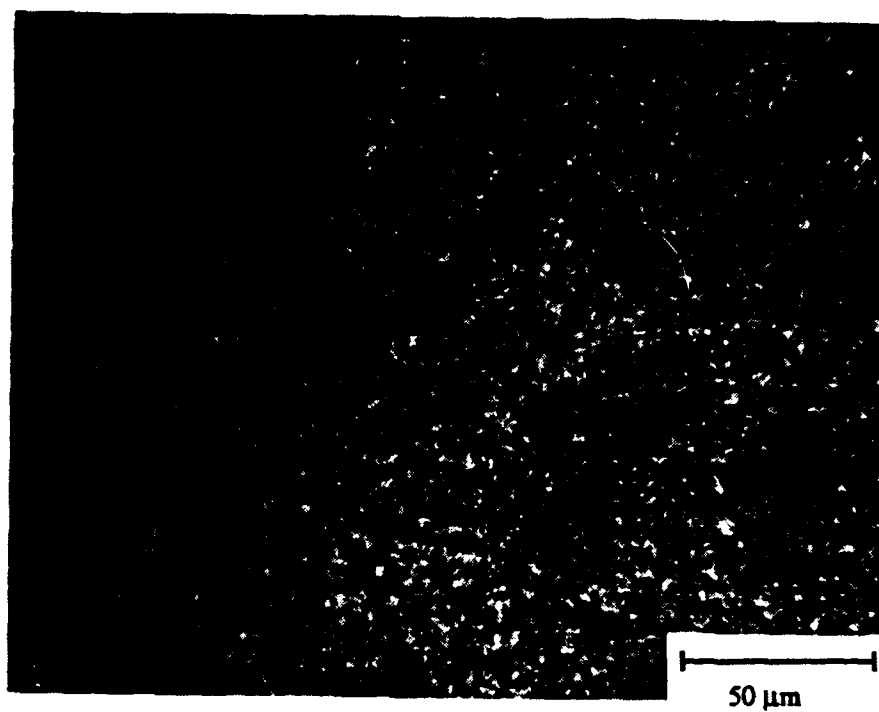


Figure 3.20: Cross-Section Microstructure of 4140 Heat-Affected Zone.

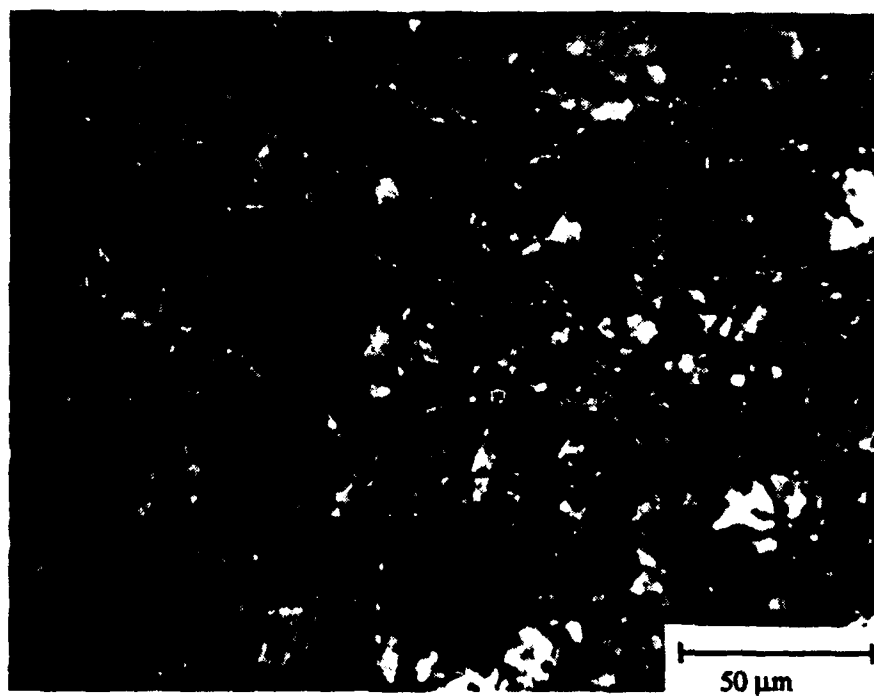


Figure 3.21: 4140 Microstructure Viewed from Cross-Section.

### 3.3.1 Optical Inspection

The section of weldment inspected under an optical microscope at 20X magnification is shown in Figure 3.12 A. Two defects were found on this surface, both of which were visible to the unaided eye. An inclusion measuring 0.12 mm by 0.22 mm was discovered 6.5 mm from the top of the weldment at the border between the final two weld passes and their 4140 heat-affected zones. The second defect found was a pore located 25 mm from the top of the weldment and situated entirely within the weld center of the first weld pass. This pore was larger than the inclusion, measuring 0.57 mm by 0.74 mm. Denney and Nurminen reported that laser weldments containing pores which were 1.59 mm in diameter or smaller could be considered as good quality welds; weldments which had not cracked as a result of the welding operation were found to contain pores of such sizes [1].

### 3.3.2 Hardness Tests

A second polished and etched weldment cross-section was used for Rockwell "C" hardness (HRC) evaluations; the tests were performed on the various weld zones and at different depths throughout the weld thickness. The macrograph of the cross-section showing the locations of all the hardness indentations appears in Figure 3.22. Results of the hardness profiles X-X', Y-Y', Z-Z' and W-W' of Figure 3.22 have been plotted in Figure 3.23 to show the variation of hardness throughout the different weld zones. Hardness variations with depth due to the subtle changes in microstructures caused by the heat of subsequent welding operations would probably not be conclusively detected using HRC tests because of the size of the indenter; the test was used as a means to determine weld quality as it compares to the weldment of Denney and Nurminen. Some changes with depth are noted from the data in Figure 3.23 which may be due in part to the irregular shape of the weldment itself. It can be seen in Figure 3.22 that two hardness indentations that

were intended to represent the same weldment zone would sometimes fall within different zones because of the non-uniform cross-section.

Results of the HRC data were compared to the work of Denney and Nurminen [1]. Figures 3.24 to 3.26 compare HRC values taken from approximately the same locations within two weldments that differed only in the welding speeds used to fabricate each. The data in Figure 3.24 were taken from tests conducted between 20 mm and 28 mm from the top surface of the weldment. Figures 3.25 and 3.26 were taken between depths of 12 mm to 20 mm and 3 mm to 8 mm, respectively. A notable difference in hardness was recorded for the various depths at the position designated as 7 mm, which appears to coincide with the HTS HAZ N/weld center boundary. The differences here may arise solely by having taken the readings on such a boundary. Readings taken at the next two positions, designated 9 mm and 11 mm, also reveal a change in hardness with depth. At both of these positions hardness increased with depth as is evident in Figure 3.23. These results would seem to indicate that subsequent laser passes may enhance the formation of martensite in this region. The microstructures shown in Figures 3.17 and 3.18 may also help to explain the results of the hardness tests. Some austenite was noted in Figure 3.17 taken near the top of the weldment, while the microstructure at 25 mm from the surface in Figure 3.18 was noted as purely martensitic.

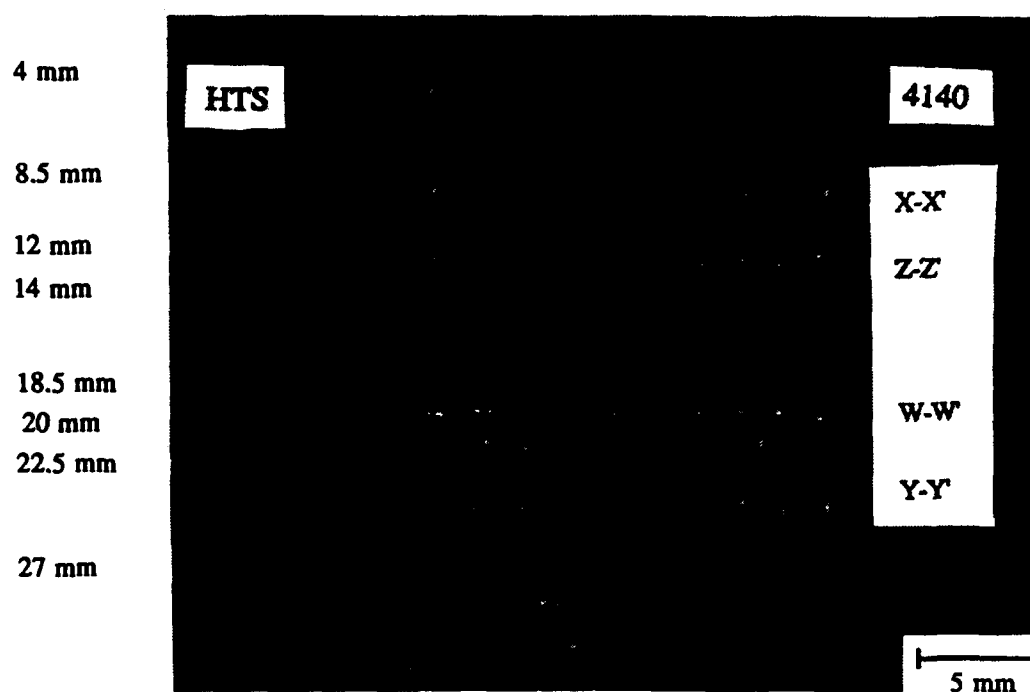


Figure 3.22: Macrograph of Cross-Section Used in Rockwell "C" Hardness Tests.

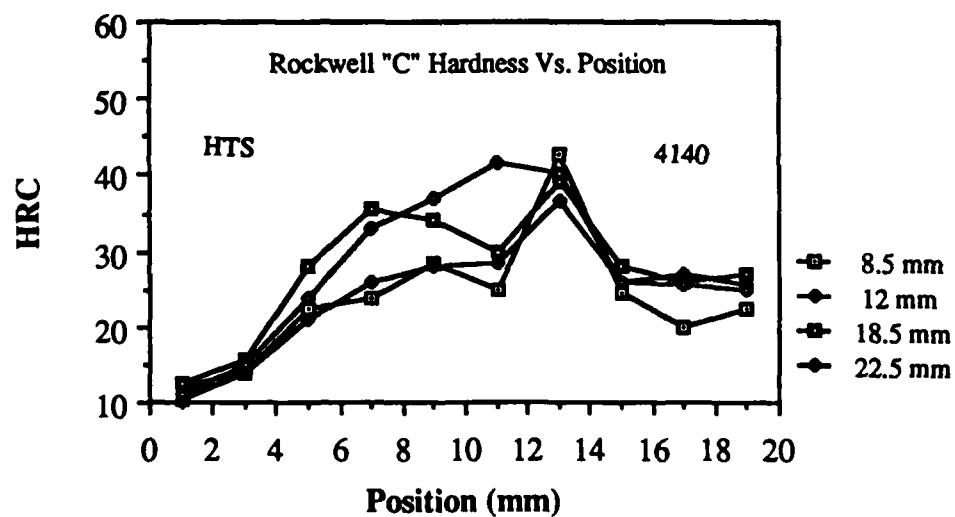


Figure 3.23: Rockwell "C" Hardness Versus Position for Various Depths within Cross-Section.

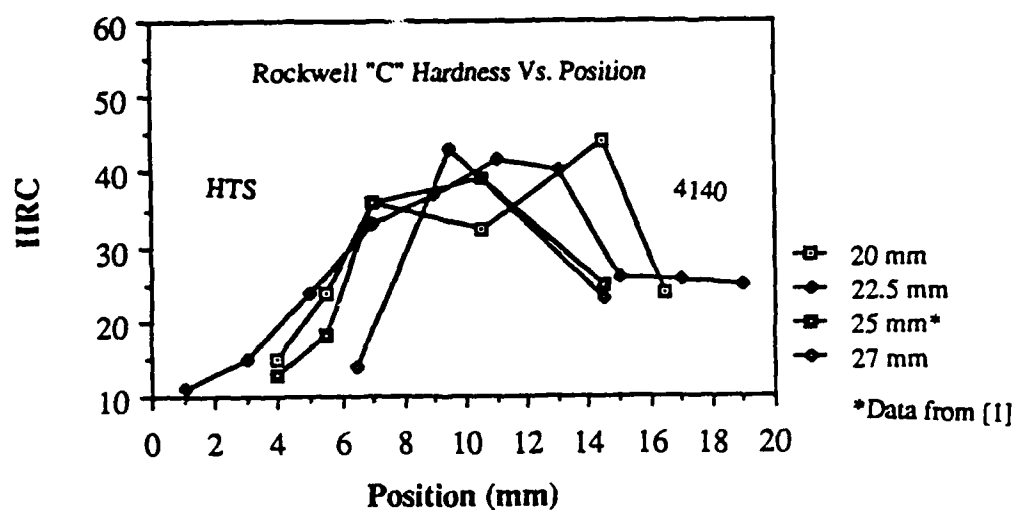


Figure 3.24: Rockwell "C" Hardness Versus Position for Specimens at Depths of 20-28 mm.

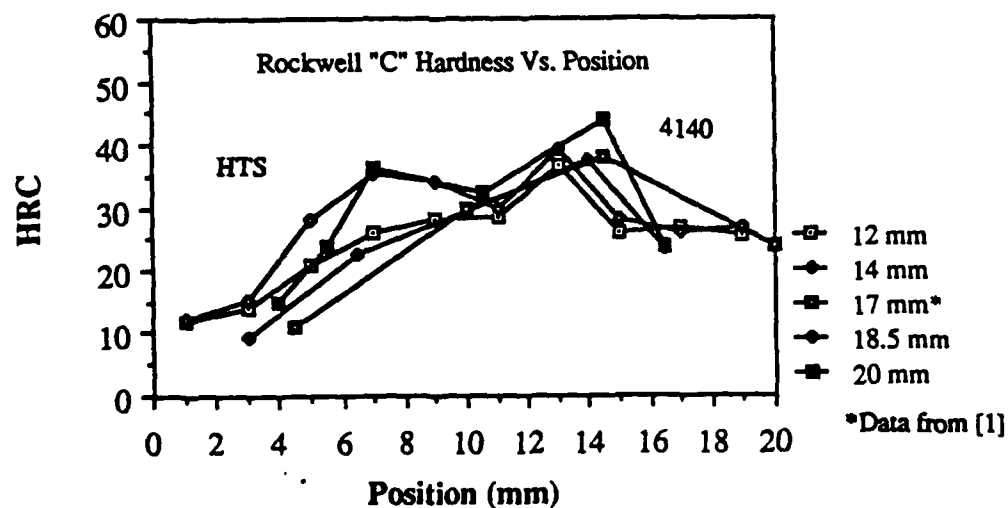


Figure 3.25: Rockwell "C" Hardness Versus Position for Specimens at Depths of 12-20 mm.

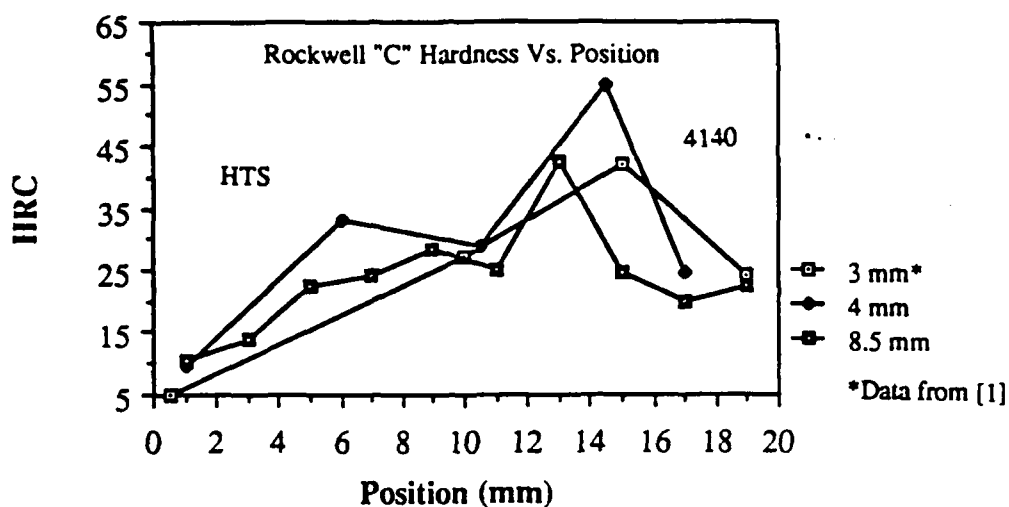


Figure 3.26: Rockwell "C" Hardness Versus Position for Specimens at Depths of 3-8 mm.

### 3.3.3 Fracture Surface Porosity

The fracture surfaces of the CT-specimens were used in porosity evaluations. All specimens fell into one of four groups according to which weldment zone had been tested in the fatigue experiments; the specimen groups are those listed in Table 3.2. Each fracture surface exhibited a fatigue region and a final fracture region. The fracture surface of specimen #23 shown at 3X in Figure 3.27 shows a smooth region of fatigue crack growth and a region of fast fracture characterized by plastic deformation; such deformation is clearly seen around the border. The fracture surfaces from five specimens were photographed and the negatives were printed at a magnification of 6X for use in the porosity evaluation procedure. Porosity levels were assessed separately within the fatigue and fast fracture regions for each of these specimens.



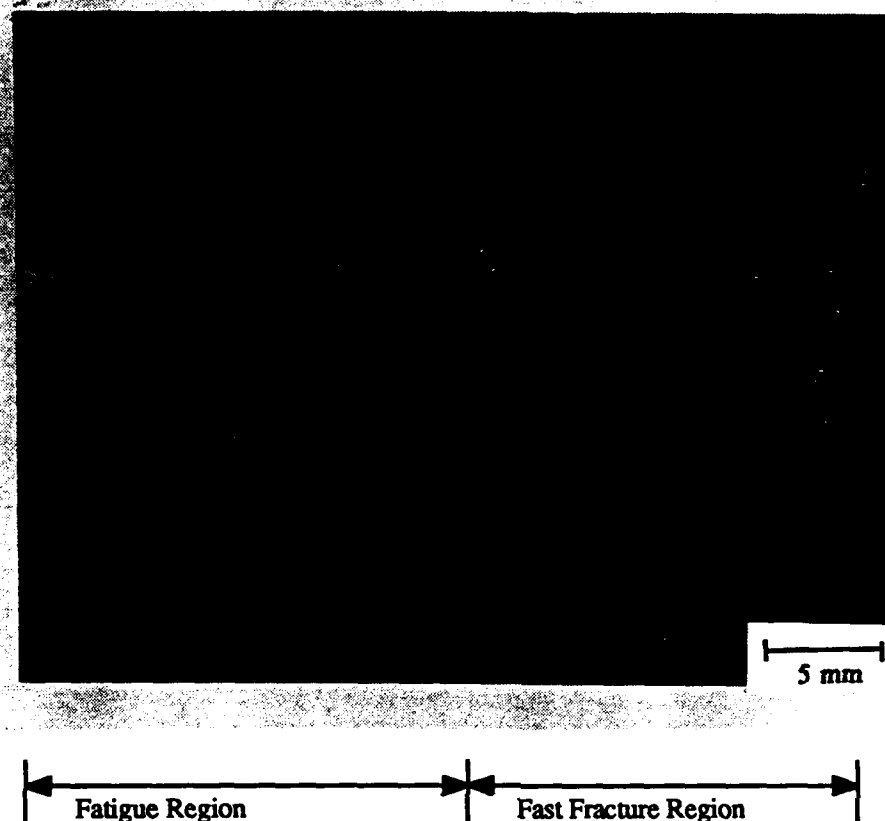


Figure 3.27: Fracture Surface of Specimen #23 Showing Fatigue and Fast Fracture Regions.

Table 3.2 CT-Specimen Numbers and the Regions Tested

<u>Specimen #</u>	<u>Region tested</u>
1,2,3,12,13	weld center
11,21,22	4140 HAZ
23,24,31	HTS HAZ N
32,33,34	HTS HAZ F

### 3.4 Compact-Tension (CT) Specimen Fabrication

The original weldment used measured 183 cm long by 20.3 cm wide and had a variable cross-section. After fabrication of the weldment, the material was sectioned into four pieces, each measuring 45.7 cm long by 20.3 cm wide. The materials used to make the weldment were the actual size and shape of the specific application for which the weldment was considered; a trough cover and track for a catapult launch system. The irregular cross-section of the weldment was a result of this intended application. Two of the four sections of the weldment were as sketched in Figure 3.28 (A), and three CT-specimens were cut from each of these. The other two sections appeared as shown in Figure 3.28 (B); each of these sections yielded four CT-specimens. The banded region near the center of the plates in Figure 3.28 represents the location of the weld.

Fabrication of the CT-specimens began by sectioning each of the four plates. For example, specimens #1, #2 and #3 were cut from one plate as follows: The plate was sectioned as shown in Figure 3.29. Each of the 60.3 mm wide blocks originally had a cross-section as shown in Figure 3.29, the blocks were milled from both sides to a uniform thickness of 9.5 mm. Each of the blocks was then cut from both ends to a final length of 63.5 mm centered around the weld. The location of the CT-specimens #1, #2 and #3 with respect to the block and the weld is shown in Figure 3.29, these specimens were centered on the weld center.

The other CT-specimens were centered around various regions of the weld in order to study corrosion fatigue through the heat-affected zones as well as through the weld center. Table 3.2 lists the specimen number and the region tested for each specimen. In each case the root of the notch coincided with the region to be tested. Each specimen contained a 1.6 mm radius edge groove on its back side which was centered on the notch root, was parallel to the direction of crack propagation and served to restrain the crack, causing it to propagate in the same region throughout the test. The final dimensions for the CT-specimens are given in Figure 3.30.

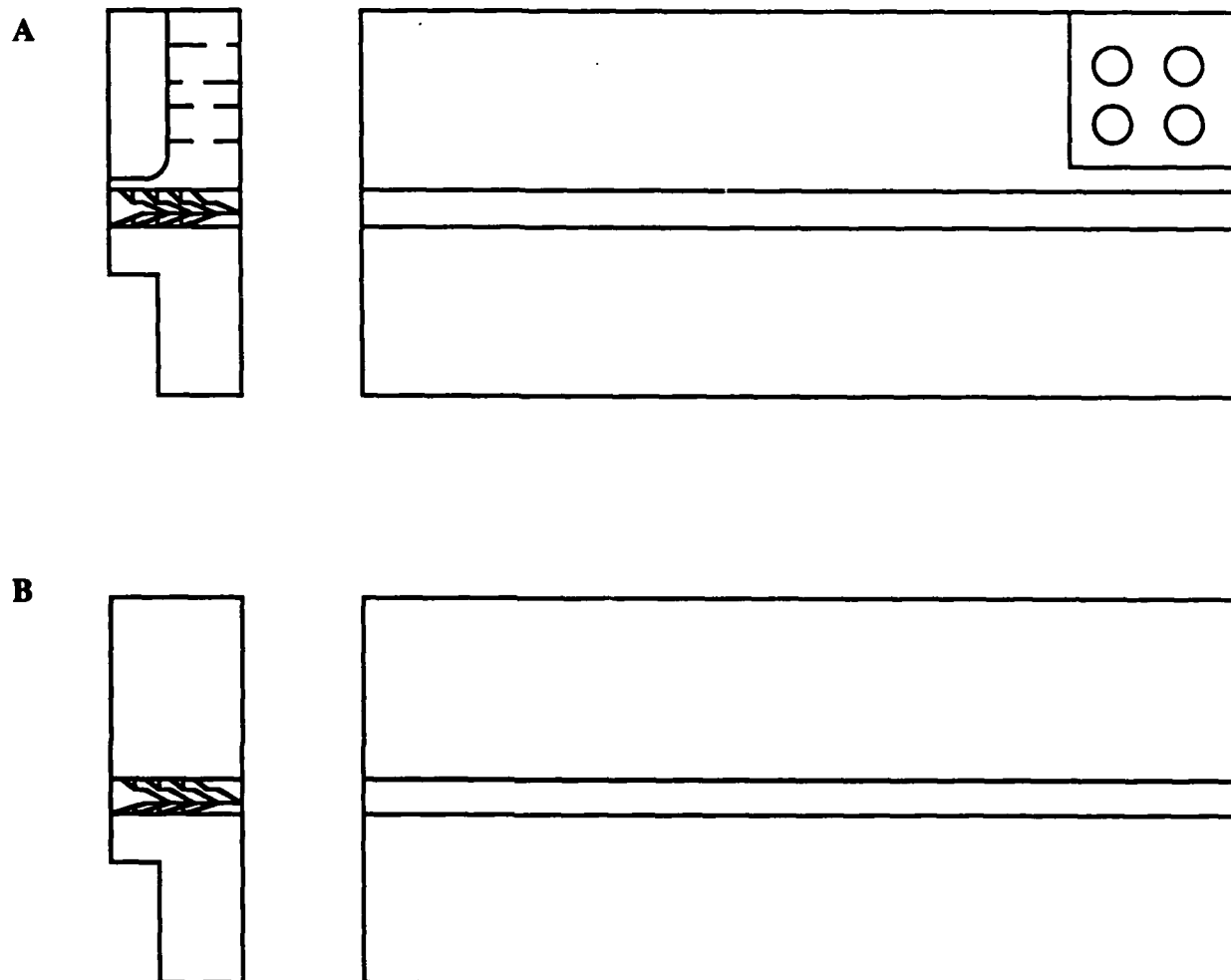


Figure 3.28: Original Weldment Sections Which Yielded Three CT-Specimens (A), and Four CT-Specimens (B).

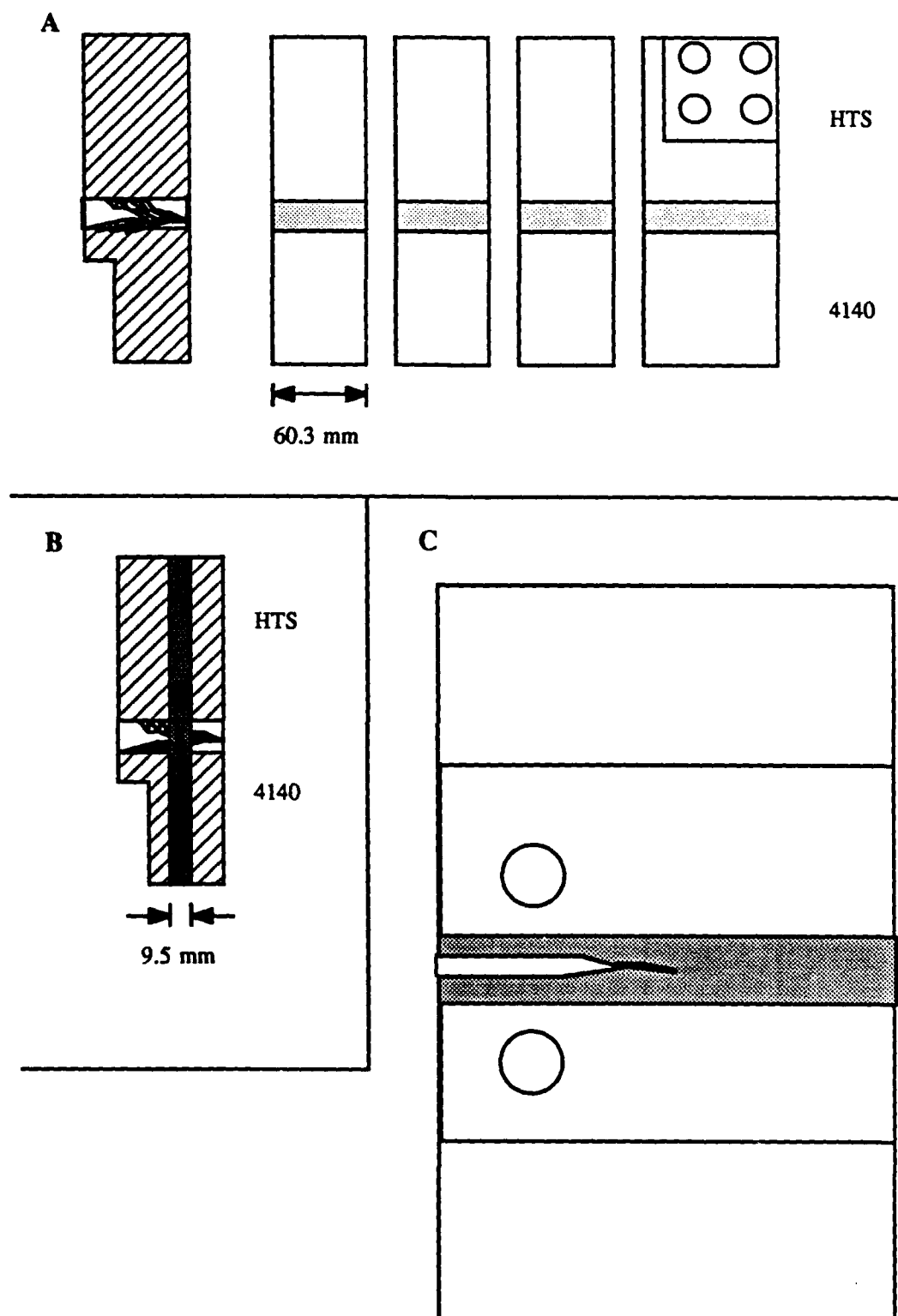
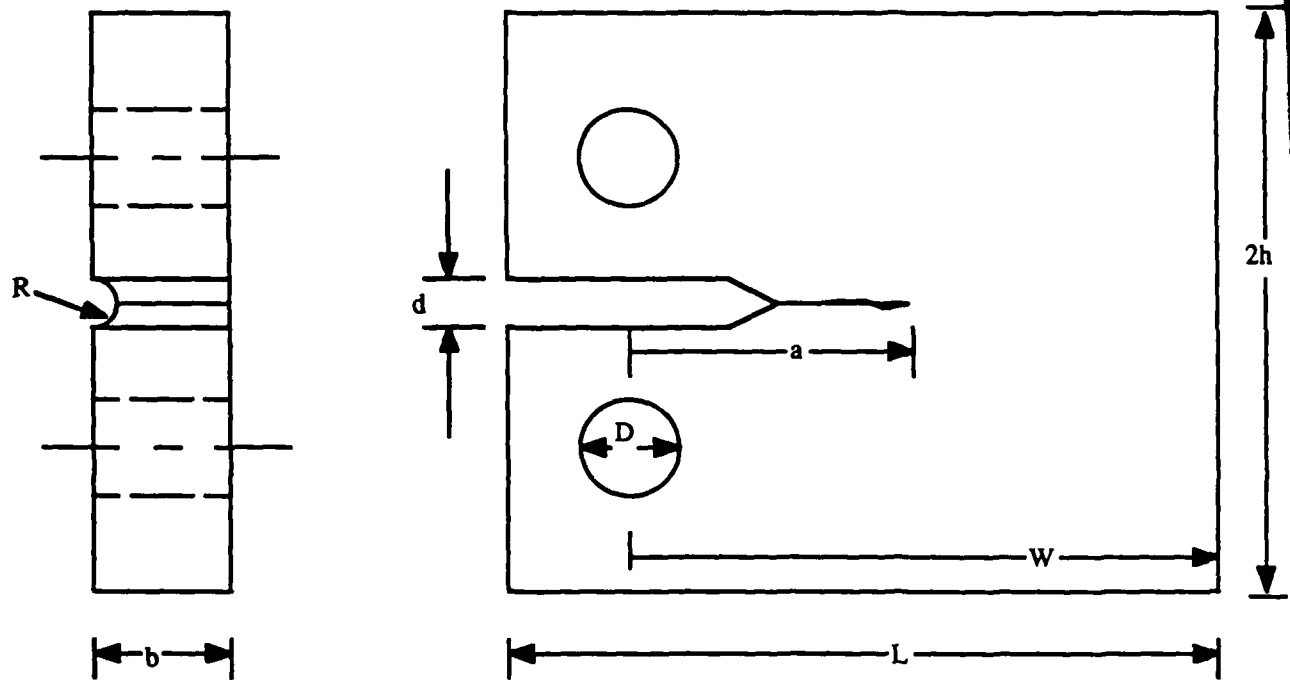


Figure 3.29: Steps in CT-Specimen Fabrication. Sectioning Original Plate (A), Milling Cross-Section to Uniform Thickness (B) and Locating Specimen Notch Center with respect to Weld (C).



$L=5.7150$  cm  
 $W=4.4450$  cm  
 $2h=6.3500$  cm  
 $b=0.8255$  cm  
 $D=1.2700$  cm  
 $a=1.2700$  cm  
 $d=0.3175$  cm  
 $R=0.1600$  cm

Figure 3.30: Dimensions of CT-Specimen.

## Chapter 4

### EXPERIMENTAL PROCEDURES

#### 4.1 Introduction

The primary experimental focus of this study was on the collection of fatigue data from CT-specimens tested in air and in salt water. The details of the various testing apparatus and methods are presented in this chapter.

#### 4.2 Fatigue Tests

The fatigue resistance and corrosion-fatigue resistance, determined as fatigue crack propagation rates, of the HTS/4140 weldments were tested for within various weld regions using the CT-specimens. Room temperature tests were run in air and in 3.5 volume percent NaCl solution; test frequencies of one and five Hertz were used in each environment. Load control testing using a sinusoidal waveform was done on an Instron Model 8000 Servohydraulic Control System equipped with a 100 kN capacity dynamic load cell. A Hewlett-Packard microprocessor controlled the testing program and provided a record of the load history and the number of cycles data.

##### 4.2.1 Apparatus

An environmental chamber was designed and constructed to attach to the actuator-driven piston on the Instron and surround the CT-specimen during fatigue testing. The chamber consisted of a 7.6 liter clear polycarbonate jar which was connected to one of two stainless steel specimen grips via a hole in its bottom; the jar was supported by an aluminum base built up around the specimen grip. The system was bolted together from the inside and the entire region was sealed with silicone gasket to prevent leakage and any interaction of the bolt metal with the salt water solution.

Two specimen grips and two pins were machined from type 431 stainless steel and then heat-treated to obtain a minimum tensile strength of 700 MPa. One grip had been attached to the chamber as described above and then connected to the piston on the Instron, the other grip was connected to a universal joint which provided ease of specimen insertion and removal, and then to the load cell attached to the Instron. The entire load train including the environmental chamber, specimen grips and a specimen is sketched in Figure 4.1.

#### 4.2.2 Data Collection

Crack-propagation strain gages were mounted to the side of the CT-specimens at a distance of 0.05 mm ahead of the notch, sufficient to insure that the crack had extended past any machining effects prior to encountering the strain gage; Micro-Measurements TK-09-CPA01-005 gages were used. These gages consisted of twenty foils separated by 0.025 cm and connected in parallel to copper-plated soldering tabs. The effective resistance across the gage with all twenty foils intact was  $5.4 \pm 10.0\% \Omega$ . Lead wires connected these tabs to a Houston Instrument 3000 Strip-Chart Recorder and a Keithley 225 Current Source; the resulting circuit is sketched in Figure 4.2.

A crack propagating across the strain gage would cause each of the twenty foils on the gage to break one by one until final fracture of the specimen occurred. Each time a foil broke on the gage the effective resistance across the soldering tabs increased. Forcing a constant current across the gage resulted in an increase in the voltage input into the strip-chart recorder to coincide with every break in a gage foil. The pen on the recorder tracked the voltage versus time record of the test which could then be converted to crack length versus number of cycles data using the position of the gage and the test frequency.

#### 4.2.3 Test Procedure

Before each corrosion-fatigue specimen was mounted, calibration of the system was performed to ensure optimal response of the load train with respect to the microprocessor control. The grips and pins were coated with polyurethane to prevent interaction with the specimen metals, the strain gages and lead wires on those specimens which were to be tested in the salt water were also isolated from the solution by a thin layer of polyurethane coating. Once the coatings dried the chamber was filled with 3 L of 3.5% NaCl solution. A dummy specimen possessing a similar tensile stiffness as the test specimens was inserted in the grips and the position and load response of the piston and load cell were calibrated for the system. The dummy specimen was then removed, a test specimen installed and the test started. The response of the testing apparatus depended not only on the specimen stiffness, but also on the weight of the load train; because this weight differed depending on whether testing was done in air or in salt water, the tests in air required a similar calibration procedure. Each of these tests was conducted using the same load train and included the environmental chamber, filled or not.

The typical test on a specimen, whether in air or in salt water, consisted of an initial run at a relatively high stress range until a visible crack was noted. The stress was then lowered to allow the crack to propagate through the gage. Often the crack extended through the entire gage before approaching the fracture toughness conditions as would be manifested in a very rapid crack propagation rate. When this occurred the test was interrupted and a second gage was applied ahead of the crack. The test was then restarted at a cyclic stress intensity near that at which the previous run had been interrupted in order to expand the range of the data.



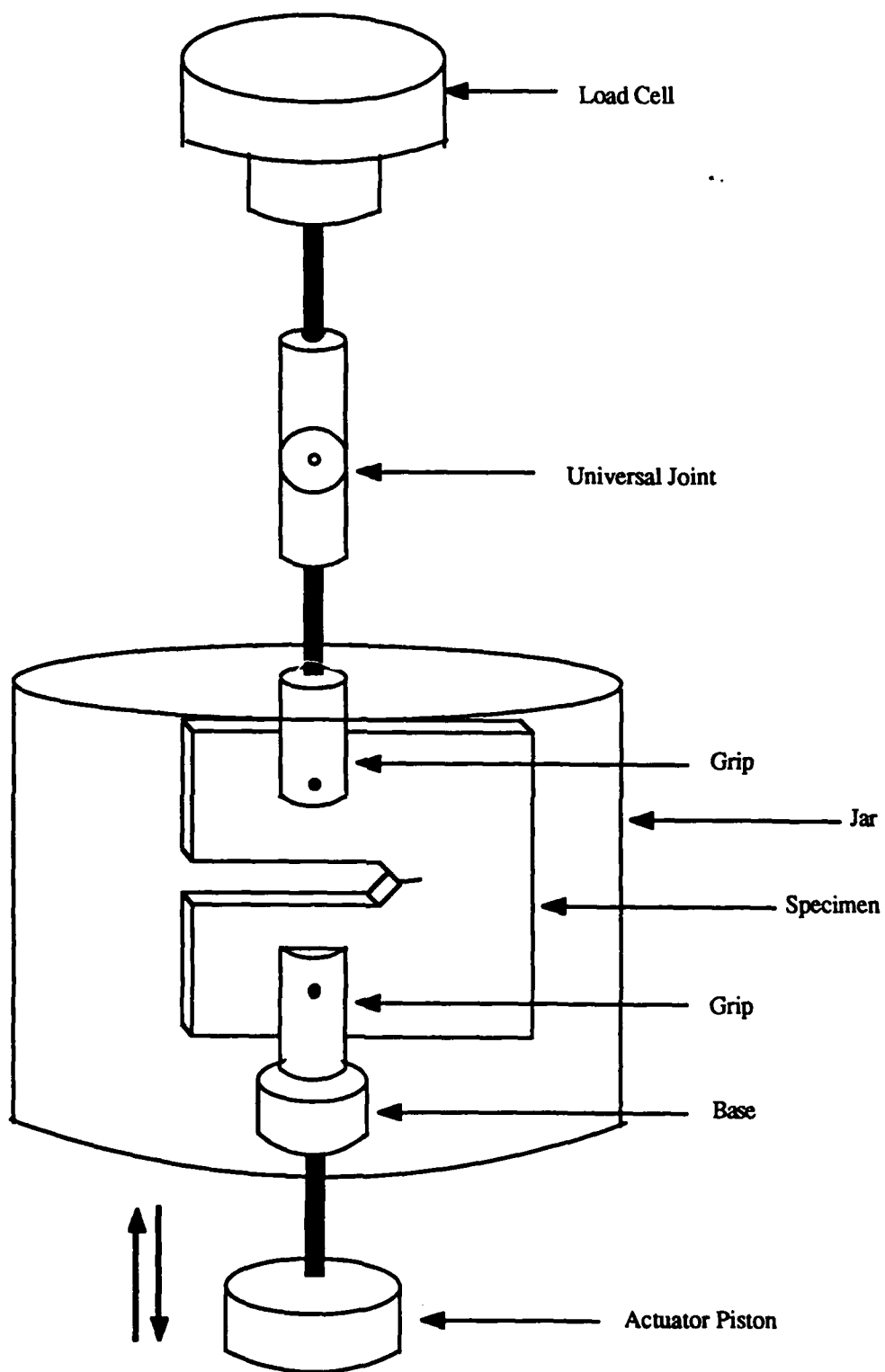


Figure 4.1: Sketch of Entire Apparatus for Fatigue Tests.

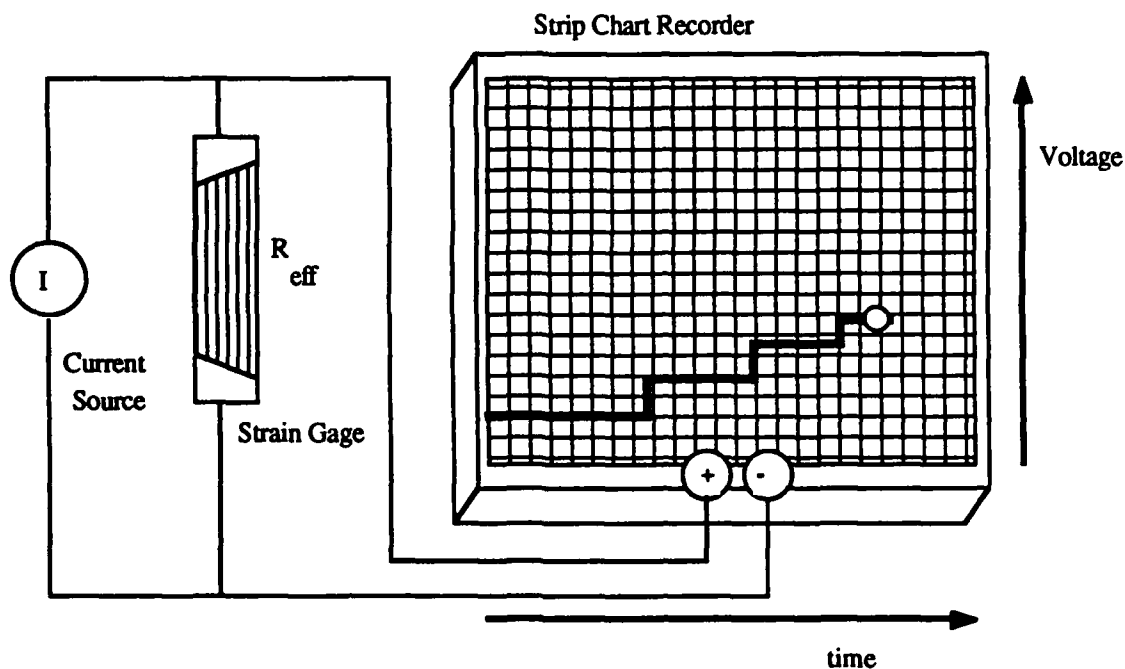


Figure 4.2: Sketch of Circuit Used in Crack Propagation Data Acquisition.

#### 4.3 Treatment of Data

The raw data collected from the strip-chart recorder for a given fatigue test consisted of a record of the voltage input to the recorder versus time. These data were enhanced by an independent record of cycle number and maximum and minimum load peaks which could be printed from the microprocessor control at any time during the test. These records were used in conjunction with the specimen dimensions and test frequency to determine crack growth rate versus stress intensity relationships and fracture toughness values for all test conditions. The details of the steps involved in treating the data are discussed in this section.

#### 4.3.1 Crack Length Versus Number of Cycles Data

Figure 4.2 shows schematically the change in voltage associated with the advancement of the crack tip across a foil on the crack propagation strain gage. The crack length associated with each voltage increase is known from the location of the gage on the face of the specimen. Crack length data could be recorded for every foil position on the strain gage once that foil was broken.

The number of cycles data was calculated from conversion of the time record on the strip-chart recorder. As the graph paper traveled past the pen on the strip-chart recorder at a known rate, the distance the paper traveled between voltage increases was easily measured from the record left by the pen on the paper. These quantities were used with the test frequency to determine the number of cycles accumulated between each crack tip advance across a foil on the strain gage as follows:

$$\Delta N = \nu L \left( \frac{1}{V} \right) \quad (4.1)$$

where  $\Delta N$  is the number of cycles,  $\nu$  is the test frequency in cycles per second,  $V$  is the velocity of the paper on the strip-chart recorder in centimeters per second and  $L$  is the distance the paper traveled between voltage change events in centimeters. The number of cycles accumulated during the time it took the crack to extend from one foil on the strain gage to the next was computed as  $\Delta N$  above. The total number of cycles accumulated was found for a given crack length by adding  $\Delta N$  to the previous total number of cycles:  $N_T = N_{T(\text{previous})} + \Delta N$ .

Specimens were often subjected to several runs as was mentioned in Section 4.2.3. The test conditions were often changed for a given specimen if it was determined that the crack was growing too slowly or too rapidly for data accumulation in a particular test.

Each time the applied load was changed another run was counted; the cycle count for an individual run was started at  $N_T = 0$  regardless of whether the specimen had undergone previous runs.

A change in the applied load level is accompanied by a change in the size of the plastic zone ahead of the crack tip. A growing crack subjected to such a change in applied load is still under the influence of the plastic zone that existed prior to the load change. This crack must grow beyond the prior plastic zone before it can be considered to be growing due to the conditions of the present test [38]. The cyclic plastic zone size for a material whose yield strength is  $\sigma_{ys}$  is given as [39]:

$$r_y = \left(\frac{1}{2\pi}\right) \left(\frac{\Delta K_I}{2\sigma_{ys}}\right)^2 \quad (4.2)$$

when the stress intensity range is  $\Delta K_I$ . The size of the plastic zone was determined for the crack lengths at the end of all runs preceding runs for which data were collected. Data points for any run which were found to lie within the plastic zone of the previous run were disregarded. All remaining crack length versus number of cycles data have been tabulated in Appendix A.

#### 4.3.2 Computing $da/dN$ Versus $\Delta K_{eff}$ Data

The crack growth rate, written as  $da/dN$ , is defined as the slope of the curve fitted to the crack length versus number of cycles data. An example of the curve fitting procedure is sketched in Figure 4.3. Crack growth rates were determined as follows: each set of crack length versus number of cycles data was plotted and fitted with a smooth curve using a french curve as a guide to insure the smoothness of the fit. The tangent to the curve at a crack length  $a'$  was drawn, the rate of change of the crack length at that point was

calculated from the slope of the tangent line. Slopes were measured graphically for several crack lengths on the curve within the range of the data. These slopes, in units of meters/cycle, represented the growth rates for the chosen crack lengths.

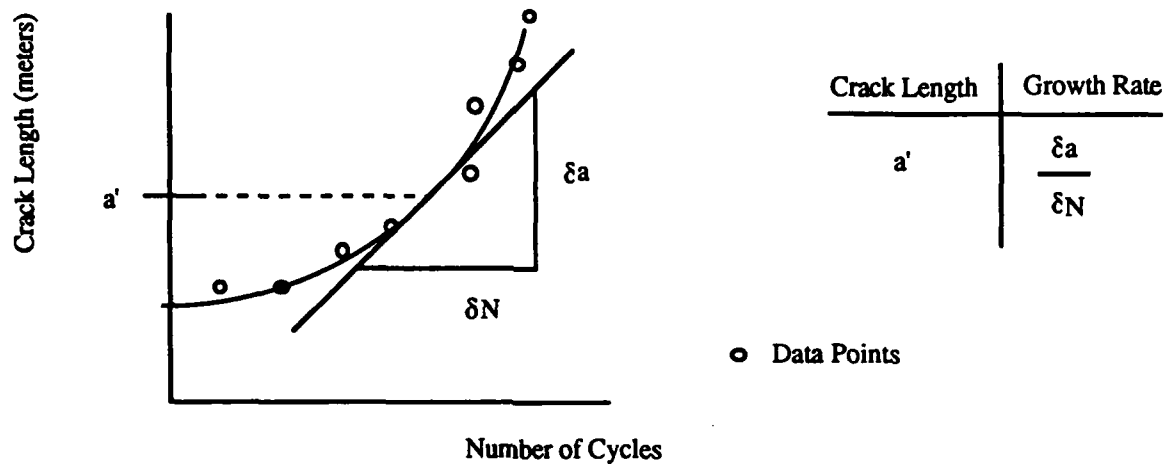


Figure 4.3: Example Sketch of Curve Fit Used to Determine Crack Growth Rates.

The stress intensity range for a CT-Specimen under a fluctuating load is given by Equation 4.3 [39].

$$\Delta K = \frac{(\Delta P)}{(b \sqrt{w})} \frac{(2 + \frac{a}{w})}{\sqrt[3]{(1 - \frac{a}{w})}} \Phi(\frac{a}{w}), \quad (4.3)$$

where

$$\Phi\left(\frac{a}{w}\right) = 0.866 + 4.64 \left(\frac{a}{w}\right) - 13.32 \left(\frac{a}{w}\right)^2 + 14.72 \left(\frac{a}{w}\right)^3 - 5.6 \left(\frac{a}{w}\right)^4.$$

Specimen dimensions  $w$  and  $b$  are the width and thickness, respectively, of the CT-Specimen and  $\Delta P$  is the load range. The effect of the minimum load to maximum load ratio,  $R$ , on crack growth rates, can be accounted for using the Schijve relation that was given as Equation 2.9,

$$\Delta K_{\text{eff}} = \Delta K (0.55 + 0.35R + 0.1R^2). \quad (2.9)$$

The effective stress intensity range,  $\Delta K_{\text{eff}}$ , was calculated for each of the same crack lengths whose growth rates were determined from the curve fitting calculations. These crack growth rate versus stress intensity range data pairs have been listed in Appendix B and the specimen dimensions and load ratios for each successful run are given in Appendix C.

#### 4.3.3 The Crack Growth Rate Law

Accounting for the effect of the load ratio,  $R$ , on the crack growth rates through the use of  $\Delta K_{\text{eff}}$  allows the following modified version of the Paris law [39] to describe the crack growth:

$$\frac{da}{dN} = C (\Delta K_{\text{eff}})^m. \quad (4.4)$$

A linear relationship results for the  $da/dN$  -  $\Delta K_{\text{eff}}$  plots on logarithmic axes;

$$\log \left( \frac{da}{dN} \right) = m (\log (\Delta K_{\text{eff}})) + \log (C). \quad (4.5)$$

#### 4.3.4 Fracture Toughness Calculations

Final failure of the CT-Specimen often occurred beyond the crack propagation strain gages; therefore, final crack progress was determined from a fractured specimen as the point of incipient gross plastic deformation. This feature was accompanied by a sharp change in the direction of the crack path into the HTS base metal. A typical fracture pattern is shown in Figure 4.4 for a specimen with the crack growing in the weld center that turned sharply into the HTS region, then turned again and propagated rapidly. Gross plastic deformation occurs in conjunction with these turns as is evident from the sketch of the top view of the fracture surface in Figure 4.4.

#### 4.4 Treatment of Fractured Specimens

Every specimen was subjected to runs until it failed. The specimens were examined to insure that the crack remained within the same region throughout its propagation stage as constrained by the side grooves. In many cases the crack was found to turn 90°, run into the HTS region and turn again. These turns occurred during the final fracture stage and not during the propagation stage. One-half of each failed specimen was sent to Westinghouse for cleaning using ENDOX 214 as described by Yuzawich and Hughes [40]. The corrosion products were removed from the specimens in order to study the underlying fracture surfaces under the Scanning Electron Microscope (SEM). Once cleaned, these specimens were coated with urethane to preserve the clean fracture surfaces until SEM analysis could be performed. Five of these surfaces were also used in the porosity evaluations. The other half of each specimen was wrapped and stored under a vacuum so as to preserve the corrosion products on the fracture surfaces for SEM analysis.

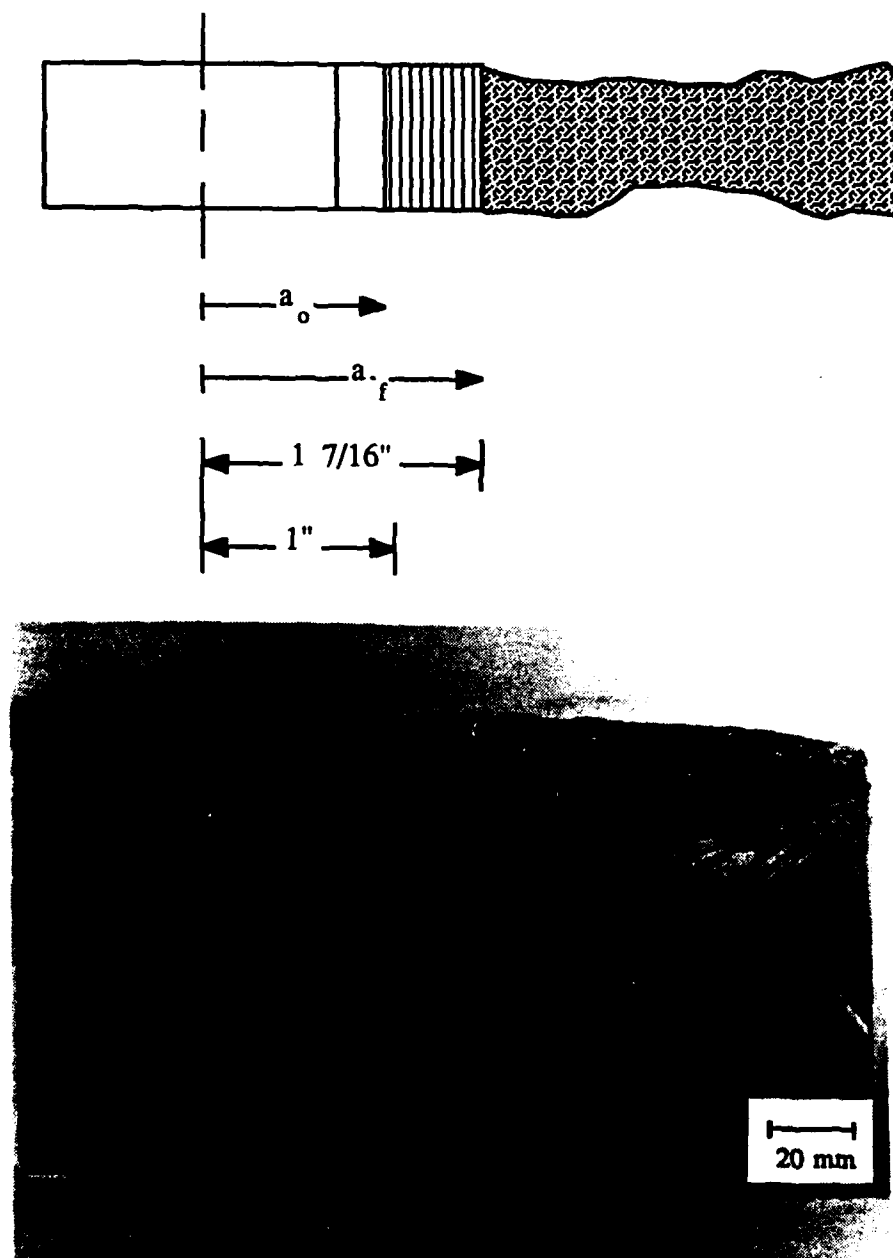


Figure 4.4: Fractured Specimen Showing Crack Path and Gross Plastic Deformation.



#### 4.5 Porosity Determination

The volume fraction of porosity was determined from the magnified fracture surfaces of five specimens using a point counting method adapted from DeHoff and Rhines [41]. Success of the point counting method depends upon the appropriate selection of grid sizes based on the size of the porosity "phase." An optimal grid would intersect with an individual phase occurrence, or pore, on an average of one intersection per pore. Grids of different sizes were fabricated to satisfy this criterion for the different pore sizes found within the fracture surfaces of the five specimens.

## Chapter 5

### RESULTS

#### 5.1 Fatigue Data

The crack growth rate versus stress intensity range data have been plotted on logarithmic axes in Figures 5.1 to 5.8. The data are grouped and plotted according to two different schemes. The data in Figures 5.1 to 5.4 were grouped according to the region of weldment tested, which was either HTS HAZ F, HTS HAZ N, weld center or 4140 HAZ. The data were also grouped into one of the following test conditions: in salt water at one Hertz, in air at one Hertz, in salt water at five Hertz or in air at five Hertz; Figures 5.5 to 5.8 present plots of the data grouped according to test conditions.

A straight line was fitted through the crack growth rate versus stress intensity range data points for each run to determine the constants  $C$  and  $m$  in the crack growth rate law of Equation 4.5. The data from runs in salt water in the HTS HAZ F and 4140 HAZ regions showed a transition to a lower slope at intermediate  $\Delta K_{eff}$  values. The onset of this transition stage results in a kink in the  $da/dN$  vs.  $\Delta K_{eff}$  curves of Figures 5.1 to 5.8. The data points for the runs in salt water were fitted to the crack growth law in this transition stage, where observed, using only data points from within this region; the constants  $C$  and  $m$  are listed in Table 5.1 for each successful air and salt water run. The  $\Delta K_{eff}$  levels at the onset and the end of the transition stage are given in Table 5.2. The individual runs including the straight line fits have been plotted in Appendix D.

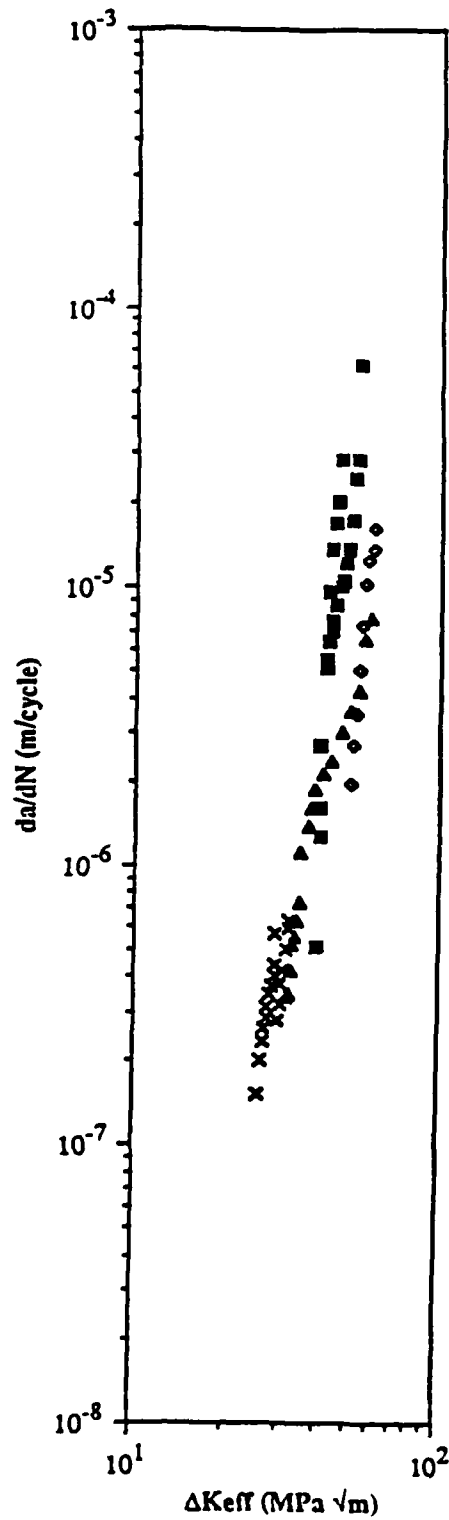


Figure 5.1: All Runs in the HTS HAZ F.

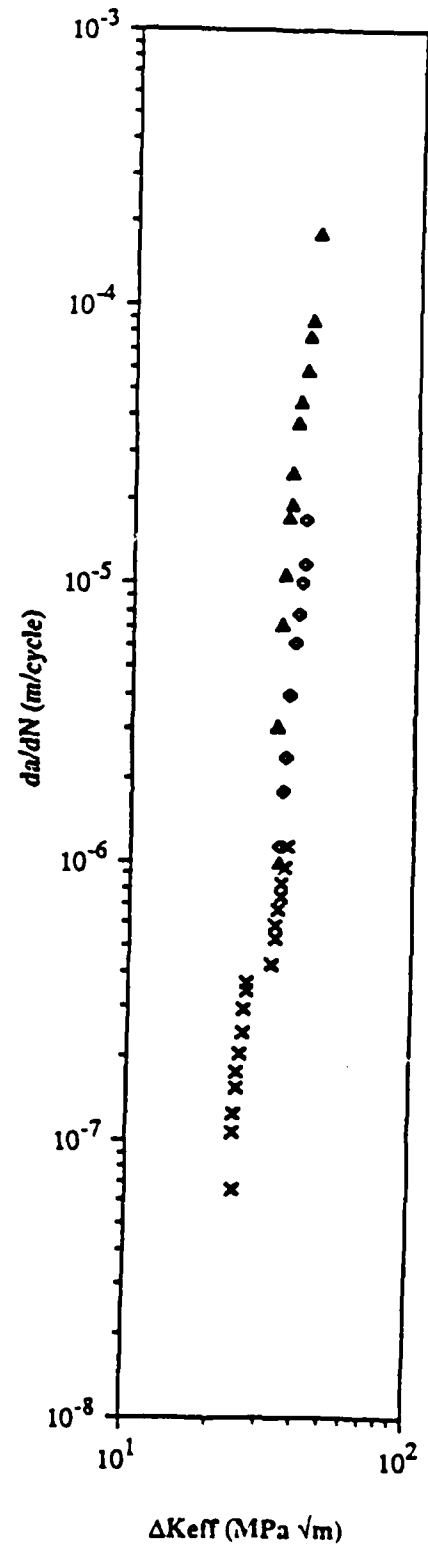


Figure 5.2: All Runs in the HTS HAZ N.

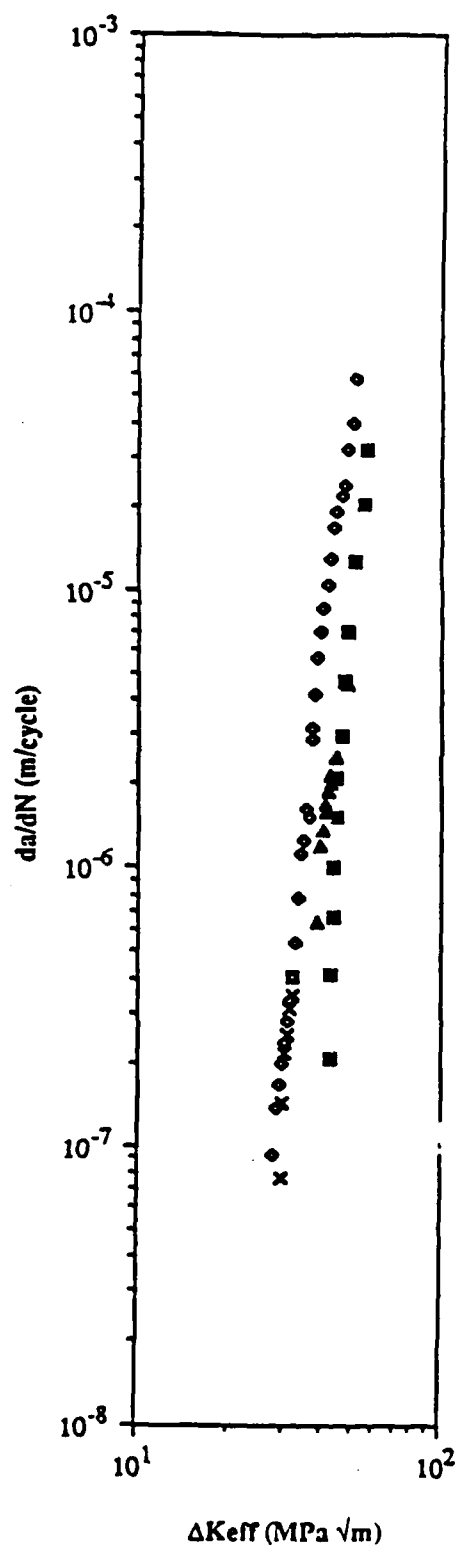


Figure 5.3: All Runs in the Weld Center.

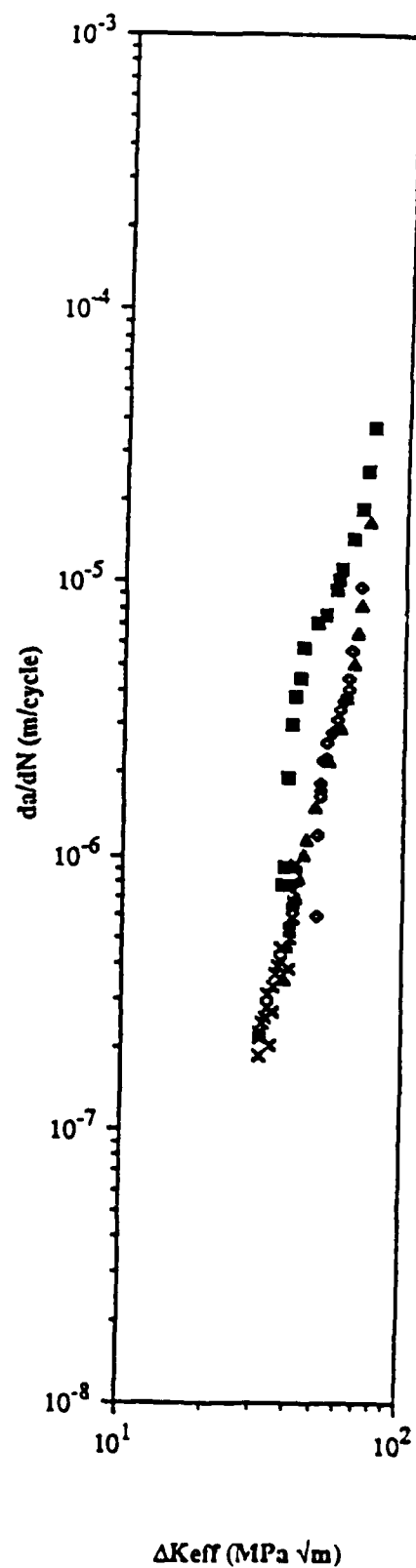


Figure 5.4: All Runs in the 4140 HAZ.

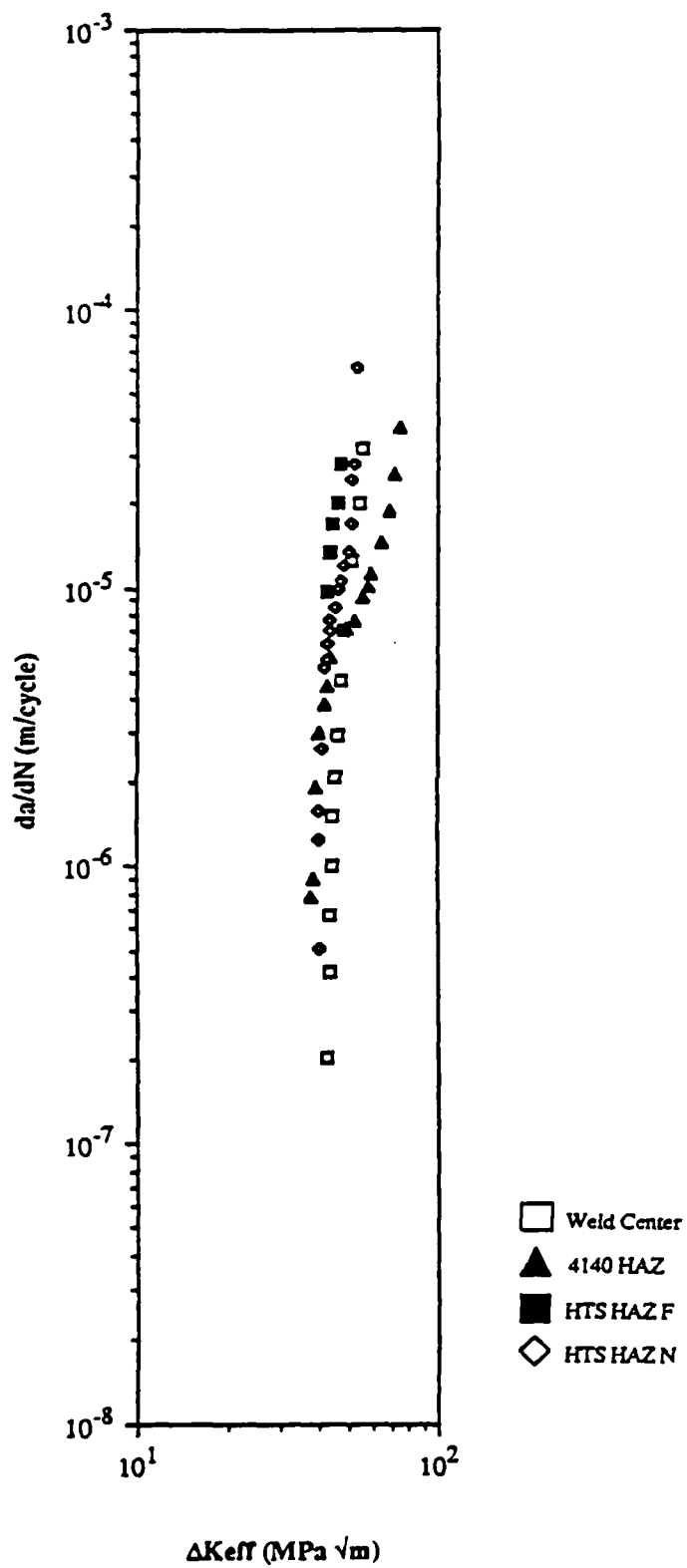


Figure 5.5: All Runs in Salt Water at 1 Hz.

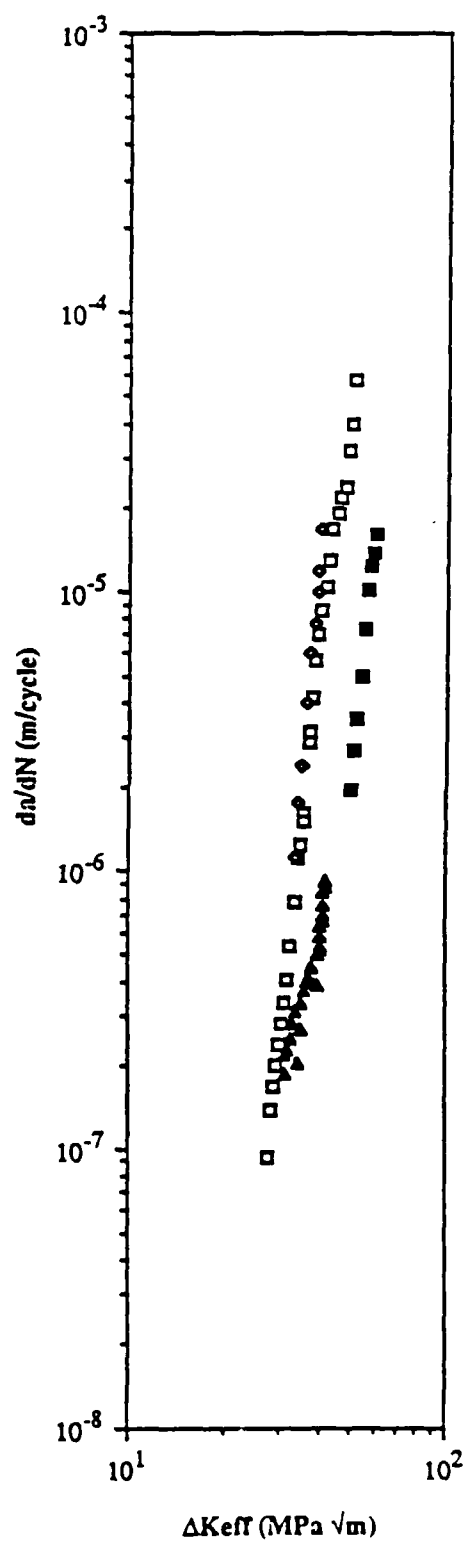


Figure 5.6: All Runs in Air at 1 Hz.

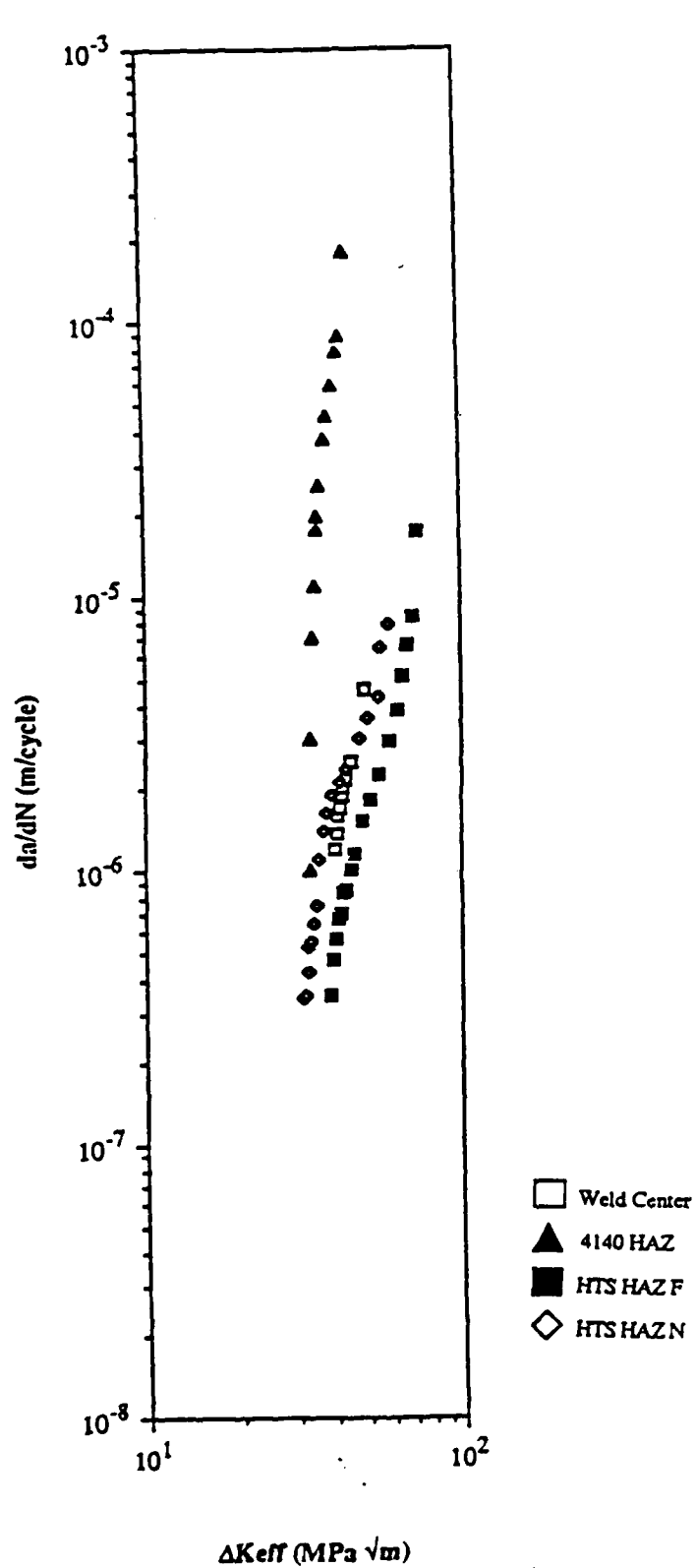


Figure 5.7: All Runs in Salt Water at 5 Hz.

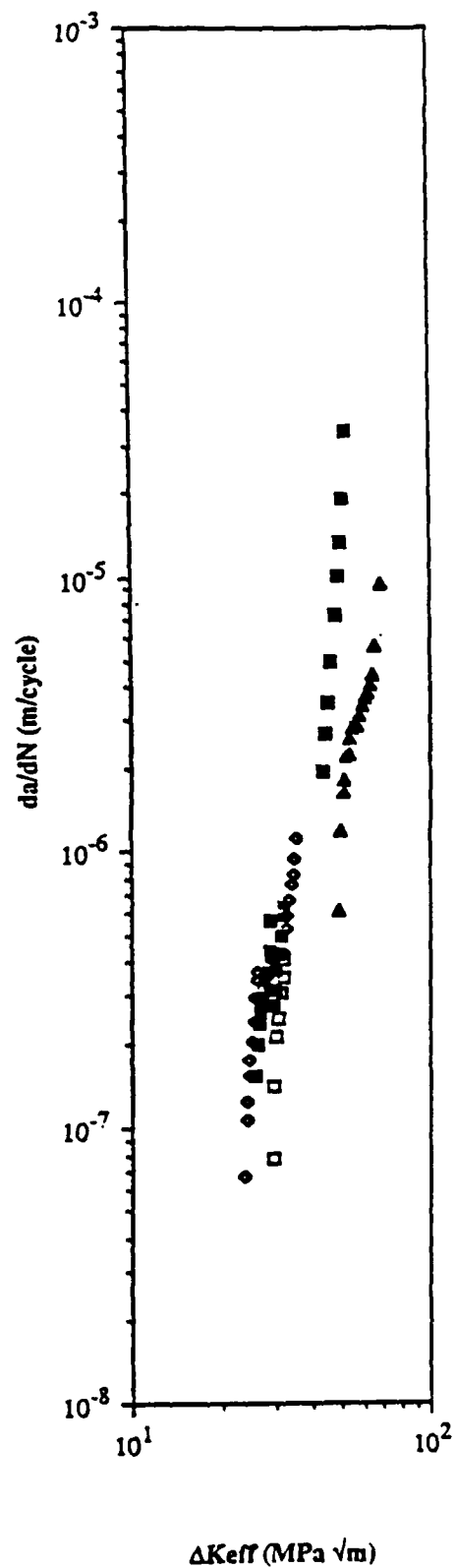


Figure 5.8: All Runs in Air at 5 Hz.

Table 5.1 Constants C and m from Equation 4.5

<u>Specimen, Run</u>	<u>Runs in Air</u>		<u>Runs in Salt Water</u>	
	<u>Coefficient: C</u>	<u>Exponent: m</u>	<u>Coefficient: C</u>	<u>Exponent: m</u>
1,1	4.16E-22	9.6		
3,4	2.32E-21	9.4		
3,7	9.66E-23	10.4		
3,8	1.93E-22	10.3		
12,2			4.68E-17	6.6
11,2	7.91E-20	8.5		
11,4	1.10E-21	10.2		
11,5	7.48E-23	10.8		
21,5			3.71E-19	8.9
23,4	2.94E-26	12.0		
23,6	2.01E-19	7.9		
23,8	9.52E-16	5.6		
23,9	7.91E-13	3.8 (T)*		
24,2			1.90E-13	4.1 (T)
31,2			2.56E-10	2.6 (T)
32,7	8.10E-21	9.2		
32,10	3.54E-19	8.3		
32,12	6.17E-23	9.8		
33,2			6.67E-11	2.8 (T)
34,4			2.20E-20	9.0
34,5			9.79E-15	5.4 (T)

\* (T) Denotes data from the transition stage.

Table 5.2 Values of  $\Delta K_{eff}$  at Transition Onset ( $\Delta K_{eff T}$ ) and End ( $\Delta K_{eff III}$ )

<u>Region</u>	<u><math>\Delta K_{eff T}</math></u> <u>(MPa<math>\sqrt{m}</math>)</u>	<u><math>\Delta K_{eff III}</math></u> <u>(MPa<math>\sqrt{m}</math>)</u>	<u>Frequency, Environment</u>
HTS HAZ F	42	51	SW, 1 Hz
	38	54	SW, 5 Hz
4140 HAZ	43	68	SW, 1 Hz
	41	67	SW, 5 Hz
	52	63	Air, 5 Hz

Table 5.3 Estimated Strengths For Weldment Regions

<u>Region</u>	<u>HRC (ave.)</u>	<u><math>\sigma_{UTS}</math> (MPa)</u>
HTS HAZ N	34.0	1055
HTS HAZ F	22.5	779
weld center	31.5	985
4140 HAZ	41.0	1296



## 5.2 Results of Fracture Toughness Calculations

The plastic zone sizes within each of the specimens were calculated for the critical crack lengths and compared to the specimen widths to determine whether plane strain or plane stress conditions existed at the time of final fracture. The yield strengths needed in this calculation were estimated at 70% of the corresponding tensile strengths which were found using the hardness data in Figure 3.26 for the four regions tested. The estimated strengths for the HTS HAZ F, HTS HAZ N, weld center and 4140 HAZ were used in the determination of the plastic zone sizes at fracture according to Equation 4.2 and are listed in Table 5.3.

The fracture toughness values were computed for each specimen by substituting the maximum load,  $P_{\max}$ , for  $\Delta P$  in Equation 4.3. The final crack lengths,  $a_f$ , were taken as the distance from the plane of application of the load to the point of incipient gross plastic deformation. The fracture toughness values and final plastic zone sizes are given in Table 5.4. All final crack lengths and  $P_{\max}$  data have been tabulated in Appendix E.

Table 5.4 Fracture Toughness Values and Final Plastic Zone Sizes

Specimen	$K_{IC}$ (MPa $\sqrt{m}$ )	$\Delta K = K_{IC}(1-R)$	$r_p$ (m)
1	107	96	0.00077=0.094b
2	105	94	0.00074=0.074b
3	106	93	0.00072=0.086b
12	103	86	0.00066=0.077b
13	112	98	0.00080=0.099b
11	69	61	0.00027=0.034b
21	89	76	0.00042=0.052b
22	92	81	0.00048=0.061b
23	134	120	0.00070=0.081b
24	124	110	0.00058=0.071b
31	129	116	0.00063=0.080b
32	95	85	0.00097=0.120b
33	100	89	0.00106=0.130b
34	81	72	0.00069=0.085b

### 5.3 Porosity Levels

All specimens within one of the four groups listed in Table 3.2 were first visually compared to determine whether porosity levels varied in either the fatigue or the fast fracture region for the specimens in any given group. Three of the groups showed no apparent variation in porosity levels; one specimen was randomly chosen from each of these groups for porosity evaluation. Three of the five specimens from the weld center group showed equivalent porosity levels in both the fatigue and fast fracture regions. A fourth specimen appeared to have a higher amount of porosity in the fatigue region but similar porosity in the fast fracture region to the first three while the fifth specimen from this group contained an unusually large pore in the fast fracture region but had a similar degree of porosity in the fatigue region to the first three specimens. These latter two specimens were chosen from the weld center group for porosity evaluation together with one specimen each from the 4140 HAZ, HTS HAZ N and HTS HAZ F. Results of the porosity counts have been given in Table 5.5.

Table 5.5 Fracture Surface Porosity in the Fatigue and Fast Fracture Regions

<u>Specimen Number</u>	<u>Group</u>	<u>Fatigue Region Porosity (%)</u>	<u>Fast Fracture Region Porosity (%)</u>
3	weld center	4.0	22.5
13	weld center	5.1	6.6
11	HTS HAZ N	2.0	3.2
32	HTS HAZ F	1.5	7.4
23	4140 HAZ	8.8	19.2

#### 5.4 Fatigue Surfaces

Scanning electron microscope (SEM) microphotographs from the air and salt water fatigue surfaces of every weldment region have been included in Figures 5.9 to 5.18. These figures illustrate the various fracture morphologies owing to cracking during salt water and air fatigue and serve to relate the crack growth rate data presented in Figures 5.1 to 5.8 to the occurrence of environmentally-assisted cracking.

Four microphotographs from the HTS HAZ N region appear in Figures 5.9 to 5.12; the air and salt water cracking behaviors at low  $\Delta K_{eff}$  levels are shown in Figures 5.9 and 5.10, respectively, and the crack paths for the two environments at intermediate  $\Delta K_{eff}$  levels are represented in Figures 5.11 and 5.12.

The fracture morphology of the HTS HAZ F is shown in Figure 5.13 for the air environment and in Figure 5.14 for the salt water environment. Two photomicrographs were included from the weld center region as well; the fatigue surfaces in air and in salt water for this region are shown in Figures 5.15 and 5.16, respectively.

Four microphotographs from the fatigue surfaces of the 4140 HAZ appear in Figures 5.17 to 5.18. These represent the air and salt water environment fracture behaviors of this region at low magnifications.

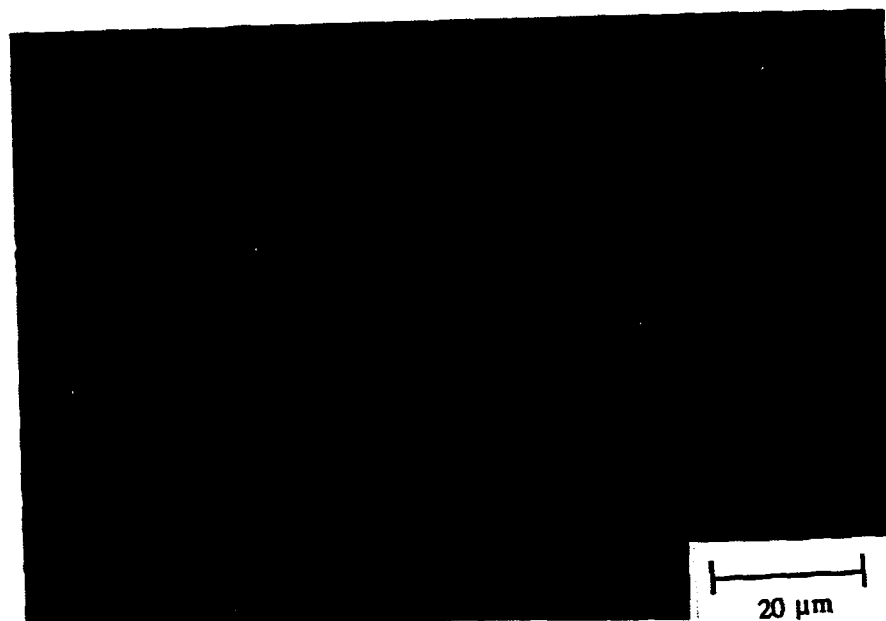


Figure 5.9: Fatigue Surface of the HTS HAZ N in Air at Low Cyclic Stress Intensity.



Figure 5.10: Fatigue Surface of the HTS HAZ N in Salt Water at Low Cyclic Stress Intensity.

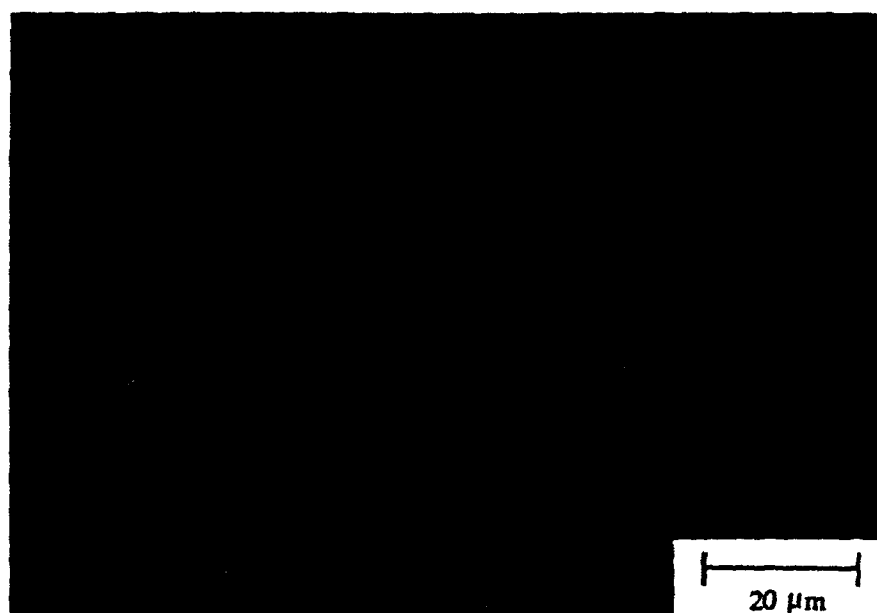


Figure 5.11: Fatigue Surface of the HTS HAZ N in Air at Intermediate Cyclic Stress Intensity.

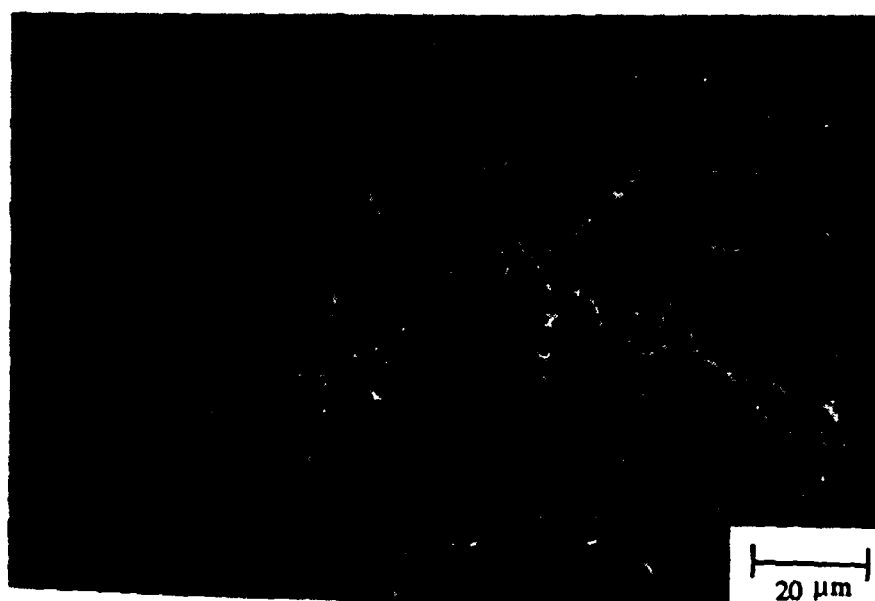


Figure 5.12: Fatigue Surface of the HTS HAZ N in Salt Water at Intermediate Cyclic Stress Intensity.

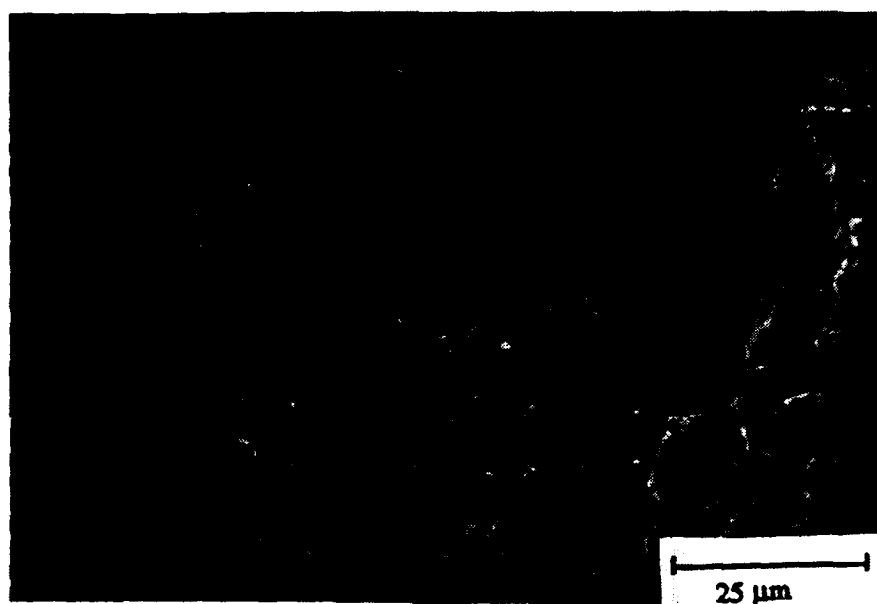


Figure 5.13: Fatigue Surface of the HTS HAZ F in Air.

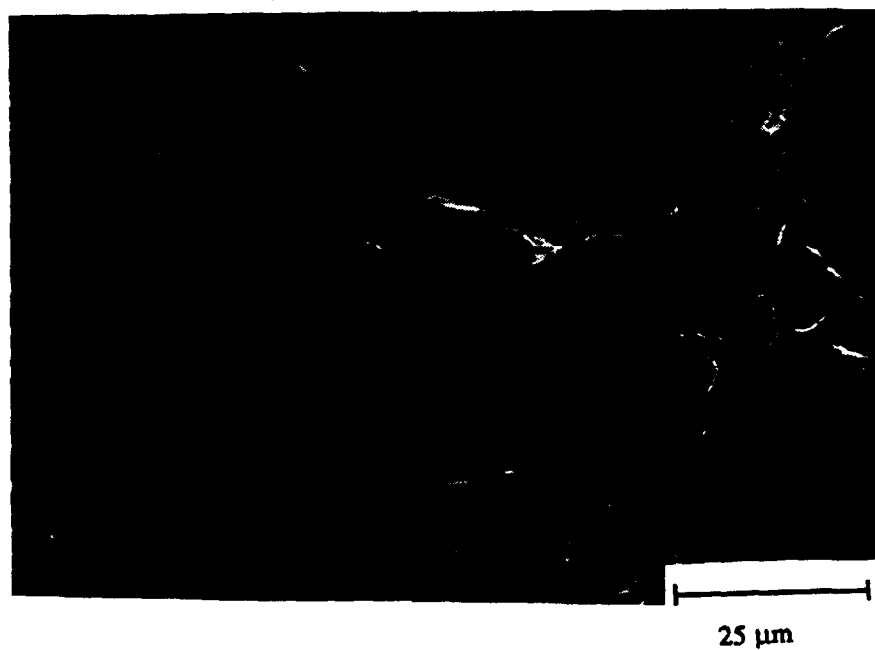


Figure 5.14: Fatigue Surface of the HTS HAZ F in Salt Water.

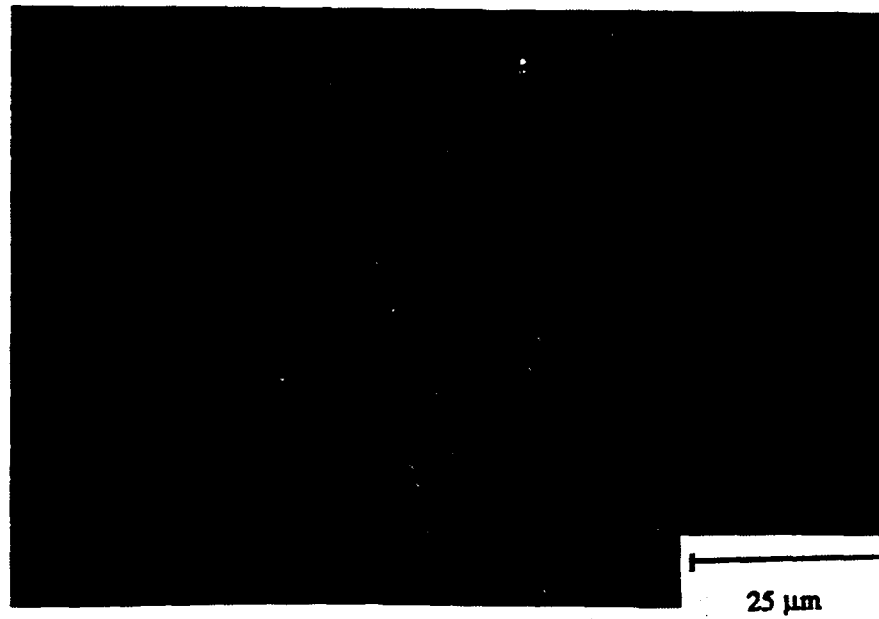


Figure 5.15: Fatigue Surface of the Weld Center in Air.



Figure 5.16: Fatigue Surface of the Weld Center in Salt Water.



Figure 5.17: Fatigue Surface of the 4140 HAZ in Air at Low Magnification.



Figure 5.18: Fatigue Surface of the 4140 HAZ in Salt Water at Low Magnification.



## Chapter 6

### DISCUSSION AND CONCLUSIONS

#### 6.1 Corrosion-Fatigue Data

The primary focus of the discussion in this section will be on the crack growth behavior within each of the weldment regions at low, intermediate and high cyclic stress intensities. These three cracking stages are clearly separated by changes in the slopes of the  $da/dN$  vs.  $\Delta K_{eff}$  salt water data for the HTS HAZ F and 4140 HAZ regions as seen in Figures 5.1 and 5.4. In general, these stages in salt water include an initial cracking behavior at low values of  $\Delta K_{eff}$  that is highly sensitive to the  $\Delta K_{eff}$  level, a second stage that is flagged by the appearance of a "kink" in the  $da/dN$  vs.  $\Delta K_{eff}$  curve for which the dependence on  $\Delta K_{eff}$  lessens in sensitivity, and finally a reoccurrence of the steeply-sloped cracking behavior at high  $\Delta K_{eff}$  levels.

The behavior of the data differs from one weldment region to another which may be due to the variation in microstructures within these regions. General trends in the data will be discussed with reference to the effects of porosity, frequency, microstructure and salt water on cracking behavior, and cases of exceptions will be addressed. A model of the rate-controlling process will be offered as an explanation of the observed behavior.

##### 6.1.1 Low $\Delta K_{eff}$ Behavior

Inspection of the data in Figures 5.1 to 5.4 at crack growth rates indicates that a different behavior occurs for tests at 1 Hertz in salt water as compared to all other tests. There is an initial high dependence on  $\Delta K_{eff}$  for tests in salt water at 1 Hertz as well as a crack initiation delay for these experiments. The mechanism of initiation delay appears to be due to salt water effects; it is present for data from tests in salt water at 5 Hertz but the delay is more pronounced at 1 Hertz in this environment. A blunting mechanism would explain this behavior; cracking in salt water may have been arrested due to blunting by

pitting or by an increased sensitivity in salt water to a crack-arresting mechanism resulting from porosity. The behavior of the data favors the metal dissolution mechanism of blunting by pitting; more time is allowed for pits to develop at 1 Hertz than at 5 Hertz which explains the enhanced retardation effect at 1 Hertz. At low crack growth rates and low cyclic frequencies more time is allowed for the growth of a film of corrosion products on the crack surface; the presence of this film can also retard crack growth rates.

Comparison of the data in Figures 5.1 to 5.4 at low  $\Delta K_{eff}$  levels shows a higher dependence of the crack growth rates in salt water at 1 Hertz on  $\Delta K_{eff}$  than of the crack growth rates in air at that frequency, clearly the rate-controlling mechanism in salt water is dependent itself upon  $\Delta K_{eff}$ . At five Hertz, the crack growth rates in air and in salt water show an equivalent amount of sensitivity to the  $\Delta K_{eff}$  value. Although the salt water cracking rates at 1 Hertz were initially lower than those at five Hertz for the HTS HAZ F, weld center and 4140 HAZ regions, they eventually overtake the growth rates at 5 Hertz indicating that the rate-controlling mechanism is enhanced at the lower cyclic frequency if in fact the same mechanism controls the rate of cracking at both frequencies.

The effect of porosity on the cracking behavior at low  $\Delta K_{eff}$  levels may be that of an increased sensitivity to a crack arresting mechanism in salt water as compared to in air, however since the arresting behavior is more pronounced at 1 Hertz than at 5 Hertz, it is more readily explained by a blunting mechanism that is unique to the corrosion process, pitting, or by the growth of a corrosion-product film layer which would be favored at a lower frequency. The highest measured porosity level recorded in Table 5.5 was found in the 4140 HAZ region which also had the least pronounced frequency effect in the retardation mechanism. This evidence would seem to rule out any porosity effect at low  $\Delta K_{eff}$  levels.

### 6.1.2 Transition Stage Crack Growth Behavior

The  $da/dN$  vs.  $\Delta K_{eff}$  data from tests in Figures 5.1 to 5.8 include a transition stage at intermediate cyclic stress intensity levels for some regions which represents a second stage of cracking in these regions and is especially pronounced in Figures 5.1 and 5.4 for the HTS HAZ F and 4140 HAZ regions. Characterized by a "kink" in the  $da/dN$  vs.  $\Delta K_{eff}$  curve, the onset of this stage may be linked with the growth of the cyclic plastic zone to that of the average grain size within the metal at which point the crack is opened to its environment and Mode I cracking ensues [22].

The  $\Delta K_{eff}$  values at which the transition stage was observed to occur for a given run are reported in Table 5.2. In the HTS HAZ F region this transition was seen for the tests in salt water at 1 Hertz and 5 Hertz, but the tests in air do not adequately cover the intermediate  $\Delta K_{eff}$  values and it can not be determined whether the transition occurred in air. The transition stage is seen for the data in air at 5 Hertz within the 4140 HAZ, in addition to the data at both frequencies in salt water. A frequency effect is noted for the onset of this stage in salt water, wherein the transition is observed to occur at lower growth rates and lower cyclic stress intensities for the salt water data at the higher frequency of 5 Hertz in both weldment regions, and crack growth rates are much enhanced at 1 Hertz during this cracking stage.

In both the HTS HAZ F and 4140 HAZ regions, for which this transition stage is well pronounced, the data was fitted to the growth law using only the data from within the transition stage for those runs in which it was shown to occur; these are marked by a boldface 'T'. In the HTS HAZ F region, the growth law constants reflect the sharp contrast in cracking behavior during this stage as compared to crack growth behavior outside of the transition stage for tests in air and in salt water. The growth law constants for the set of data from a salt water test outside the transition stage show the manner in which the runs in salt water return to the initial steep dependence on  $\Delta K_{eff}$  and resemble the runs in air at high  $\Delta K_{eff}$  values. The growth law constants for the 4140 HAZ also reveal a

change during this transition stage in the cracking behavior of the tests which is more pronounced for the data at 1 Hertz than at 5 Hertz in salt water. In Figure 5.4 the crack growth rates for the test in salt water at 1 Hertz at the onset of its transition are six times that of the tests in air and in salt water at 5 Hertz, this represents the highest level of accelerated crack growth found in this study.

### 6.1.3 High $\Delta K_{eff}$ Behavior

The data in all four weldment regions show that at very high  $\Delta K_{eff}$  values the growth rates for the tests in air and in salt water approach one another as mechanical fatigue begins to occur at a rate that is faster than any of the other processes involved, and the salt water cracking behavior resembles that of the behavior in air for this stage of unstable crack extension, regardless of frequency.

In the HTS HAZ F and 4140 HAZ regions the beginning of stage three is characterized by a return to the steep dependence of the crack growth rate on the cyclic stress intensity level. In both of these regions the crack is seen to be growing at a faster rate for tests in salt water at 1 Hertz than for tests at 5 Hertz as instability is approached; however, the  $\Delta K_{eff}$  values at the onset of stage three as reported in Table 5.2 were not found to depend on frequency. Because this final stage begins at comparable cyclic stress intensity values regardless of the cracking rate, environment, or frequency, the explanation for this phenomenon must be that it occurs as the maximum stress intensity level approaches the fracture toughness.

There is no evidence that the salt water environment lessened the load-carrying capability of these regions at instability. The time to failure during salt water exposure was altered, and the extent of this effect was enhanced at the lower frequency. For the 4140 HAZ, the presence of salt water at five Hertz had no great effect on the total life of the material; the crack spent a longer time in the first cracking stage as described for the low  $\Delta K_{eff}$  values, but the point of instability did not occur at an increased crack growth rate. At

one Hertz in the same region, the crack growth rate was decidedly enhanced prior to the point of instability and the life was significantly reduced at intermediate and high  $\Delta K_{eff}$  values because of the salt water environment. A salt water environment in the HTS HAZ F region seems to have had the same effect of enhanced growth rates near instability for the tests in salt water at the lower frequency compared to those of the salt water data at 5 Hertz as well as the data in air.

#### 6.1.4 Relative Cracking Rates of the Weldment Regions

The data presented in Figures 5.5 to 5.8 offer insight into the relative cracking behavior of the four regions tested for the conditions of salt water and air environments at both 1 and 5 Hertz. Figures 5.5 and 5.6 contain the crack growth data for all tests at 1 Hertz in salt water and in air, respectively. No data were available for the HTS HAZ N region in salt water at this frequency, but in air this region showed the highest growth rates of all four regions as seen from the data in Figure 5.6. In salt water at 1 Hertz the crack growth rates in the HTS HAZ F region surpass all others reported due to environmentally-assisted cracking in this region. As the data in Figures 5.7 and 5.8 show, the crack growth rates in the HTS HAZ N region in salt water at 5 Hertz greatly surpass the other regions in salt water at this frequency even though the results in air at this frequency show similar crack growth rates for the HTS HAZ N, weld center and HTS HAZ F regions. If the general trends are to be extended then it would be expected that the salt water data from the HTS HAZ N region at 1 Hertz would exceed those of the HTS HAZ F region in Figure 5.5.

Although the crack growth rates for the HTS HAZ N data in salt water at 5 Hertz were found to be even higher than the those of the other regions in salt water at a lower frequency, this region was not found to be the most susceptible to enhanced cracking due to the salt water environment. The greatest enhancement of crack growth rates was found

for the 4140 HAZ and HTS HAZ F regions; rates accelerated by a factor of six times those in air were found for the data in salt water at 1 Hertz.

Least susceptible to environmentally-enhanced crack growth rates in the presence of salt water was the weld center region for which growth rates in air actually exceeded those found in salt water for a large range of  $\Delta K_{eff}$  values. The reason for this behavior was not fully determined but may be attributed in part to the nature of the stress state within the weld center region. Although this laser welding operation produces a minimal amount of residual stress as compared to other types of welding procedures, there may be some accelerated crack growth effect in air associated with whatever residual stress state may have been present. The porosity level within the fatigue surface of the weld center region was found to be 5% which may have contributed to the relative air and salt water crack growth rates by providing a blunting mechanism in salt water or by interfering with the hydrogen diffusion and embrittlement processes in salt water.

#### 6.1.5 Modelling the Rate-Controlling Mechanisms

The results in Figures 5.1 and 5.4 for the HTS HAZ F and 4140 HAZ regions show accelerated crack growth rates for the salt water experiments, especially at 1 Hertz, over the rates in air at intermediate and high  $\Delta K_{eff}$  levels. Growth rates at low  $\Delta K_{eff}$  values in salt water generally fell below those in air, while at very high  $\Delta K_{eff}$  levels, the two environments resulted in the same cracking rates near instability. These data suggest that one mechanism cannot control the rate of crack growth throughout the range of conditions encountered during corrosion-fatigue; although the mechanisms may proceed at non-constant rates, that alone does not explain the transition regions in the  $da/dN$  vs.  $\Delta K_{eff}$  data. A general model for the rate-controlling mechanisms during corrosion-fatigue that makes use of the changes in the rates of the individual mechanisms is discussed in this section.

It is reasonable to assume that many mechanisms of crack extension do occur during corrosion-fatigue, but that a single mechanism controls the cracking process for all possible conditions is not a reasonable assumption. Some mechanisms occur at non-constant rates; the rate of cracking owing to mechanical fatigue depends on the cyclic stress intensity level and increases throughout the test, and other mechanisms depend upon the environmental conditions which may not be constant. In the case of mechanical fatigue, the data indicate that near instability, mechanical fatigue must occur at a rate that surpasses all other cracking rates as it then takes over control of the cracking process. Prior to this point, the increased growth rates seen from data in salt water at 1 Hertz represent enhanced cracking as controlled by some mechanism whose rate exceeds that of mechanical fatigue. In order for mechanical fatigue to take over control in the rate of the cracking process, it must be considered to be a parallel mechanism along with the other rate-controlling mechanisms that are responsible for enhanced crack growth rates; in this way the fastest rate is allowed to prevail. That mechanical fatigue and hydrogen embrittlement are considered parallel mechanisms makes sense because the two are not dependent on one another to proceed.

The low  $\Delta K_{eff}$  behavior requires a different treatment. In this case, some mechanism controls the cracking rate to the extent that it can slow cracking down below the rate of mechanical fatigue as evidenced by lower cracking rates in salt water than in air at low  $\Delta K_{eff}$  levels. Blunting mechanisms will explain this behavior if one considers an incremental crack extension by mechanical fatigue that exposes fresh bare metal to its environment. This metal is then subjected to the formation of a pit by dissolution, the pit then relieves the stress intensity at the crack tip and slows down the overall crack growth rate. The mechanisms of mechanical fatigue and pitting follow one another sequentially.

In Chapter 2 the resistance to crack extension offered by a system in response to a crack growth mechanism was given as the inverse of the growth rate associated with the mechanism. Therefore, parallel resistors can be used to model the resistances of a system

to parallel cracking mechanisms and resistors in series can model the resistances to cracking by sequential mechanisms. A possible model to account for the behavior seen in these results is sketched in Figure 6.1; the resistances of the system to cracking due to the mechanisms of mechanical fatigue, hydrogen embrittlement and dissolution have been included.

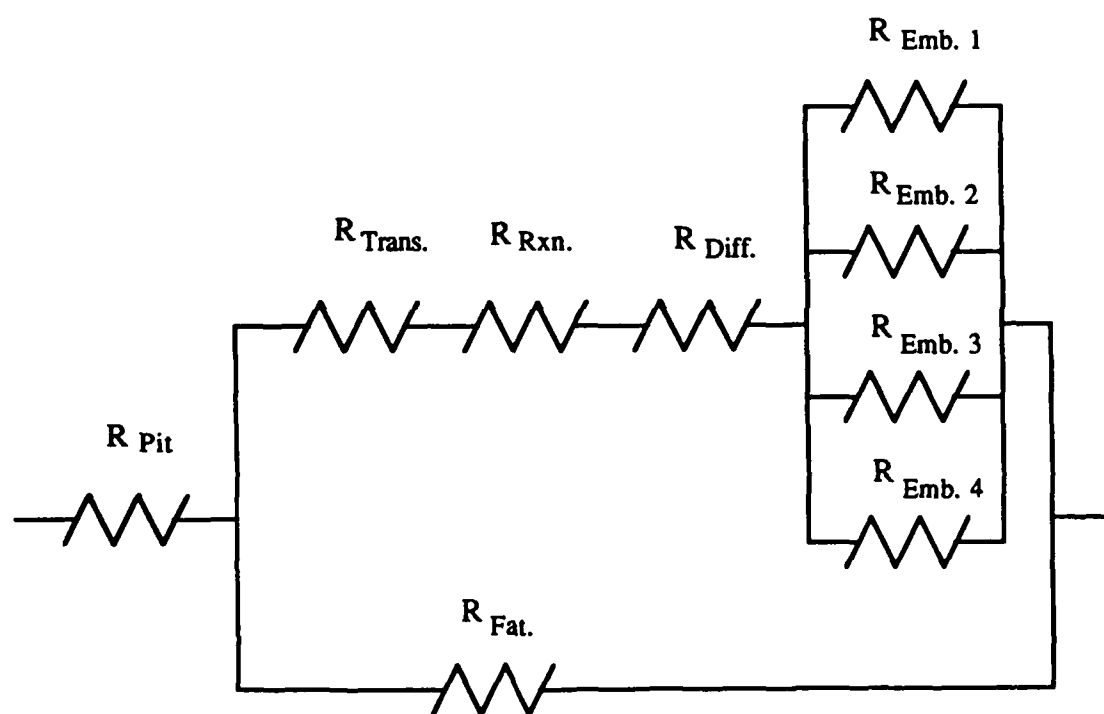


Figure 6.1: A Proposed Model for the Rate-Controlling Mechanisms During Corrosion-Fatigue.



Each 'R' represents a resistance to a cracking mechanism such that:

$$R_m = \frac{1}{\left(\frac{da}{dN}\right)_m} \quad (6.1)$$

and the subscripts attached to each resistance denote the following mechanisms represented in this model:

"Emb. 1" to "Emb. 4" are individual parallel embrittlement mechanisms associated with hydrogen once it has diffused to the embrittlement site.

"Diff." is the mechanism of hydrogen diffusion through the plastic zone.

"Rxn." represents the reactions at the metal/environment interface by which hydrogen is adsorbed.

"Trans." is the mechanism of hydrogen transport through the electrolyte to the crack tip.

"Fat." is the mechanism of mechanical fatigue.

"Pit." is the mechanism of pitting by metal dissolution.

## 6.2 Fracture Toughness Results

The results in Table 5.4 show that the cyclic plastic zone size never grew to a size that approached that of the specimen thickness for any test conditions and therefore the specimens remained in plane strain conditions at the time of failure. The measured values reported for the fracture toughnesses represent the plane-strain fracture toughness values of the material in all regions.

The 4140 HAZ had the highest fracture toughness value of any region. This region also had the highest strength as reported in Table 5.3 and the highest accelerated crack

growth rates owing to salt water. Fracture toughness values were found to be high for the weld center region, which was also found to be a high-strength region, yet no accelerated crack growth rates were found in the salt water data for this region. The microstructures within the 4140 HAZ, weld center and HTS HAZ N regions were reported in Chapter 3 to all contain martensite, while the responses of these three regions to corrosion-fatigue included accelerated crack growth in the 4140 HAZ, no change in cracking behavior for the HTS HAZ N and increased resistance to crack growth in the weld center. The salt water cracking behavior of these regions seems to be as much a result of the unique solidification procedure that produced these microstructures as the microstructures themselves.

The salt water did not seem to affect the load-carrying capabilities of any of the weldment regions; fracture toughness values were found to be comparable for all air and salt water tests within a region. This observation could be predicted from the proposed rate-controlling model because it holds mechanical fatigue responsible for the crack growth rate prior to failure.

Specimen #3 from the weld center region contained a large porosity level in its fast fracture region which was not the case for the other specimens from this region; one can not conclude from the results in Table 5.4 whether this porosity affected the fracture toughness value for the weld center region. The weld center region was the only one of the four that showed any variation in its porosity levels from specimen to specimen. It would therefore not be possible to attribute any variation in the fracture toughness values found in the other regions to porosity.

### 6.3 Fatigue Surfaces Analysis

An extensive amount of scanning electron microscope (SEM) analysis of the fractured specimens revealed unique characteristics of the cracking behaviors for several of the corrosion-fatigue test conditions in this study that relate to the results of the  $da/dN$  vs.  $\Delta K_{eff}$  data. This section will address the fracture surfaces of each region individually.

### 6.3.1 The HTS HAZ N

Figures 5.9 to 5.12 contain SEM photomicrographs from specimens tested in the HTS HAZ N region. The morphology in Figure 5.9 includes evenly spaced striations on a smooth fracture surface resulting from fatigue in air. This fracture surface indicates that cracking occurred by the continuous advance of a primary crack through the microstructure. The morphology in the center of Figure 5.10, a photomicrograph taken from a specimen that had undergone fatigue in salt water, resembles that of Figure 5.9 in that ductile striations are seen to have occurred during the fracture process in salt water. In addition to the advance of this primary fatigue crack, the fracture surface of Figure 5.10 shows that secondary cracking has occurred as evidenced by the brittle failure surrounding the central morphology of the primary crack in the figure. There is some evidence of salt water attack in Figure 5.10; in the lower left corner some intergranular fracture can be seen indicating that environmentally assisted cracking has occurred. These two photomicrographs were taken from low to intermediate  $\Delta K_{eff}$  levels where the low energy intergranular fracture in Figure 5.10 served to assist cracking in the salt water specimen.

Figures 5.11 and 5.12 were taken from specimens tested in air and in salt water, respectively, from the HTS HAZ N, and again illustrate similar morphologies for the air and salt water fractures in this region; the environmental effect is manifested as secondary cracking and some cleavage facets in Figure 5.12. These photomicrographs are quite similar despite their different test conditions, as was found to be the case for Figures 5.9 and 5.10. Figures 5.9 to 5.12 support the results of the fatigue crack growth behavior in this region reported in Figure 5.2; little evidence of salt water attack was found on the salt water fatigue surfaces, and crack growth rates were not greatly accelerated due to salt water for this region.

### 6.3.2 The HTS HAZ F

Two distinctly different morphologies from tests in air and in salt water were found in the HTS HAZ F region and are shown in Figures 5.13 and 5.14, respectively. Figure 5.13 reveals a very ductile, striated fracture in air that is quite contrasted from the morphology of Figure 5.14; the salt water attack on this region is quite clear as evidenced by the intergranular fracture in Figure 5.14. HTS HAZ F cracking in salt water was greatly assisted by the low energy, intergranular failure which was quite possibly accelerated by trapping of hydrogen at MnS inclusions [24]. Figure 5.14 contains evidence of this phenomenon; voids, such as the one in the lower left corner of Figure 5.14, surrounded by intergranular failure, may indicate the former site of an MnS inclusion. This particular void size is on the order of the inclusion size in Figure 3.6. These photomicrographs come from regions of low  $\Delta K_{eff}$ , at intermediate  $\Delta K_{eff}$  levels there still was evidence of intergranular fracture and also a large number of secondary cracks. These figures illustrate the reason for the highly accelerated crack growth rates seen at 1 Hertz in the salt water data for this region: intergranular cracking in the salt water environment contributed to greatly enhanced crack growth rates.

### 6.3.3 The Weld Center

The fatigue surface of the weld center region in air is shown in Figure 5.15 to exhibit a ductile transgranular failure mode. The salt water fatigue surface morphology of the weld center region contains the most unique characteristics of all regions and conditions in this study. This surface is seen in Figure 5.16 to obviously differ from that of the air environment; grain boundaries on the order of  $10\ \mu\text{m}$  appear to be outlined in the center of Figure 5.16 as a result of a decohesion fracture process. Although cracking was obviously affected by the presence of salt water, the crack growth rates in the weld center region were actually higher for the air environment. The weld center cracking process in air resulted in

a flat fracture surface while the topography of the salt water fracture is more jagged. The nature of the salt water failure suggests that competitive mechanisms such as residual stress, porosity and embrittlement had the combined effect in this refined microstructure of tending to orient the crack in a number of different ways, hence it expended a lot of energy in trying to locate the local low energy path.

#### 6.3.4 The 4140 HAZ

The fracture morphologies of the 4140 HAZ are shown in Figure 5.17 for the air environment and Figure 5.18 for the salt water environment. Although the morphologies for these two different conditions do differ from one another, there is no strong evidence of salt water attack on the salt water fatigue surfaces as was the case for the HTS HAZ F. The region of Figure 5.17 failed by ductile tearing as evidenced by the plastic flow while the fatigue surface of Figure 5.18 shows a more embrittled failure; both are transgranular, the salt water fatigue surface contains areas of faceted grain failure.

#### 6.4 Conclusions

The highest fatigue crack growth rates were found in the martensitic HTS HAZ N region in salt water. Although the HTS HAZ N did have the fastest overall crack growth rates for the salt water data, those growth rates in salt water were not highly accelerated over the growth rates for the region in air. This region was found to be not heavily affected by salt water corrosion-fatigue; no evidence of intergranular cracking was found on the fatigue surfaces for this region. The primary fatigue crack was assisted by a secondary cracking mode in the salt water environment.

Both the HTS HAZ F and 4140 HAZ regions were found to exhibit highly accelerated crack growth rates due to environmentally-assisted cracking in salt water; crack growth rates as much as six times those in air were found for salt water data at 1 Hertz in both of these regions. The hydrogen attack contributing to the increased growth rates is

evidently intergranular cracking in the fatigue surface morphology of the HTS HAZ F region in Figure 5.14, and embrittlement evidence appears as an increased incidence of faceting for the 4140 HAZ.

The weld center region was found to be the most resistant to environmentally-assisted cracking; salt water rates in this region fell below those in air. The high energy salt water cracking behavior in this region was seemingly a result of competitive mechanisms acting on a localized scale to misorient the crack.

Salt water had no effect on the load-carrying capabilities of the regions. The plane strain fracture toughness values of the four regions were found using data from the air and salt water specimens. The 4140 HAZ was found to be the toughest region, followed by the weld center; the fracture toughnesses found for these regions were  $129 \text{ MPa } \sqrt{\text{m}}$  and  $107 \text{ MPa } \sqrt{\text{m}}$ , respectively. The fracture toughness values found for the HTS heat-affected zones were  $83 \text{ MPa } \sqrt{\text{m}}$  near the fusion zone and  $92 \text{ MPa } \sqrt{\text{m}}$  near the base metal.

Various mechanisms become responsible for the overall crack growth rates during different stages of corrosion-fatigue. The shapes of the  $da/dN$  vs.  $\Delta K_{\text{eff}}$  data provide evidence of the changing rate-controlling mechanisms. The individual cracking mechanisms proceed at non-constant rates during corrosion-fatigue owing to their dependences on such non-constant parameters as the cyclic plastic zone size.

## REFERENCES

- (1) Denney, P. E. and Nurminen, J. I., " Program to Demonstrate the Welding of Naval Catapult Trough Covers to Tracks Using a High Power Laser Beam," Westinghouse Report 87-9D4-RAIL-R1, Pittsburgh, Pa., May, 1987.
- (2) Grigor'yants, A. G., et al., *Automatic Welding*, English Translation of *Avtomaticheskaya Svarka*, No. 10, 1980, pp. 9-12.
- (3) Denney, P. E., and Metzbower, E. A., *International Conference on Technology and Applications of HSLA Steels*, Philadelphia, Pa., 1983, pp. 689-696.
- (4) Metzbower, E. A., Denney, P. E., Fraser, F. W. and Moon, D. W., *Welding Journal*, Vol. 63, No. 7, July, 1984, pp. 39-43.
- (5) Metzbower, E. A., *ICALEO 1982*, Vol. 31, 1982, pp. 20-23.
- (6) Metzbower, E. A. and Moon, D. W., *Fractography and Materials Science*, Williamsburg, Va., Nov. 27-28, 1979, pp. 131-149.
- (7) Alekseev, V. A., *Welding Production*, English Translation of *Svarochnoe Proizvodstvo*, No. 11, 1981, pp. 15-17.
- (8) Toshchev, A. M., Tochilkin, V. A., Truseneva, G. P., Vasyanova, T. I. and Belen'kii, A. M., *Welding Production*, English Translation of *Svarochnoe Proizvodstvo*, No. 1, 1982, pp. 19-20.
- (9) Strychor, R., Moon, D. W. and Metzbower, E. A., *Journal of Metals*, Vol. 36, No. 5, May, 1984, pp. 59-61.
- (10) Moltan, P. A., *Journal of Materials Science Letters* 4, 1985, pp. 281-283.
- (11) Denney, P. E. and Metzbower, E. A., *ICALEO 83*, Vol. 38, 1983, pp. 80-86.
- (12) Fontana, M. G., *Corrosion Engineering*, New York, McGraw-Hill, 1986.
- (13) Scott, P. M. in *Corrosion Fatigue, ASTM STP 801*, American Society for Testing and Materials, 1983, pp. 319-344.
- (14) Congleton, J., Craig, I. H., Olieh, R. A. and Parkins, R. N. in *Corrosion Fatigue, ASTM STP 801*, American Society for Testing and Materials, 1983, pp. 367-389.
- (15) Kitagawa, H., Tsuji, K., Hisada, T. and Hashimoto, Y. in *Corrosion Fatigue, ASTM STP 801*, American Society for Testing and Materials, 1983, pp. 147-158.
- (16) Leis, B. N., Rungta, R., Mayfield, M. E. and Beavers, J. A. in *Corrosion Fatigue, ASTM STP 801*, American Society for Testing and Materials, 1983, pp. 197-228.
- (17) Ricci, R. H., Berardo, L. N., Gassa, L. M. and Vilche, J. R., *International Congress on Metallic Corrosion*, Vol. 3, Toronto, June 3-7, 1984, pp. 161-166.

- (18) Endo, K., Komai, K., Shikida, T. in *Corrosion Fatigue, ASTM STP 801*, American Society for Testing and Materials, 1983, pp. 81-95.
- (19) Cowling, M. J. and Appleton, R. J. in *Proceedings, Fatigue and Crack Growth in Offshore Structures*, The Institution of Mechanical Engineers, London, 1986, pp.77-92.
- (20) Wei, R. P. and Shim, G. in *Corrosion Fatigue, ASTM STP 801*, American Society for Testing and Materials, 1983, pp. 5-18.
- (21) Liaw, P.K., Leax, T.R., Fabis, T. R. and Donald, J. K., *Engineering Fracture Mechanics*, Vol. 26, No. 1, 1987, pp. 1-13.
- (22) Barbangelo, A., *Journal of Engineering Materials and Technology, Transactions of the ASME*, Vol. 109, No. 2, April, 1987, pp. 119-123.
- (23) Matlock, D. K., Edwards, G. R., Olson, D. L. and Ibarra, S., *Journal of Materials Engineering*, Vol. 9, No. 1, 1987, pp. 23-34.
- (24) Torronen, K. and Kemppainen, M. in *Corrosion Fatigue, ASTM STP 801*, American Society for Testing and Materials, 1983, pp. 287-318.
- (25) Fujii, C. T. and Smith, J. A. in *Corrosion Fatigue, ASTM STP 801*, American Society for Testing and Materials, 1983, pp. 390-402.
- (26) Hodgkiess, T. and Cannon, M. J. in *Proceedings, Fatigue and Crack Growth in Offshore Structures*, The Institution of Mechanical Engineers, London, 1986, pp. 69-76.
- (27) Ford, P., "Mechanistic Understanding of Stress Corrosion and Corrosion Fatigue, and its Practical Use," in a seminar given at The Pennsylvania State University, October 26, 1987.
- (28) Turnbull, A. in *Corrosion Fatigue, ASTM STP 801*, American Society for Testing and Materials, 1983, pp. 351-364.
- (29) Hertzberg, R. W., *Deformation and Fracture Mechanics of Engineering Materials*, John Wiley and Sons, New York, 1983.
- (30) Nelson, H. G., "Hydrogen-Materials Incompatibility: Present Understanding and Future Research Opportunities," in a seminar given at The Pennsylvania State University, November 18, 1987.
- (31) Gerberich, W. W. in *Corrosion Fatigue, ASTM STP 801*, American Society for Testing and Materials, 1983, pp. 19-25.
- (32) Schijve, J. in Ewalds, H. L. and Wanhill, R. J. H., *Fracture Mechanics*, Edward Arnold, London, 1984, p. 179.
- (33) Murakami, R. and Ferguson, W. G., *Fatigue and Fracture of Engineering Materials and Structures*, Vol. 9, No. 6, 1987, pp. 477-488.



- (34) Davis, D. A. and Czyryca, E. J. in *Corrosion Fatigue*, ASTM STP 801, American Society for Testing and Materials, 1983, pp. 175-196.
- (35) Ross, R. P., *Metallic Materials Specification Handbook*, E. & F. N. Spon, New York, 1980.
- (36) Denney, P., personal correspondence, October, 1986.
- (37) Reed, E. L., *Photomicrographs of Iron and Steel*, John Wiley & Sons, New York, 1929.
- (38) Queeney, R. A., personal consultation, May, 1986.
- (39) Ewalds, H. L. and Wanhill, R. J. H., *Fracture Mechanics*, Edward Arnold, London, 1984.
- (40) Yuzawich, P. M. and Hughes, C. W., "An Improved Technique for Removal of Oxide Scale from Fractured Surfaces of Ferrous Materials," Westinghouse Scientific Paper 77-1D9-FRTOG-P1, Pittsburgh, Pa., March, 1977.
- (41) DeHoff, R. T. and Rhines, F. N., *Quantitative Microscopy*, McGraw-Hill, New York, 1968.

## APPENDIX A

## COMPLETE CRACK LENGTH VERSUS NUMBER OF CYCLES DATA

SPECIMEN #1	RUN #1	<u>Cycles</u>	<u>Crack Length (cm)</u>
		27330	1.9177
		27595	1.9304
		27850	1.9431
		28280	1.9685
		28430	1.9812
		28580	1.9939
		28660	2.0193
		28780	2.0701
		28900	2.1717
		29020	2.2733
		29139	2.3241

SPECIMEN #3	RUN #4	<u>Cycles</u>	<u>Crack Length (cm)</u>
		1600	1.4785
		4100	1.5085
		5900	1.5385
		7400	1.5682
		9160	1.5982
		10460	1.6281
		11100	1.6581
		11870	1.6881

SPECIMEN #3	RUN #7	<u>Cycles</u>	<u>Crack Length (cm)</u>
		28460	1.7450
		32050	1.7730
		35230	1.8148
		38330	1.8478
		39930	1.8834
		41285	1.9228
		42460	1.9558
		43485	1.9926
		44210	2.0307
		44665	2.0676
		45015	2.1031
		45565	2.1361
		46220	2.1717
		46700	2.2060

**SPECIMEN #3 RUN #8**

<u>Cycles</u>	<u>Crack Length (cm)</u>
11700	2.4336
11889	2.4643
12009	2.4948
12087	2.5255
12117	2.5563
12134	2.5867
12204	2.6175
12261	2.6482
12283	2.6787
12300	2.7094
12330	2.7399
12337	2.7706
12353	2.8014
12377	2.8318
12411	2.8626

**SPECIMEN #11 RUN #2**

<u>Cycles</u>	<u>Crack Length (cm)</u>
29420	1.7005
30030	1.7282
30650	1.7556
31120	1.7833
31655	1.8110
32060	1.8384
32430	1.8661
32750	1.8936
33065	1.9212
33360	1.9489

**SPECIMEN #11 RUN #4**

<u>Cycles</u>	<u>Crack Length (cm)</u>
15610	2.0041
17200	2.0318
19050	2.0592
24725	2.0869
26290	2.1143
27500	2.1420
28600	2.1697
29850	2.2248

**SPECIMEN #11 RUN #5**

<u>Cycles</u>	<u>Crack Length (cm)</u>
21420	2.7254
21640	2.7528
21820	2.7803
21965	2.8077
22090	2.8623
22125	2.8898
22150	2.9172
22200	2.9446
22230	2.9720

**SPECIMEN #12 RUN #2**CyclesCrack Length (cm)

2040	1.5837
2835	1.6182
3934	1.9627
3979	1.9972
4045	2.0315
4296	2.0660
4361	2.1006
4441	2.1349
4819	2.1694
4860	2.2037
4920	2.2382
5917	2.6198

**SPECIMEN #21 RUN #5**CyclesCrack Length (cm)

1221	2.0803
1246	2.1311
1275	2.1565
1332	2.1819
1392	2.4867

**SPECIMEN #23 RUN #4**CyclesCrack Length (cm)

3223	1.6459
3727	1.6728
4240	1.7005
4700	1.7285
5024	1.7564

**SPECIMEN #23 RUN #6**CyclesCrack Length (cm)

1657	1.7846
3133	1.8125
4251	1.8405
5031	1.8687
5833	1.8966
6610	1.9246
7333	1.9528
7953	1.9807

**SPECIMEN #23 RUN #8**CyclesCrack Length (cm)

2810	2.0086
4284	2.0366
5514	2.0648
6585	2.0927
7630	2.1206
8685	2.1488
9693	2.1768

**SPECIMEN #23 RUN #9**

<u>Cycles</u>	<u>Crack Length (cm)</u>
10741	2.7318
11026	2.7597
11196	2.7879
11226	2.8158
11306	2.8438
11424	2.8720
11536	2.8999
11678	2.9279
11753	2.9560
11830	2.9840
11909	3.0119
12010	3.0399
12064	3.0681
12100	3.1394

**SPECIMEN #24 RUN #2**

<u>Cycles</u>	<u>Crack Length (cm)</u>
49720	1.8199
50270	1.8471
50865	1.8745
51470	1.9017
52080	1.9291
52395	1.9563
52850	1.9837
53230	2.0109
53635	2.0384
54030	2.0655
54500	2.0930
54730	2.1201
55100	2.1476
55350	2.1748
55565	2.2022
55835	2.2294
56000	2.2568
56215	2.2840
56425	2.3114
56545	2.3386
58275	2.9096

**SPECIMEN #31 RUN #2**

<u>Cycles</u>	<u>Crack Length (cm)</u>
3510	1.5342
3963	1.5626
4190	1.5908
4850	1.7612
5780	2.6606

**SPECIMEN #32 RUN #7**

<u>Cycles</u>	<u>Crack Length (cm)</u>
2135	1.7247
2985	1.7526
4045	1.7808
4585	1.8087
5430	1.8367
6588	1.8649
6706	1.8928
7230	1.9208
7750	1.9489

**SPECIMEN #32 RUN #10**

<u>Cycles</u>	<u>Crack Length (cm)</u>
3345	2.0048
5350	2.0330
6680	2.0610
7975	2.0889
8600	2.1171
9535	2.1450
10500	2.1730
11325	2.2012
12170	2.2291
12575	2.2570

**SPECIMEN #32 RUN #12**

<u>Cycles</u>	<u>Crack Length (cm)</u>
4110	2.7892
4140	2.8171
4262	2.8450
4392	2.8732
4485	2.9012
4519	2.9291
4568	2.9573
4599	2.9853
4611	3.0132
4655	3.0544

**SPECIMEN #33 RUN #2**

<u>Cycles</u>	<u>Crack Length (cm)</u>
4554	1.5110
4590	1.5390
4689	1.5667
4857	1.5946
5349	1.6223
5803	1.6502
6300	1.6779
7071	1.7059
7894	1.7336
8541	1.7615
9245	1.7892
9877	1.8171
10311	1.8448
10827	1.8724
11272	1.9004
14585	2.6441

**SPECIMEN #34 RUN #4**

<u>Cycles</u>	<u>Crack Length (cm)</u>
1148	2.3642
1165	2.3917
1182	2.4194
1199	2.4468
1204	2.4742
1215	2.5016

**SPECIMEN #34 RUN #5**

<u>Cycles</u>	<u>Crack Length (cm)</u>
730	2.5568
979	2.5842
1111	2.6116
1168	2.6393
1200	2.6667
1232	2.6942
1264	2.7216
1292	2.7493
1326	2.7767
1353	2.8042
1370	2.8316
1393	2.8956

## APPENDIX B

COMPLETE  $dA/dN$  VERSUS  $\Delta K_{EFF}$  DATA

SPECIMEN #1	RUN #1	$dA/dN$ (m/cyc)	$\Delta K_{eff}$ (MPa $\sqrt{m}$ )
		2.05E-07	42.71
		4.17E-07	43.04
		6.67E-07	43.55
		1.00E-06	44.06
		1.53E-06	44.41
		2.11E-06	44.94
		2.95E-06	46.03
		4.62E-06	46.92
		7.02E-06	48.33
		1.26E-05	51.71
		2.04E-05	54.51
		3.20E-05	55.93
SPECIMEN #3	RUN #4	$dA/dN$ (m/cyc)	$\Delta K_{eff}$ (MPa $\sqrt{m}$ )
		7.69E-08	29.40
		1.43E-07	29.61
		2.14E-07	30.11
		2.50E-07	30.63
		3.09E-07	31.16
		3.48E-07	31.70
		4.07E-07	32.24
SPECIMEN #3	RUN #7	$dA/dN$ (m/cyc)	$\Delta K_{eff}$ (MPa $\sqrt{m}$ )
		9.26E-08	27.40
		1.36E-07	27.96
		1.67E-07	28.53
		2.00E-07	29.11
		2.35E-07	29.77
		2.80E-07	30.43
		3.33E-07	31.08
		4.07E-07	31.81
		5.40E-07	32.56
		7.81E-07	33.32
		1.11E-06	34.06
		1.25E-06	34.82
		1.62E-06	35.64



## SPECIMEN #3 RUN #8

da/dN (m/cyc) $\Delta K_{eff}$  (MPa  $\sqrt{m}$ )

1.52E-06	35.93
2.88E-06	36.78
3.19E-06	37.07
4.17E-06	37.65
5.62E-06	38.57
7.00E-06	39.52
8.57E-06	40.52
1.04E-05	41.56
1.30E-05	42.64
1.67E-05	43.78
1.91E-05	44.96
2.18E-05	46.20
2.39E-05	47.51
3.17E-05	48.88
4.00E-05	50.31
5.75E-05	51.42

## SPECIMEN #11 RUN #2

da/dN (m/cyc) $\Delta K_{eff}$  (MPa  $\sqrt{m}$ )

4.28E-07	31.90
5.24E-07	32.38
5.94E-07	32.88
6.76E-07	33.38
7.56E-07	33.89
8.28E-07	34.41
9.54E-07	34.94
1.12E-06	35.49

## SPECIMEN #11 RUN #4

da/dN (m/cyc) $\Delta K_{eff}$  (MPa  $\sqrt{m}$ )

6.63E-08	23.76
1.06E-07	24.00
1.25E-07	24.14
1.55E-07	24.35
1.75E-07	24.53
2.04E-07	24.94
2.43E-07	25.35
2.95E-07	25.64
3.42E-07	25.99
3.68E-07	26.27

**SPECIMEN #11 RUN #5**da/dN (m/cyc)      ΔK<sub>eff</sub> (MPa √m)

1.12E-06	33.49
1.78E-06	34.22
2.38E-06	34.97
4.00E-06	36.16
6.09E-06	37.41
7.72E-06	38.29
1.00E-05	39.20
1.18E-05	39.60
1.69E-05	40.16

**SPECIMEN #12 RUN #2**da/dN (m/cyc)      ΔK<sub>eff</sub> (MPa √m)

1.20E-06	39.48
1.36E-06	40.28
1.57E-06	40.57
1.70E-06	41.10
1.90E-06	41.96
2.02E-06	42.30
2.12E-06	42.84
2.50E-06	44.42
4.59E-06	48.86

**SPECIMEN #21 RUN #5**da/dN (m/cyc)      ΔK<sub>eff</sub> (MPa √m)

1.00E-06	32.93
3.03E-06	33.32
7.10E-06	33.80
1.08E-05	34.32
1.73E-05	34.98
1.94E-05	35.41
2.53E-05	36.07
3.76E-05	37.23
4.53E-05	38.06
5.82E-05	39.74
7.82E-05	41.10
8.80E-05	41.95
1.80E-04	43.44

**SPECIMEN #23 RUN #4**

<u>da/dN (m/cyc)</u>	<u><math>\Delta K_{eff}</math> (MPa <math>\sqrt{m}</math>)</u>
3.85E-07	39.40
4.98E-07	39.58
5.27E-07	39.84
5.40E-07	39.98
5.40E-07	40.06
5.87E-07	40.27
6.40E-07	40.49
6.70E-07	40.59
6.95E-07	40.71
7.54E-07	40.94
8.41E-07	41.22
8.80E-07	41.38
9.23E-07	41.84

**SPECIMEN #23 RUN #6**

<u>da/dN (m/cyc)</u>	<u><math>\Delta K_{eff}</math> (MPa <math>\sqrt{m}</math>)</u>
2.04E-07	34.17
2.67E-07	34.70
3.31E-07	35.20
3.72E-07	35.80
3.93E-07	36.36
4.15E-07	36.94
4.54E-07	37.53

**SPECIMEN #23 RUN #8**

<u>da/dN (m/cyc)</u>	<u><math>\Delta K_{eff}</math> (MPa <math>\sqrt{m}</math>)</u>
1.87E-07	31.00
2.17E-07	31.31
2.24E-07	31.50
2.44E-07	32.02
2.54E-07	32.55
2.82E-07	33.11
3.11E-07	33.65

## SPECIMEN #23 RUN #9

da/dN (m/cyc)      ΔK<sub>eff</sub> (MPa √m)

6.08E-07	49.42
1.20E-06	50.03
1.65E-06	50.80
1.85E-06	51.15
2.24E-06	52.32
2.27E-06	52.66
2.63E-06	53.52
2.84E-06	54.78
2.90E-06	56.09
3.15E-06	57.44
3.48E-06	58.86
3.65E-06	60.34
3.85E-06	61.88
4.13E-06	62.56
4.46E-06	63.49
5.66E-06	65.17
9.58E-06	68.35

## SPECIMEN #24 RUN #2

da/dN (m/cyc)      ΔK<sub>eff</sub> (MPa √m)

3.51E-07	38.34
4.67E-07	38.99
5.64E-07	39.87
6.67E-07	40.79
6.96E-07	41.26
8.20E-07	41.74
8.37E-07	42.71
1.01E-06	44.25
1.14E-06	45.87
1.53E-06	48.18
1.82E-06	51.02
2.24E-06	54.52
2.95E-06	58.86
3.84E-06	62.39
5.07E-06	65.30
6.57E-06	67.36
8.33E-06	69.54
1.70E-05	73.05

SPECIMEN #31 RUN #2	<u>da/dN (m/cyc)</u>	<u><math>\Delta K_{eff}</math> (MPa <math>\sqrt{m}</math>)</u>
	7.84E-07	37.20
	9.14E-07	37.81
	1.91E-06	38.77
	3.00E-06	40.05
	3.85E-06	41.10
	4.46E-06	42.08
	5.71E-06	43.09
	7.11E-06	48.70
	7.71E-06	51.94
	9.39E-06	55.95
	1.02E-05	57.89
	1.12E-05	59.55
	1.46E-05	64.09
	1.89E-05	68.17
	2.58E-05	71.53
	3.77E-05	75.18
SPECIMEN #32 RUN #7	<u>da/dN (m/cyc)</u>	<u><math>\Delta K_{eff}</math> (MPa <math>\sqrt{m}</math>)</u>
	2.78E-07	29.43
	3.16E-07	29.88
	3.75E-07	30.33
	4.23E-07	30.79
	4.94E-07	31.26
	5.89E-07	31.74
	6.32E-07	32.24
SPECIMEN #32 RUN #10	<u>da/dN (m/cyc)</u>	<u><math>\Delta K_{eff}</math> (MPa <math>\sqrt{m}</math>)</u>
	1.53E-07	25.57
	2.02E-07	25.97
	2.36E-07	26.38
	2.60E-07	26.61
	2.87E-07	26.81
	3.10E-07	27.24
	3.45E-07	27.69
	3.65E-07	28.14
	4.03E-07	28.61
	4.35E-07	28.78
	5.62E-07	29.09

**SPECIMEN #32 RUN #12**

<u>da/dN (m/cyc)</u>	<u><math>\Delta K_{eff}</math> (MPa <math>\sqrt{m}</math>)</u>
----------------------	--

1.96E-06	50.09
2.71E-06	51.20
3.50E-06	52.37
5.00E-06	53.58
7.33E-06	54.84
1.02E-05	56.16
1.24E-05	57.52
1.37E-05	58.95
1.61E-05	60.03

**SPECIMEN #33 RUN #2**

<u>da/dN (m/cyc)</u>	<u><math>\Delta K_{eff}</math> (MPa <math>\sqrt{m}</math>)</u>
----------------------	--

3.40E-07	31.35
3.45E-07	31.83
4.20E-07	32.32
5.22E-07	32.82
5.52E-07	33.34
6.33E-07	33.86
7.37E-07	34.39
1.10E-06	35.05
1.38E-06	36.69
1.60E-06	37.55
1.88E-06	38.90
2.10E-06	41.33
2.36E-06	43.24
3.00E-06	46.99
3.57E-06	50.33
4.25E-06	54.09
6.50E-06	55.72
7.80E-06	58.35

**SPECIMEN #34 RUN #4**

<u>da/dN (m/cyc)</u>	<u><math>\Delta K_{eff}</math> (MPa <math>\sqrt{m}</math>)</u>
----------------------	--

9.68E-06	42.76
1.35E-05	43.69
1.70E-05	44.64
2.00E-05	45.63
2.81E-05	46.66

## SPECIMEN #34 RUN #5

da/dN (m/cyc) $\Delta K_{eff}$  (MPa  $\sqrt{m}$ )

5.08E-07	39.57
1.26E-06	39.81
1.59E-06	40.07
2.67E-06	40.52
5.17E-06	41.51
5.54E-06	42.06
6.33E-06	42.55
7.00E-06	43.22
7.65E-06	43.63
8.57E-06	44.76
1.00E-05	45.94
1.05E-05	47.17
1.21E-05	48.46
1.35E-05	49.81
1.71E-05	50.68
2.43E-05	51.47
2.81E-05	52.20
6.21E-05	53.52

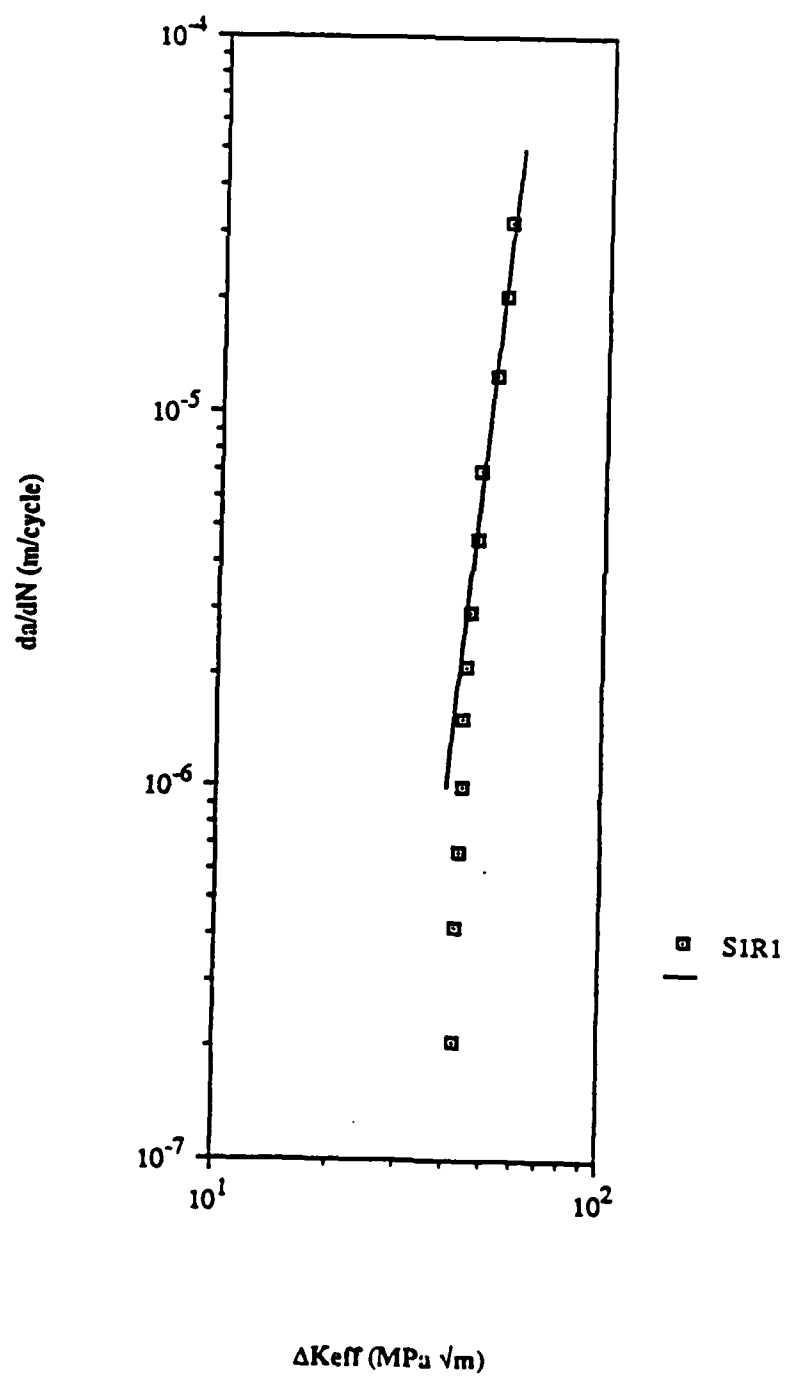
## APPENDIX C

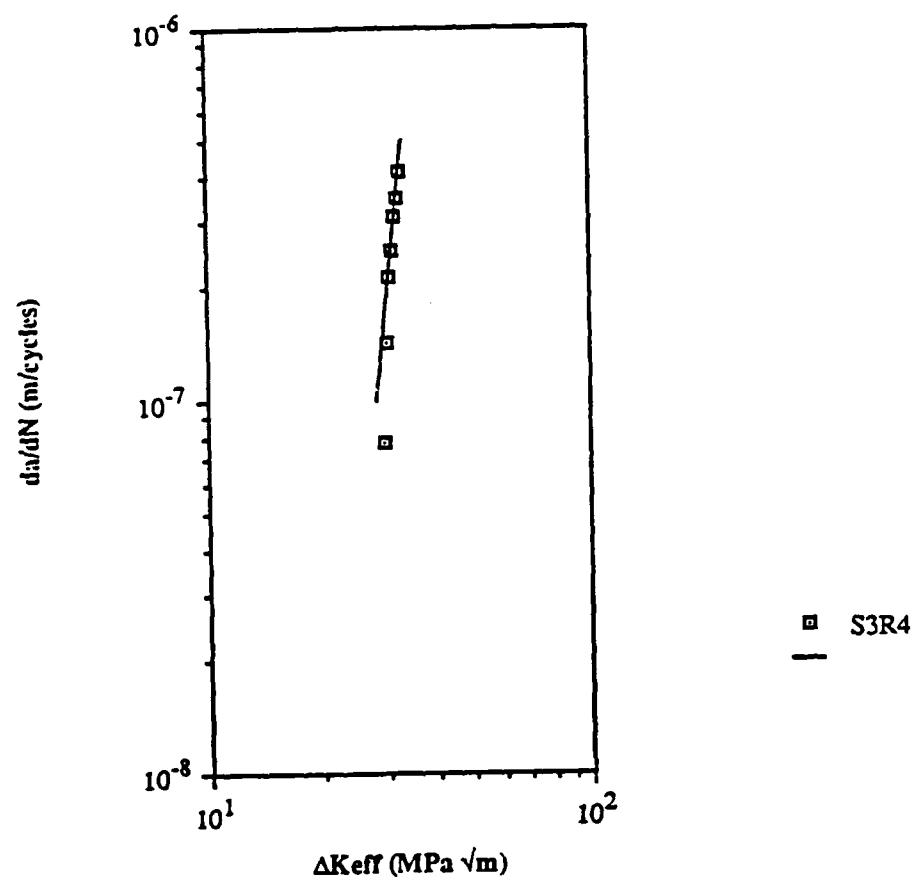
## ALL SPECIMEN DIMENSIONS, LOAD RANGES AND LOAD RATIOS

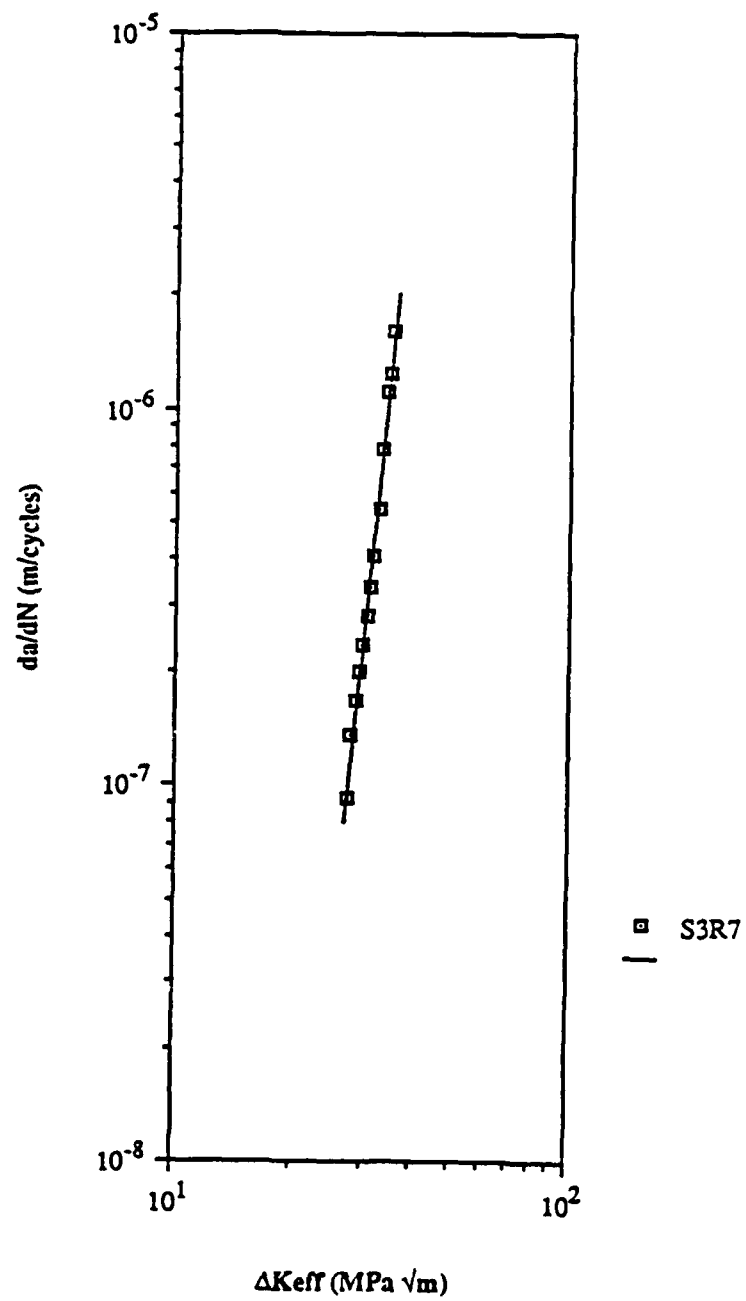
Specimen	Run	Width (cm)	Thickness (cm)	Load $\Delta P$ (kN)	Ratio R
1	1	4.4844	0.8179	16.244	0.103
3	4	4.5047	0.8344	14.322	0.134
3	7			11.551	0.135
3	8			9.794	0.119
11	2	4.7434	0.7861	14.069	0.109
11	4			8.825	0.113
11	5			7.882	0.109
12	2	4.7574	0.8052	14.332	0.160
21	5	4.7104	0.8001	11.854	0.121
23	4	4.7371	0.8674	20.074	0.104
23	6			16.142	0.104
23	8			12.908	0.105
23	9			12.864	0.111
24	2	4.7409	0.8115	16.097	0.107
31	2	4.4475	0.8522	18.130	0.105
32	7	4.8209	0.7950	13.259	0.109
32	10			10.026	0.111
32	12			11.636	0.102
33	2	4.696	0.7976	13.984	0.110
34	4	4.388	0.8115	11.325	0.101
34	5			9.007	0.109

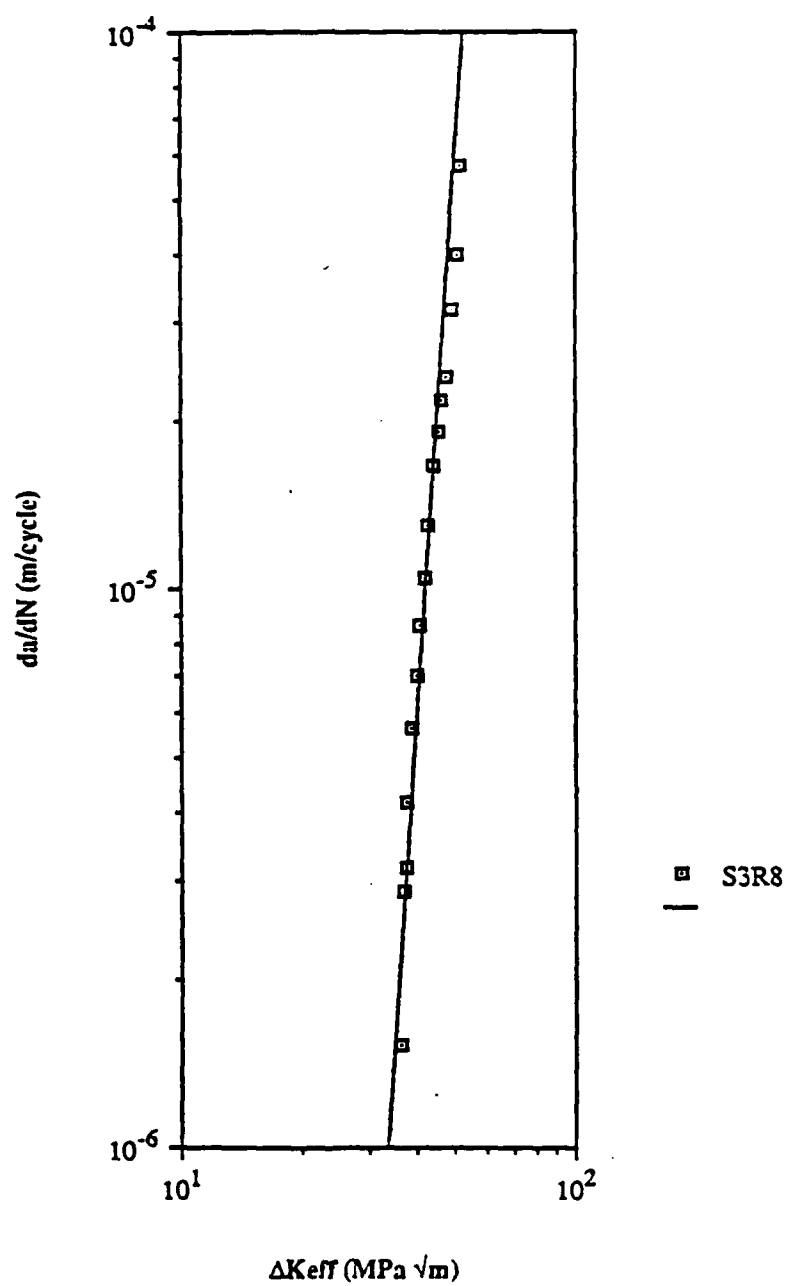


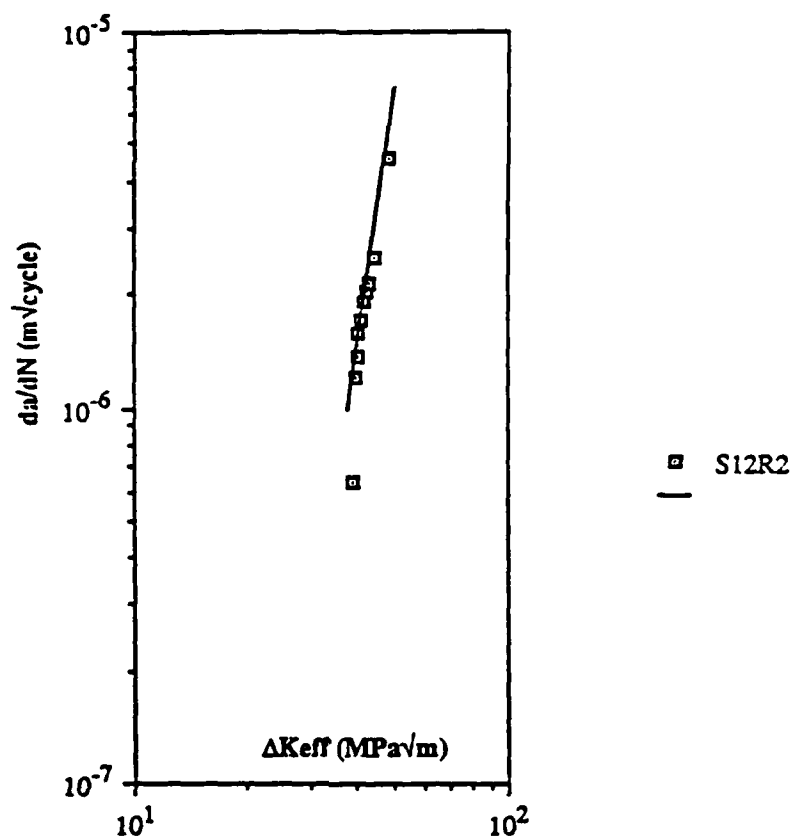
## APPENDIX D

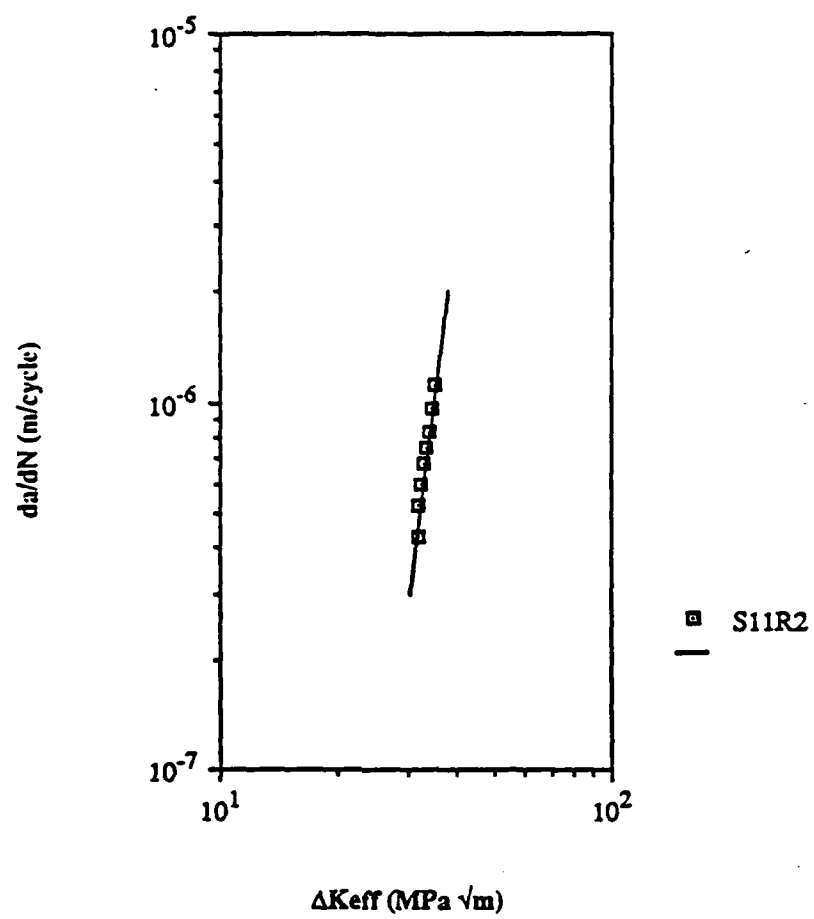
ALL DA/DN VS.  $\Delta K_{EFF}$  PLOTS WITH STRAIGHT LINE FITS

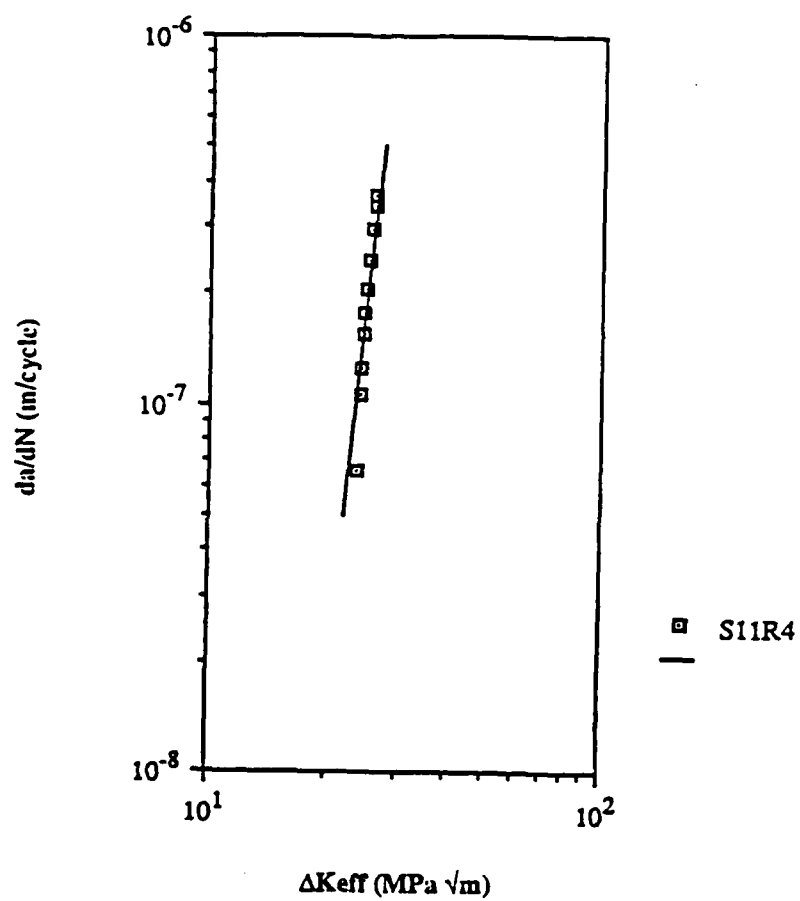


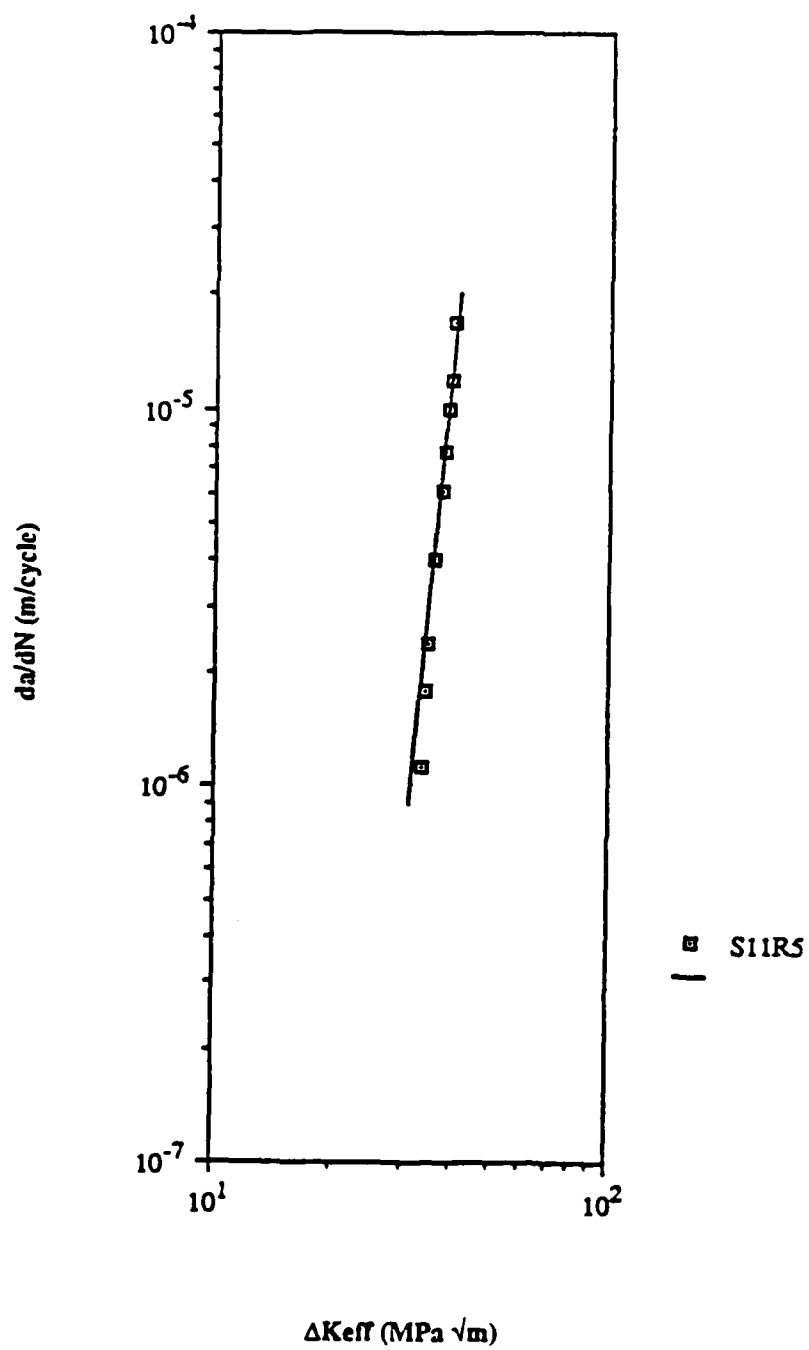




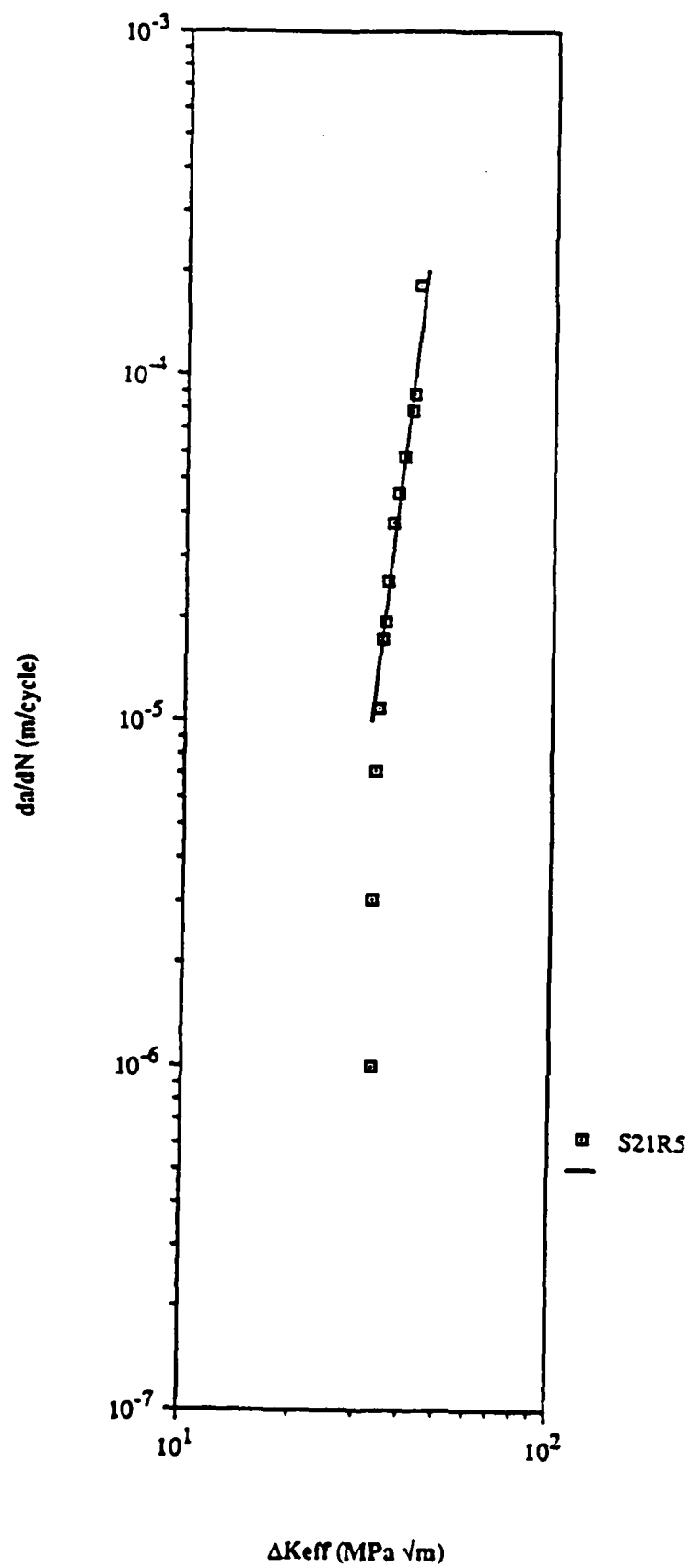


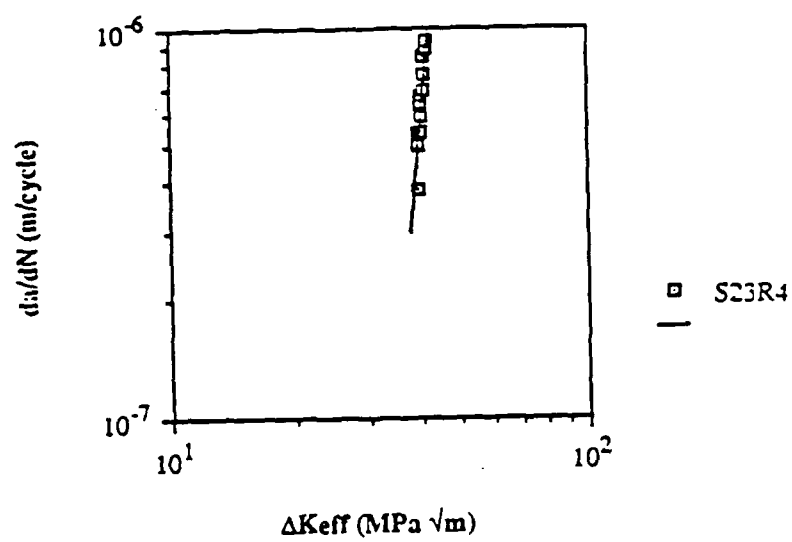


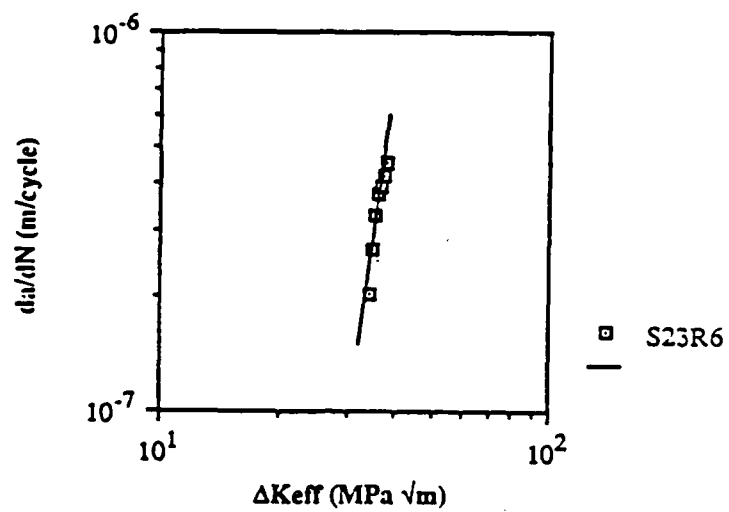


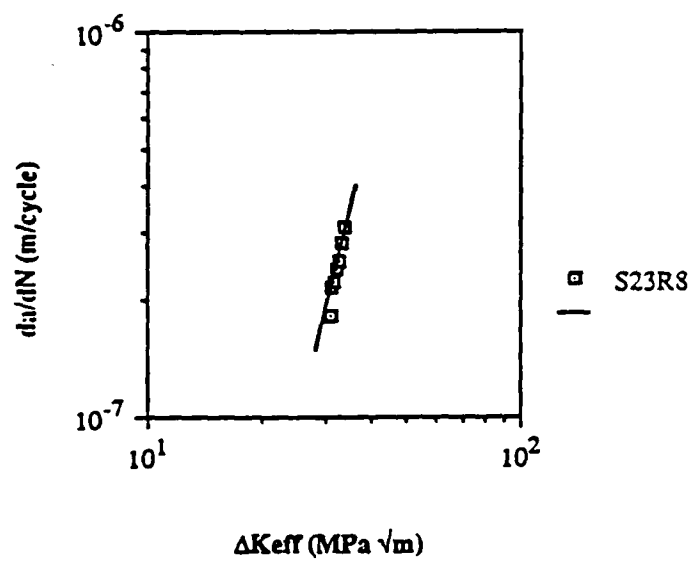


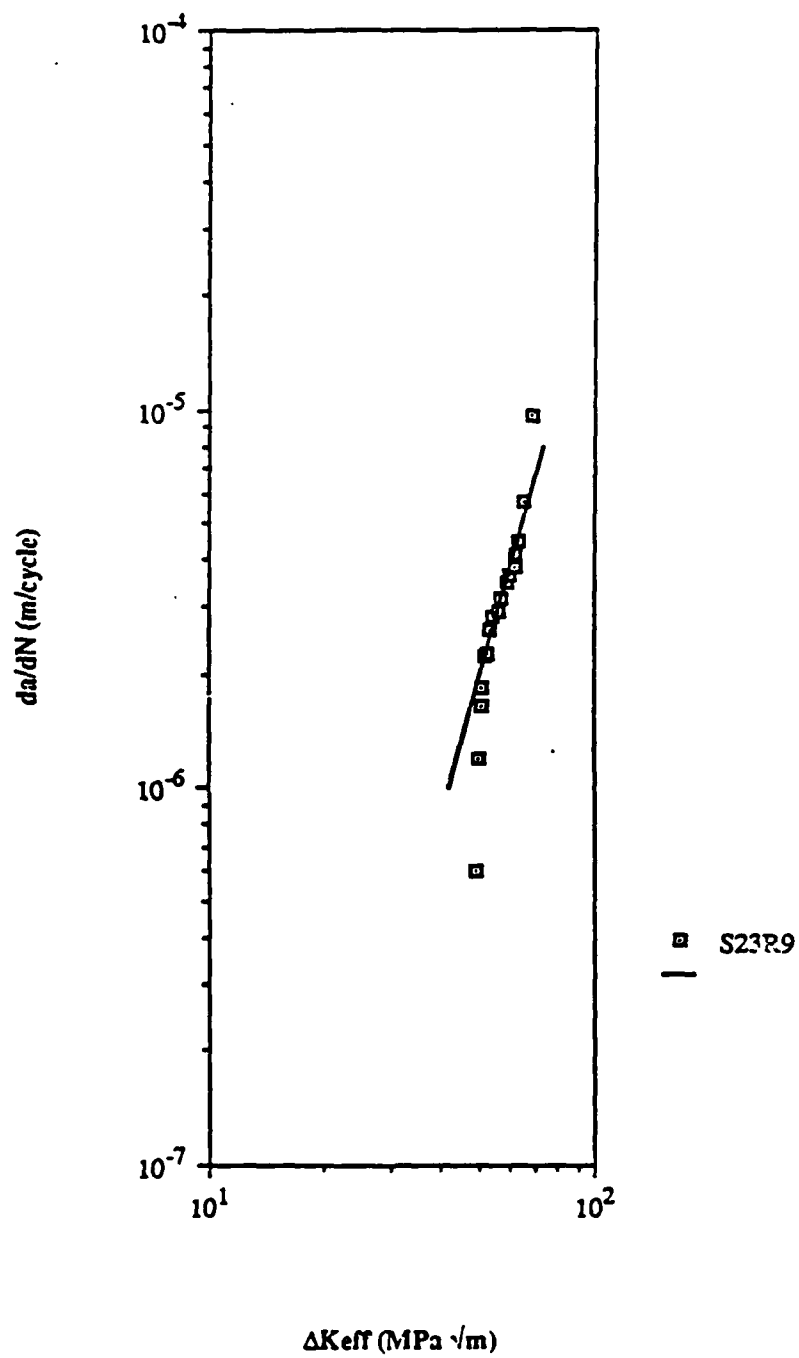


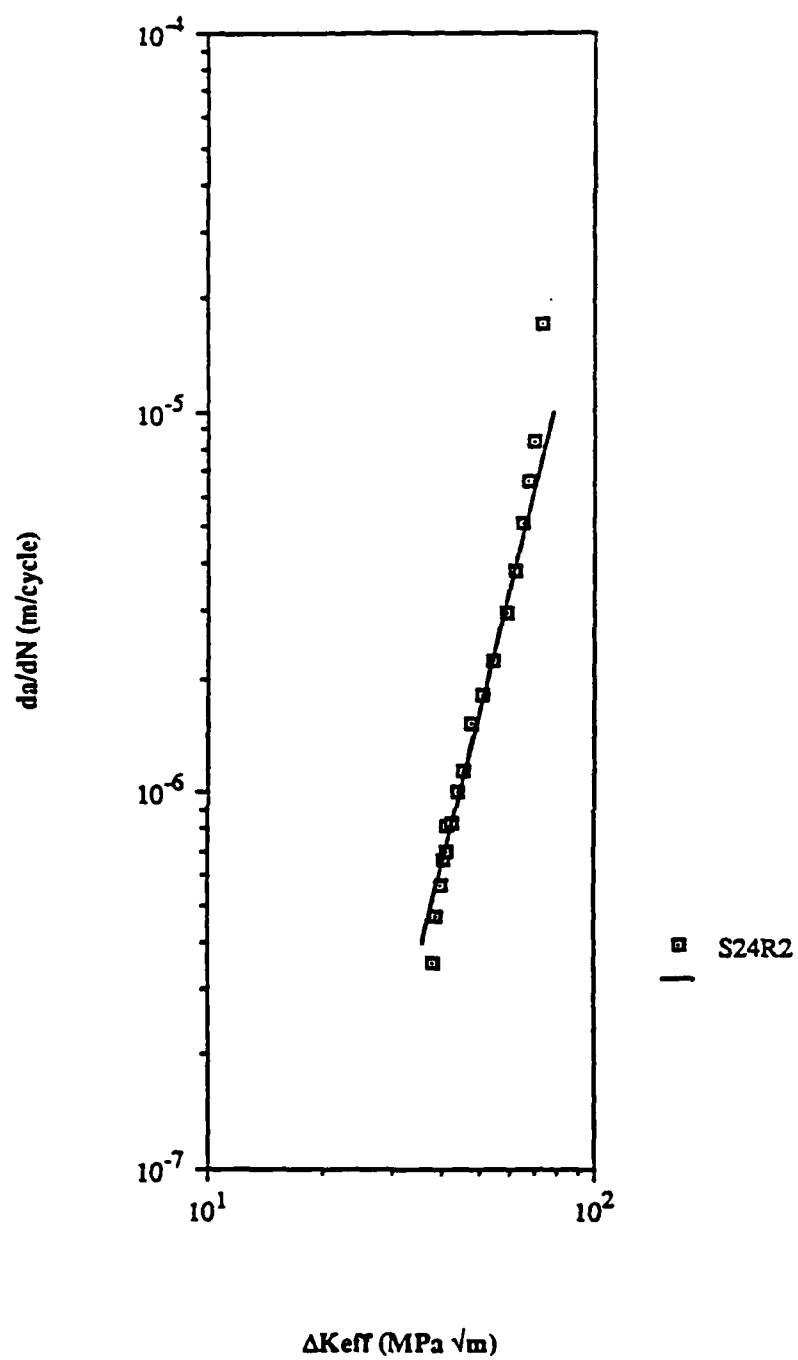


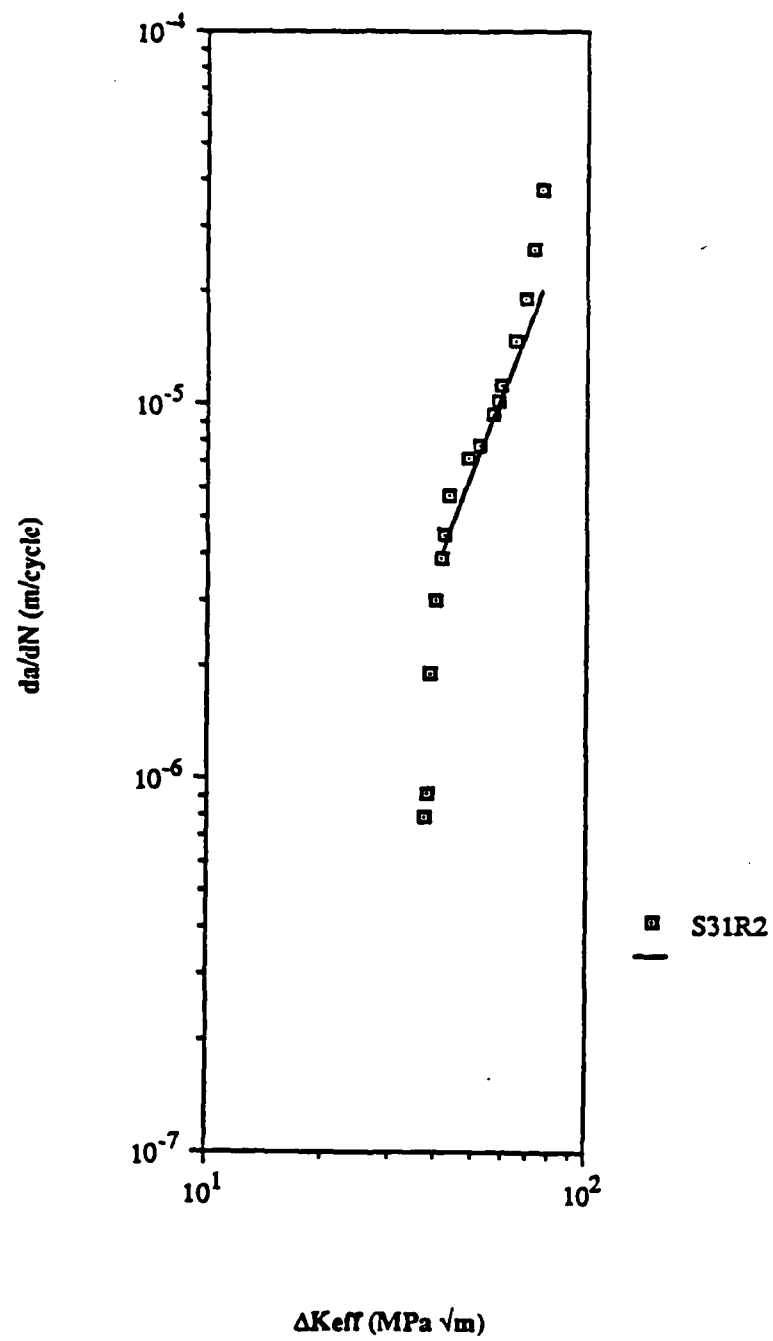


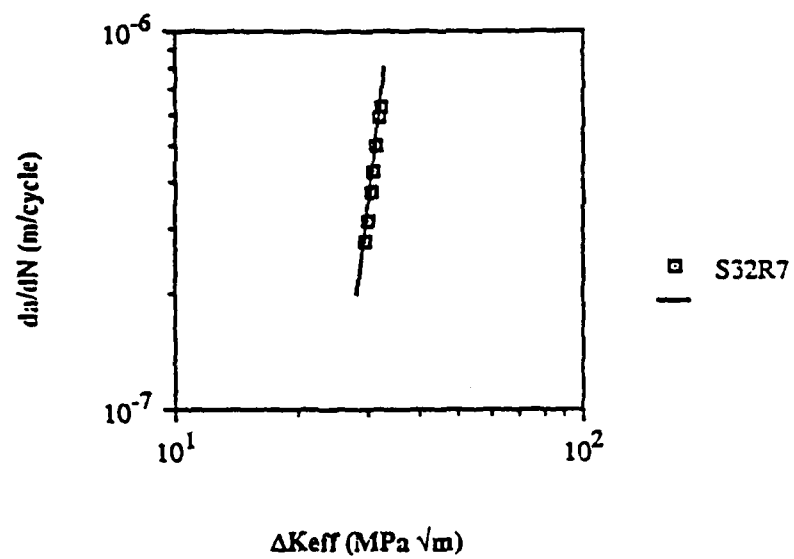




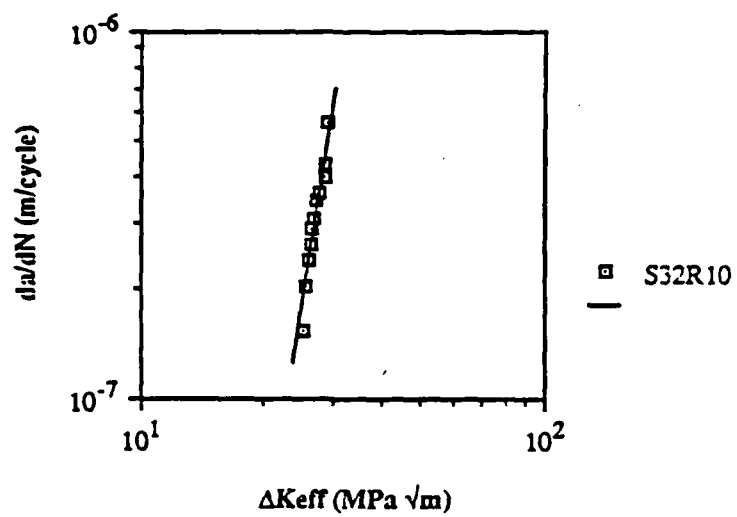


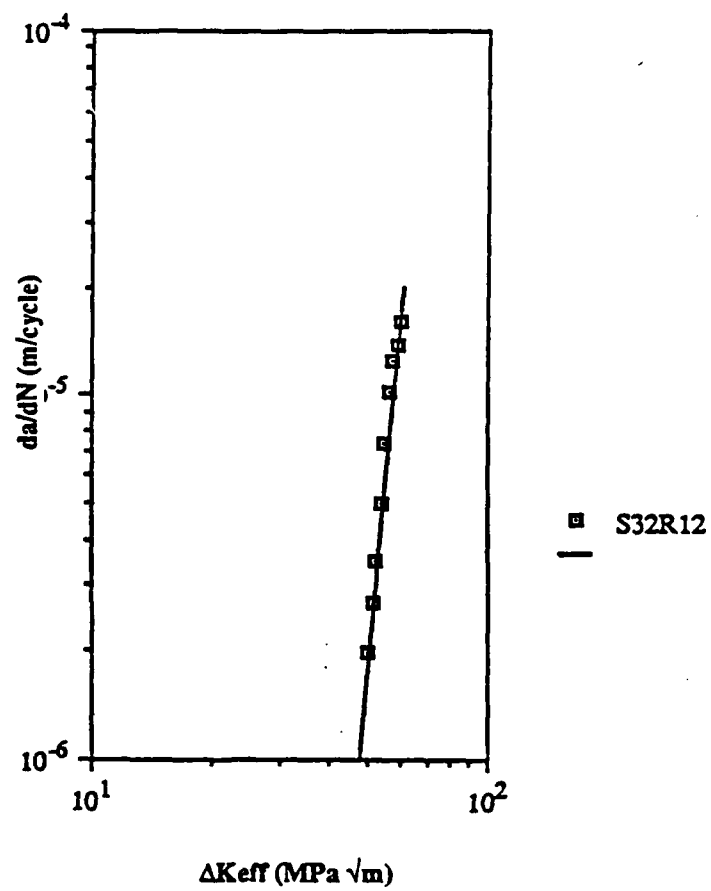


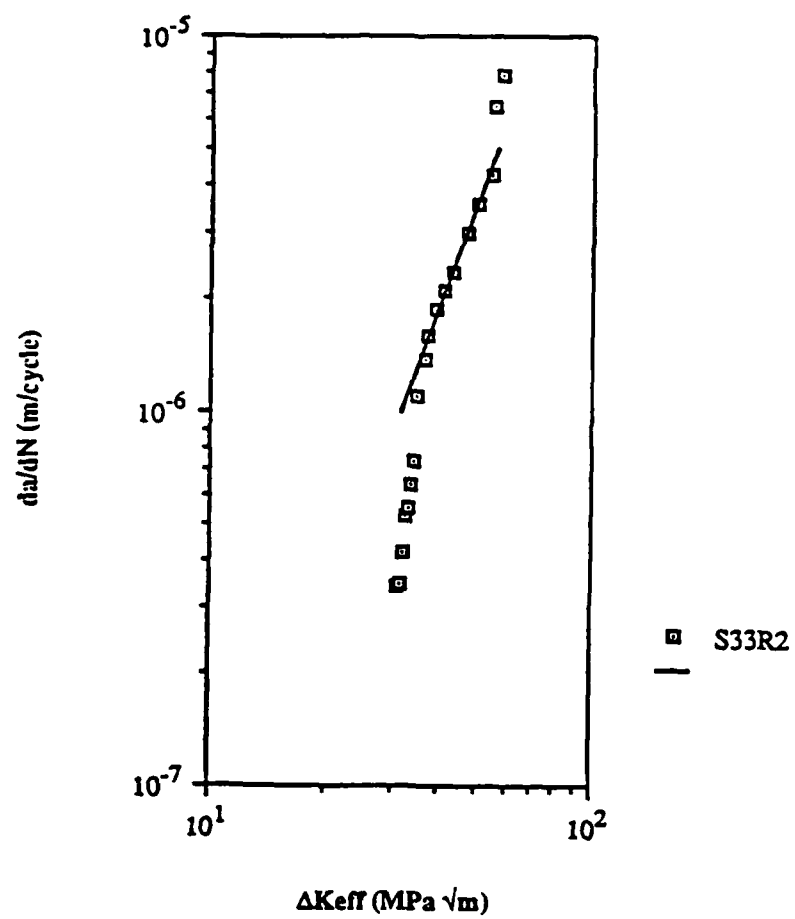


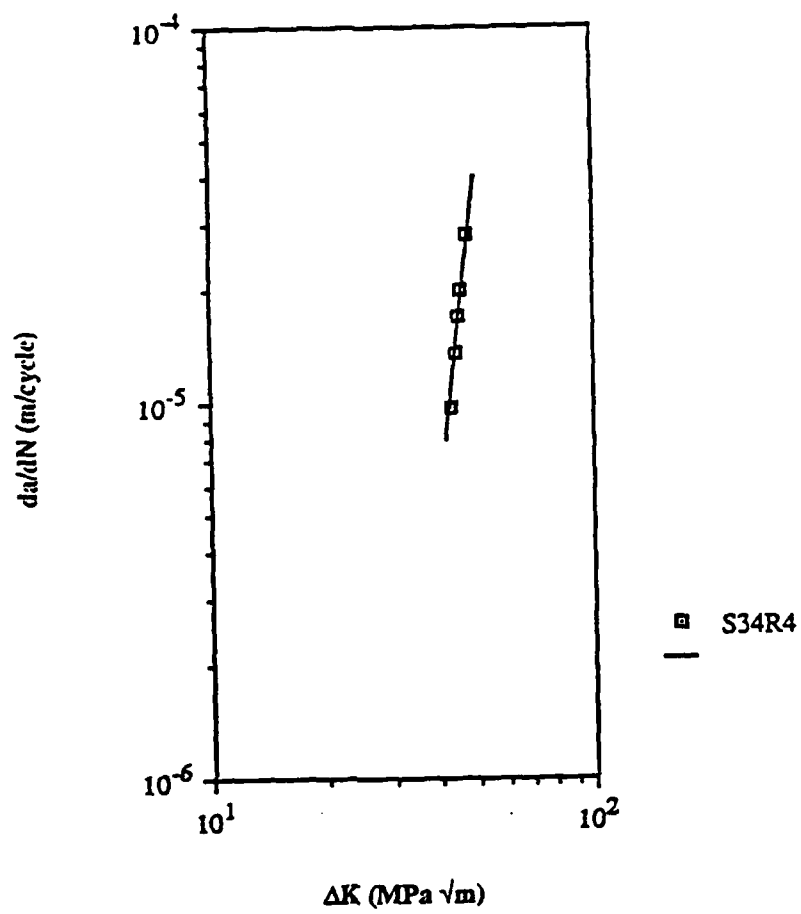


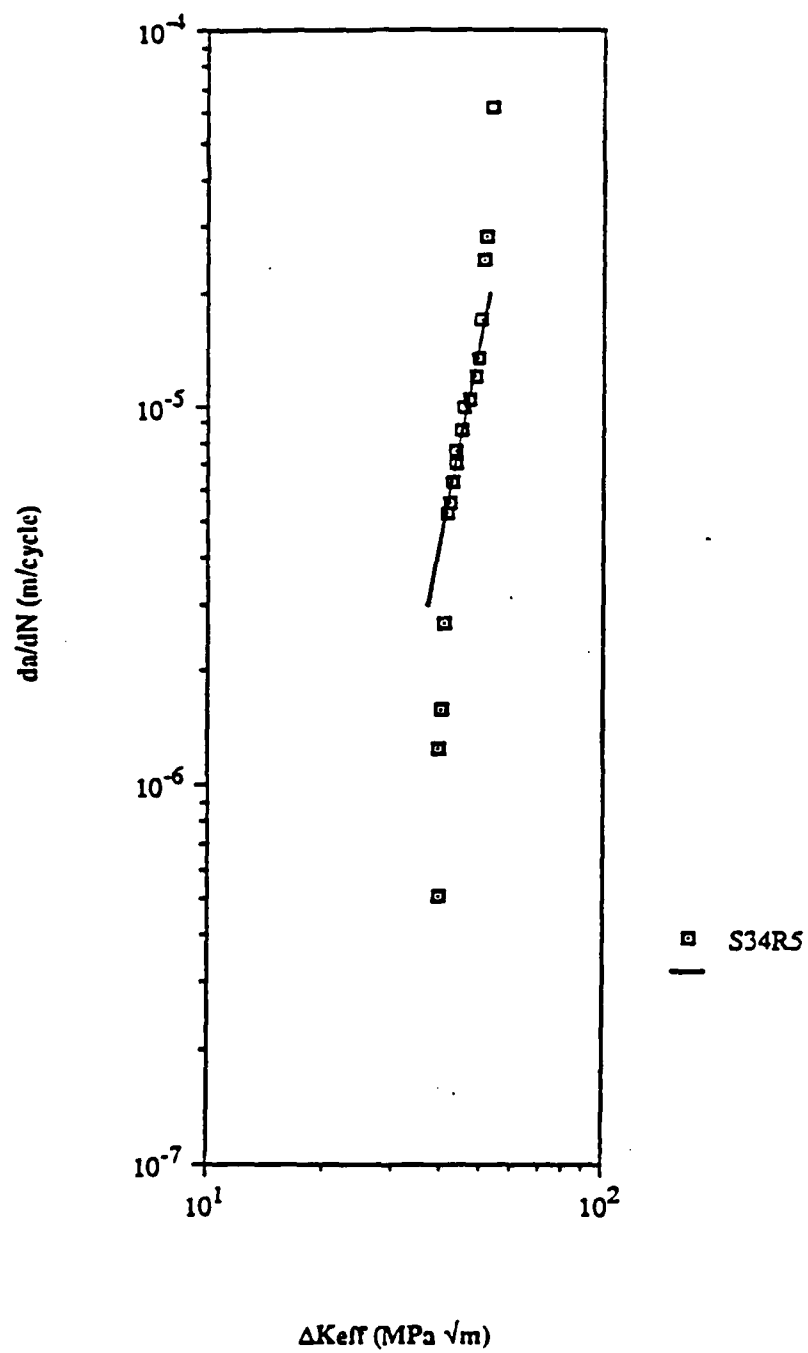












## APPENDIX E

## COMPLETE FINAL CRACK LENGTHS AND MAXIMUM LOAD DATA

Specimen	Run	Final Crack Length (cm)	Maximum Load (kN)
1	1	2.5679	18.1167
2	1	1.9901	29.6059
3	8	3.1026	11.1200
11	5	3.0353	8.8426
12	2	2.7724	17.0581
13	3	2.8334	15.6570
21	7	3.1788	21.6067
22	4	3.1763	11.2178
23	9	3.3007	14.4693
24	2	2.9261	18.0277
31	2	2.6835	20.2606
32	12	3.0353	12.9570
33	2	2.7813	15.7103
34	5	2.8321	10.0169